Engineering Excitonic Properties in van der Waals Solids Using Strain

by

Kanak Datta

A dissertation submitted in partial fulfillment
of the requirements for the degree of
Doctor of Philosophy
(Electrical and Computer Engineering)
in the University of Michigan
2022

Doctoral Committee:

Associate Professor Parag B Deotare, Chair
Professor Stephen R. Forrest
Associate Professor Emmanouil Kioupakis
Professor Zetian Mi

Kanak Datta

kanak@umich.edu

ORCID iD: 0000-0003-4086-3225

Acknowledgements

First and foremost, I would like to express my earnest gratitude to the Department of Electrical and Computer Engineering at the University of Michigan, Ann Arbor for providing me with the opportunity to complete my doctoral study with the necessary financial support, and assistantships. I would also like to thank my supervisor and committee chair Prof. Parag B. Deotare.

My sincere gratitude and heartfelt thanks go to my other dissertation committee members Prof. Stephen R. Forrest, Prof. Zetian Mi, Prof. Emmanuel Kioupakis, who, despite their exhausting and busy schedules, took time to carefully read through the dissertation and came up with valuable suggestions and insights to improve its quality by manifold. Due to their sincere help and effort, the dissertation is in much better shape than it was in its earlier versions.

I want to extend my sincere gratitude to the staff and engineers at Lurie Nanofabrication Facility at the University of Michigan, Ann Arbor for their relentless effort to maintain the state-of-the-art research equipment and sophisticated processing tools. All the devices used and characterized in this dissertation have been fabricated using the facilities and processing tools at the Lurie Nanofabrication Facility. I am grateful to Dr. Sandrine Martin, Dr. Pilar Herrera-Fierro, Dr. Vishva Ray, Katharine Beach, Shawn Wright, Kevin Owen, Matthew Oonk, Brian Armstrong, Brandon Woo, David Sebastian, Steven Sostrom, Jorge Barreda, Tony Sebastian, Matthew Gutierrez, Gregg Allion, and many others for their generous and courteous help. My special thanks go to Katharine for taking up the responsibility of being my mentor in the absence of a senior

member in our lab and helping me to get accustomed to nanofabrication and processing techniques in my early days.

I would like to thank my current lab members Zidong Li, Zhengyang Lyu, Yuchen Kan, and Zhaohan Jiang for their help with experiments, sample preparation, and characterization. I am also grateful to the members who have graduated – Arun Nagpal, Emmett Litvak, and Wyman Smith for their help at different times over the course of time. My gratitude also goes to Dr. Darwin Cordovilla, and Dr. Che-Hsuan Cheng for their helpful discussions and suggestions at various crossroads during my doctoral research.

I also want to thank my collaborators Prof. Elaheh Ahmadi, Kamruzzaman Khan, Prof. Osman M Bakr, and Dr. Ibrahim Dursun for giving me the opportunity to work and learn from them over the course of our projects. From high-quality scientific research to thoughtful pragmatism, I feel blessed to acquire many traits that have helped me to get better as a researcher. My sincere thanks also go to Dr. Afzaal Qamar and Prof. Mina Rais-Zadeh for helping me with the RF characterization tools when necessary.

Table of Contents

List of Figures

perylenetetracarboxylic dianhydrides." The Journal of chemical physics 82.4 (1985): 1682-1687. (c) Experimental set-up for in-situ photoluminescence measurement from an organic thin film under pressure. The motorized micrometer and the spring together apply a linear pressure on the thin film sandwiched between quartz substrate and a cover slip. (d) Dynamic pressure induced solvatochromic shift in PS: DCM2 and Alq_3: DCM2 systems. A clear pronounced red shift is observed as a function of pressure in both thin films. (c) and (d) - Reprinted (adapted) with permission from Chang, Wendi, Gleb M. Akselrod, and Vladimir Bulovic. "Solid-state solvation and enhanced exciton diffusion in doped organic thin films under mechanical pressure." ACS nano 9.4 (2015): 4412-4418. Copyright 2015 American Chemical Society. (e) Pressure induced spectral red-shift in a donor: acceptor blend (1:1 m-MTDATA: 3TPYMB). The redshift in photoluminescence is attributed to both solvation and reduced molecular proximity under increased pressure. Reprinted (adapted) with permission from Chang, Wendi, et al. "Spin-dependent charge transfer state design rules in organic photovoltaics." Nature communications 6.1 (2015): 1-6. 15

Figure 2-3: Static strain induced excitonic photophysical manipulation in TMDs. (a) Schematics of strain application on monolayer TMD by bending flexible substrates. Reprinted (adapted) with permission from Conley, Hiram J., et al. "Bandgap engineering of strained monolayer and bilayer MoS_2." Nano letters 13.8 (2013): 3626-3630. Copyright 2013 American Chemical Society. (b) Absorption spectra of strained (2.1%) and unstrained monolayer WSe_2. The strained monolayer absorption shows a clear redshift and reduction in linewidth due to bandgap reduction and reduced exciton-phonon coupling. Reprinted (adapted) with permission from Aslan, Ozgur Burak, Minda Deng, and Tony F. Heinz. "Strain tuning of excitons in monolayer WSe_2." Physical Review B 98.11 (2018): 115308. (c) Strain induced exciton photoluminescence modulation in monolayer

(top), and under AFM indentation (middle) on the monolayer. The bottom image shows the difference that shows the funneled fraction of excitons. The scale bar is 1 μm. (d) Reversible control over PL excitation due to exciton funneling under AFM indentation. (b), (c), and (d) - Reprinted (adapted) with permission from Moon, Hyowon, et al. "Dynamic exciton funneling by local strain control in a monolayer semiconductor." Nano Letters 20.9 (2020): 6791-6797. Copyright 2020 American Chemical Society. (e) Normalized PL spectra from monolayer WS_2 under strain that shows a clear shift. Two gaussian fitting of the PL spectra at different strain levels show conversion from exciton to trion under large strain in the monolayer. Reprinted with permission from Harats, Moshe G., et al. "Dynamics and efficient conversion of excitons to trions in non-uniformly strained monolayer WS_2." Nature Photonics 14.5 (2020): 324-329. (f) Room temperature PL centroid map of a monolayer WSe_2 transferred on a SiO_2 nano-pillar pattern that shows clear redshift at the position of the nano-pillar. (g) Normalized exciton density extracted from diffusion measurement at room temperature. The measurement position is marked in (f). The exciton flux shows a clear drift towards the position of maximum strain on the monolayer alongside diffusive transport at room temperature. (f) and (g) - Reproduced from Cordovilla Leon, Darwin F., et al. "Exciton transport in strained monolayer WSe_2." Applied Physics Letters 113.25 (2018): 252101, with the permission of AIP Publishing. 21

Figure 2-5: Acoustic field induced manipulation of excitons. (a) Schematic illustration of the GaAs/ AlGaAs device geometry with the patterned IDTs and the generation and excitation positions. The prolonged lifetime of the indirect excitons is sustained along the channel by applying an out-of-plane electric field. (b) Schematic illustration of type – I band edge modulation where the conduction and valance bands are modulated out of phase under strain. (a) and (b) - Reprinted (adapted) with permission from Violante, Adriano, et al. "Dynamics of indirect exciton

transport by moving acoustic fields." New Journal of Physics 16.3 (2014): 033035. (c) Spatial PL profiles from indirect excitons for different gate voltages Vg in the absence (dashed lines) and presence (solid lines) of a SAW with P_{rf} 24 dBm. The inset shows the diffusion length L_{ex} extracted from the decay of the profiles towards negative X. Reprinted (adapted) with permission from Rudolph, J., R. Hey, and P. V. Santos. "Long-range exciton transport by dynamic strain fields in a GaAs quantum well." Physical Review Letters 99.4 (2007): 047602. (d) Cryogenic excitonic multiplexing circuit based on the concept of dynamic strain induced exciton transport. Acoustic transport of IX excitons under 10 dBm RF excitation at (e) input port 1 (SAW_1) and (f) input ports 1 and 2 (SAW_1 and SAW_2 inputs are active at the same time). (d), (e), and (f) - Reprinted (adapted) with permission from Lazić, S., et al. "Scalable interconnections for remote indirect exciton systems based on acoustic transport." Physical Review B 89.8 (2014): 085313. Long range exciton transport under dynamic strain in 2D heterostructure at 100 K. (g) When the SAW is off the indirect excitons shows diffusive transport behavior. As the SAW is turned on, two bright peaks appear at the far end of the flake due to the exciton transport by dynamic acoustic lattice. (h) Acoustic lattice mediated exciton transport in TMD heterostructure under different RF excitations (i) 0 mW (ii) 4.5 mW (iii) 6 mW. (g) and (h) - Reprinted (adapted) with permission from Peng, Ruoming, et al. "Long-range transport of 2D excitons with acoustic waves." Nature communications 13.1 (2022): 1-7. 23

Figure 3-1: Axial strain on buckled SiO_2 microbeam: (a) Surface profile of a doubly supported SiO_2 microbeam released by gas-phase XeF_2 etching step. The surface profile is extracted using non-contact white light interferometry. (b) Maximum deflection of buckled microbeam, and the corresponding axial strain measured at the maximum defection point for different beam lengths. The axial strain at maximum deflection point decreases with increased beam length. (c) Deflection

List of Appendices

Abstract

While electronics sits at the forefront of logic processing and data communication in microprocessors, the ever-increasing trend of on-chip power density has rendered the sustainability of device scaling questionable. This has also predominantly inspired the exploration of alternative pathways for energy-efficient data communication and information processing. *Excitonics,* not only offers a viable alternative for low-power logic processors but also, low-footprint communication. At room temperature, excitons only exist in a handful of semiconducting media - organic materials and recently discovered transition metal dichalcogenides (TMD) monolayers. While the room temperature existence makes it technologically relevant, controlling the exciton dynamics remains a challenge.

The thesis addresses the challenge by exploring strain-based approaches. We first investigate the uniaxial strain modulated photophysics in an organic excitonic guest: host blend Alq_3: DCM, where the excited state properties are governed by a phenomenon called solid-state solvation. We utilize buckled SiO_2 microbeams to apply axial strain on an overlying host: guest thin film and tune the excited state photoluminescence from the guest molecules. We further verify that the observed spectral shift indeed originates from modulation in local dielectric polarization triggered by the molecular density under axial strain. We also demonstrate dynamic tuning of the molecular fluorescence by electrostatic actuation of a Si_3N_4 microbeam fabricated on a Si_3N_4/Si substrate. Later, we study piezoelectric modulation of excitonic photoluminescence in a monolayer semiconductor at room temperature under strong dielectric screening. As an archetype system, we study the photoluminescence spectral modulation in monolayer WSe_2 transferred on piezoelectric

$LiNbO_3$ substrate. Strong screening from the substrate leads to enhanced exciton dissociation and electric field-dependent shift of exciton emission energy – both can be further tuned by optically generated free carrier density. Finally, we investigate exciton transport under traveling strain in monolayer WSe_2 encapsulated by bulk h-BN (h-BN/WSe_2/h-BN). We generate high-frequency Rayleigh type SAW on piezoelectric Y-cut $LiNbO_3$ substrate by patterning interdigitated electrodes (IDTs). Traveling strain generated by the SAW wave creates out-of-phase modulation of the monolayer energy bands - also known as the Type – I modulation. We also demonstrate acoustic steering of the photogenerated exciton density by precision control over the instantaneous SAW phase using phase synchronized time-correlated single photon counting scheme (TCSPC). We find that the acoustic transport of excitons in monolayer TMDs at room temperature is limited by the intrinsic exciton mobility and the spatial extent of the monolayer. Lower intrinsic mobility results in the *'weak coupling'* of the photo-generated excitons to the traveling strain wave.

Chapter 1 Introduction

1.1 The promise of excitons in van der Waals solids

An *exciton* is a coulombically bound state of two fermions - an *electron* and a *hole*, generally found in low-dimensional semiconducting systems. These species strongly govern the photophysical properties of some classes of van der Waals solids. Van der Waals solids are materials where the constituents (atoms or molecules) are held together by a short range, weakly interacting force known as the van der Waals force [1], [2]. In this dissertation, we use the term 'van der Waals solids', for referring to two specific classes of materials – organic molecular solids - where van der Waals force acts as the primary intermolecular force and the recently discovered inorganic layered two-dimensional materials such as semiconducting transition-metal dichalcogenides (TMDs) - where thin sheets of covalently bonded atoms are held together by out of plane van der Waals force [3].

When a low-dimensional semiconducting system is optically excited above or around its bandgap energy, an e*lectron* (a negatively charged fermion) is elevated from the valance to the conduction band, leaving behind an empty state – a *hole*, also a fermion, and conceived to be of equal and opposite charge of an electron. Therefore, an attractive Coulomb force exists between these fermions that results in a bound state called an *exciton*. The *binding energy* of such a bound pair state depends strongly on the dielectric surrounding of the media. In material systems with relatively small dielectric constant (organic materials), the binding energy can be more than 1 eV [1], [4], [5]. Such excitons are referred to as *Frenkel* excitons [6]. Being a largely disordered system, excitons in organic materials are strongly localized and show poor transport

characteristics. On the contrary, in inorganic semiconductors, due to the large dielectric constant, the binding energy is smaller (~ 10 meV). Commonly referred to as *Wannier* excitons [7], these species exist in low dimensional III-V semiconducting structures – quantum well, quantum dots, or quantum wires. Although, room temperature thermal energy (k_BT) limits the exploration of exciting excitonic physics in inorganic III-V media, monolayer 2D materials with ultra-scaled dimension and out-of-plane confinement [8], [9] can sustain excitons with large binding energy and therefore offer a unique platform for studying exciting physical aspects and applications of *Wannier* excitons at room temperature. The tunability of excitonic properties in van der Waals solids under external strain can be quite different in the two material systems. For example, the excitonic energy in TMDs undergoes blueshift/redshift due to an increase/decrease in bandgap under compressive/tensile strain [10], [11]. In molecular organic solids, the excitons primarily show redshift when external pressure is applied and vice versa.

The enriched and diverse photophysical nature of excitons in these two different media largely shapes the motivation behind excitonic research. Excitons in organic semiconductors have been traditionally investigated for flexible, low-cost, high-performance optoelectronic applications such as photovoltaics, organic light emitting diodes (OLEDs), thin film transistors (TFTs), and displays. Application-specific tailoring of excitonic photophysics in these materials is achieved primarily through artificial synthesis and chemical engineering. On the other hand, the naturally occurring band properties in TMDs make them extremely sensitive to external strain and allows long rage exciton transport. Contrary to electronic devices where energy-efficient operation is largely limited by lossy stray and parasitic capacitance, excitons, being chargeless entities, can provide a viable alternative for low-loss, energy-efficient logic processing, and data communication, and sensing. Furthermore, the monolayer nature of TMDs allows excitonic device

scaling down to sub-nanometer dimension. Therefore, engineering pathways to modulate photophysics of excitons at room temperature in these media is of paramount importance to research communities across the world.

Over time, various approaches have been adopted, studied, and explored to engineer exciton photophysics in organic and inorganic semiconducting systems – strain engineering [12]–[16], external electric field [17], [18], magnetic field modulation [19]–[21], modulating molecular concentration [22], [23], and so on. In the organic semiconductor domain, strain engineering traditionally refers to the application of external pressure to alter the intermolecular interaction in small molecular systems, morphology in polymer chain organic thin films, inter-chain molecular interaction, background dielectric polarization of the medium, etc. using apparatus like diamond anvil cell (DAC) [15], [24], [25] or linear pressure gauge [14], [21] or an AFM tip [26], [27]. Such apparatus have intrinsic large footprint and therefore are not viable for integration into traditional on-chip nanofabrication platforms. To harness the true potential of organic semiconductor photophysics for optoelectronic applications, an on-chip device platform that can leverage traditional nanofabrication techniques is still required and therefore should be investigated. Another widely adopted approach for tuning exciton photophysics in organic semiconductors has been the utilization of solid-state solvation effect reported by Bulovic et al. [28]–[30] where the background dielectric environment is modulated by the addition of external molecular entities [22].

In the inorganic III-V semiconductor domain, strain has been widely used to control the exciton photoluminescence emission from quantum wells [31], [32], quantum wires [33], [34] and quantum dots [35]–[37] Excitons in these systems have very low binding energy and therefore can only be studied at cryogenic temperatures which severely limits their application bandwidth. More recently discovered 2D semiconductors provide a unique advantage in this regard not only due to

their large exciton binding energy (ranging over a few hundreds of *meV* [38], [39]) but also due to their intrinsic strong mechanical strength and rigid nature [40], [41]. These materials can be bent, extended, stretched beyond the limits of traditional bulk III-V semiconductors, and therefore offer a larger range for studying strain-tuned exciton photophysics. These materials also show larger sensitivity to external strain when compared to bulk III-V semiconductors. Traditional means of strain tuned exciton manipulation in monolayer 2D semiconductors includes utilization of flexible substrates [42], [43], patterned nanostructures [44], [45], MEMs actuators [46], local dynamic strain engineering [47], [48]. Static non-uniform strain generated by patterned nanostructures triggers room-temperature directional exciton transport in these semiconductors, a phenomenon commonly referred to as *exciton funneling* [48], [49]. In recent years, exciton transport under static strain modulated non-uniform energy landscape has been extensively studied.

On the other hand, a traveling strain wave is typically generated by surface acoustic waves (SAW) propagating at the surface of a piezoelectric material [50], [51]. In such a scheme, photogenerated excitons with high mobility can get trapped at the local potential pockets created by the traveling strain wave and are transferred over a long distance at the velocity of the wave [52], [53]. While static strain is traditionally utilized for exciton engineering, traveling strain generated by surface acoustic wave (SAW) has remained largely unexplored as means for achieving control over exciton photophysics and directional transport at room temperature. Such a scheme has been used to demonstrate the transport of indirect excitons up to a few hundred μms at cryogenic temperatures. Such long-range transport is attributed to large exciton mobility of excitons in III-V semiconductor quantum wells at cryogenic temperatures as well as the long lifetime of spatially indirect excitons. Excitonic circuits operating at cryogenic temperatures have also been demonstrated based on the long-range transport of indirect excitons in such material

systems [54]. Traveling strain, therefore, can be used not only to expand the application bandwidth of 2D monolayer semiconductors in the exciton transport domain but also to add new explorative domains to the already enriched excitonic physics. Moreover, with recent reports of exciton transport under dynamic strain in TMD heterostructures [55], a detailed understanding of the dynamic interaction of excitons at room temperature in monolayer TMDs and traveling strain waves is also of great importance.

1.2 Organization of this thesis

In the second chapter, we present a brief review on the field of strain engineering of exciton photo-physics in organic and inorganic van der Waals solids by summarizing the recent progresses. We briefly introduce the physical properties of excitons in molecular solids and in inorganic semiconductors. We also revisit the recent works and progresses in the field of strain-engineered excitonics in these two material systems.

In the third chapter, we demonstrate a small footprint on-chip platform that can be utilized for strain-tuned photophysical manipulation of excitons in molecular solids. We use buckled SiO_2 microbeams to apply axial strain an organic thin film grown by vapor thermal evaporation and trigger the solid-state solvation effect. As an archetype media, we use a widely used organic host: guest media Alq_3: DCM. Axial strain generated by the buckled microbeam modifies the local molecular density of the overlying thin film and local polarization field in the media. This triggers a proportional blueshift in the dopant emission energy. We estimate that for 1.5% doped thin film, the axial strain can modify the emission energy of the dopant at a rate of 16 meV/%. We also show that the solvatochromic shift in such a molecular media under external strain depends on the guest doping. We also show dynamic modulation of DCM emission energy by fabricating micro

electromechanical structures (MEMs) on Si_3N_4/ Si substrates in a 1.5% doped Alq_3: DCM thin film. We also discuss a possible application of such a self-strained platform as means for the determination of mechanical properties of the thin film under study.

In the fourth chapter, we use strong environmental dielectric screening to trigger piezoelectric modulation of photoluminescence in an inorganic monolayer van der Waals semiconductor – WSe_2. When transferred on a strong piezoelectric substrate ($LiNbO_3$), the monolayer WSe_2 experiences strong substrate-induced dielectric screening. This results in a large reduction in binding energy and an increase in exciton polarizability. We estimate the exciton polarizability to be 8.5×10^{-6} Dm/V from the photoluminescence spectral shift under RF electric field. We also observe a strong electric field-dependent dissociation that can be further tuned by photoexcitation. We further verify our observation from optical fluence-dependent transient photoluminescence measurement under RF excitation.

In the fifth chapter, we demonstrate room-temperature exciton transport by traveling strain wave in h-BN/ monolayer WSe_2/ h-BN system. Encapsulation by bulk h-BN moderates the monolayer's dielectric surrounding and helps reduce exciton dissociation under SAW electric field. h-BN encapsulation also improves exciton transport properties by reducing the scattering centers. From our measurements, we estimate exciton mobility in monolayer WSe_2 to be in the region of 900 $cm^2/eV/s$. We also observe that exciton transport under traveling strain is limited in the weak coupling regime due to the small intrinsic mobility of room temperature excitons in monolayer WSe_2 leading to an estimated exciton velocity of 600 m/s which is significantly smaller than the SAW velocity in $LiNbO_3$ (3980 m/s).

In the sixth chapter, we summarize the results shown in this work and discuss possible future applications of strain-tuned excitonic manipulation in van der Waals monolayer semiconductors and their heterostructures. Finally, we conclude our discussion in chapter seven.

Chapter 2 Strain Engineering of Excitons in Van der Waals Solids: A Brief Overview

2.1 A brief introduction to Van der Waals materials

Simply stated, van der Waals solids are materials where the constituent entities are held together by a type of weak cohesive force known as the van der Waals force. As mentioned before, in this dissertation, be the term 'Van der Waals solids', we refer to two classes of materials: organic molecular compounds where van der Waals force is one type of the cohesive force that bind the molecules together and most recently discovered transition metal dichalcogenides (TMDs) where thin sheets of covalently bonded atoms are held together by an out-of-plane attractive force.

Organic materials can be broadly classified into three different types: small molecules, polymers, and biological. The excited-state properties in these materials are strongly governed by the nature of inter-atomic and inter-molecular forces within the material. Weak cohesive forces such as van der Waals forces, dipole-dipole, dipole-induced dipole, hydrogen bonds, London dispersion forces, etc. [1] give rise to the amorphous or polycrystalline nature in small molecular organic thin films. Weakened inter-molecular interaction leads to strongly localized molecular orbitals that are sequentially occupied by electrons. This gives rise to the highest occupied molecular energy (HOMO) level and lowest unoccupied molecular orbital (LUMO) energy levels and an energy separation between them, commonly referred to as the *energy gap*. Following the absorption of a photon, an electron is promoted from a HOMO molecular orbital to a LUMO molecular orbital forming a coulombically bound state known as an *exciton*. These spatially confined molecular excited states have large binding energy (more than one or two orders of

magnitude larger, when compared to excitons in low-dimensional III-V quantum wells at cryogenic temperatures [56], [57]) and thus, are stable even at room temperature [4]. Additionally, the excitonic states can be either spin paired (also known as singlet states, having a net spin of zero) or spin unpaired (also known as triplets, having a net spin of one). The transition between the singlet and triplet states occurs via inter-system or reverse intersystem crossing and can be manipulated under external pressure [21]. The energy stored in such excited states can be transported from one molecular site to the neighboring site (hopping) via short-range energy transfer processes such as Förster Resonance Energy Transfer (FRET) [58], [59] or Dexter [60], [61] energy transfer. Thus, the transport distance primarily depends on the spectral (FRET) and/or the wavefunction (Dexter) overlap between molecules. Additionally, morphology (amorphous, polycrystalline, crystalline) leads to the energetic disorder that directly influences energy transport. In spite of the resulting random nature of the diffusion process [62], energy transport over large distances (>μm) has been reported [63]–[65].

Contrary to molecular organic materials, the bulk material structure of layered transition metal dichalcogenides (TMDs) is formed by the stacking of many monolayers by weak out-of-plane van der Waals force. The constituent monolayers form strong electron-sharing covalent bonds among the atoms in two dimensions and therefore show strong in-plane mechanical stability [66], [67]. These materials are generally represented by the chemical composition MX_2; *M* refers to the transition metal atom; *X* refers to the chalcogen atom. The monolayer in these materials generally consists of three atomic planes. The top and bottom planes contain chalcogen atoms in a triangular lattice configuration. The middle plane is constituted by a transition metal atom in a different triangular lattice configuration [68]. Of the many possible combinations of these materials, group VIB ones have been studied by the research community due to their exotic optical

and electronic properties [69], [70]. These materials can be synthesized in a variety of ways-mechanical exfoliation [71], [72], chemical vapor deposition (CVD) [73], [74], molecular beam epitaxy (MBE) [75]–[77]. As these materials are scaled down from the bulk phase to the monolayer phase, their electronic bandstructure undergoes exciting changes due to the out-of-plane quantum confinement at the two-dimensional limit. For example, these materials show indirect to direct bandgap transition in the monolayer limit [11], [78], [79]. The band extrema (conduction band minima and valance band maxima) for the monolayers are typically located at K points in the hexagonal Brillouin zone. The valance band shows strong spin-orbit splitting due to the presence of heavy metal transition atoms [80]–[82]. The monolayer electronic bandstructure is further complicated by variation of the mixture of the atomic orbitals at different symmetry points in the Brillouin zone– mostly *d* orbitals from the transition metal atoms and the *p* orbitals from the chalcogen atoms [83]–[85]. As multiple monolayers of these materials are stacked together, this complex orbital hybridization further alters the energy of conduction of valance band at different symmetry points, rendering direct to indirect bandgap transition [39], [86]. Reduced dimensional feature at the monolayer level results in significantly weakened dielectric screening from the surrounding environment and strong Coulomb interaction – leading to the formation of room-temperature stable bound *electron-hole* pairs in monolayer TMDs, known as *excitons*. Broken inversion symmetry in the monolayer lattice, orbital hybridization, and strong spin-orbit interaction further give rise to exciting spin-valley properties and optical selection rules [87]–[89]. The excitons in TMDs are not as strongly localized as in organic compounds and show excellent transport properties [90]–[92] due to a well-defined bandstructure. For example, exciton diffusivity

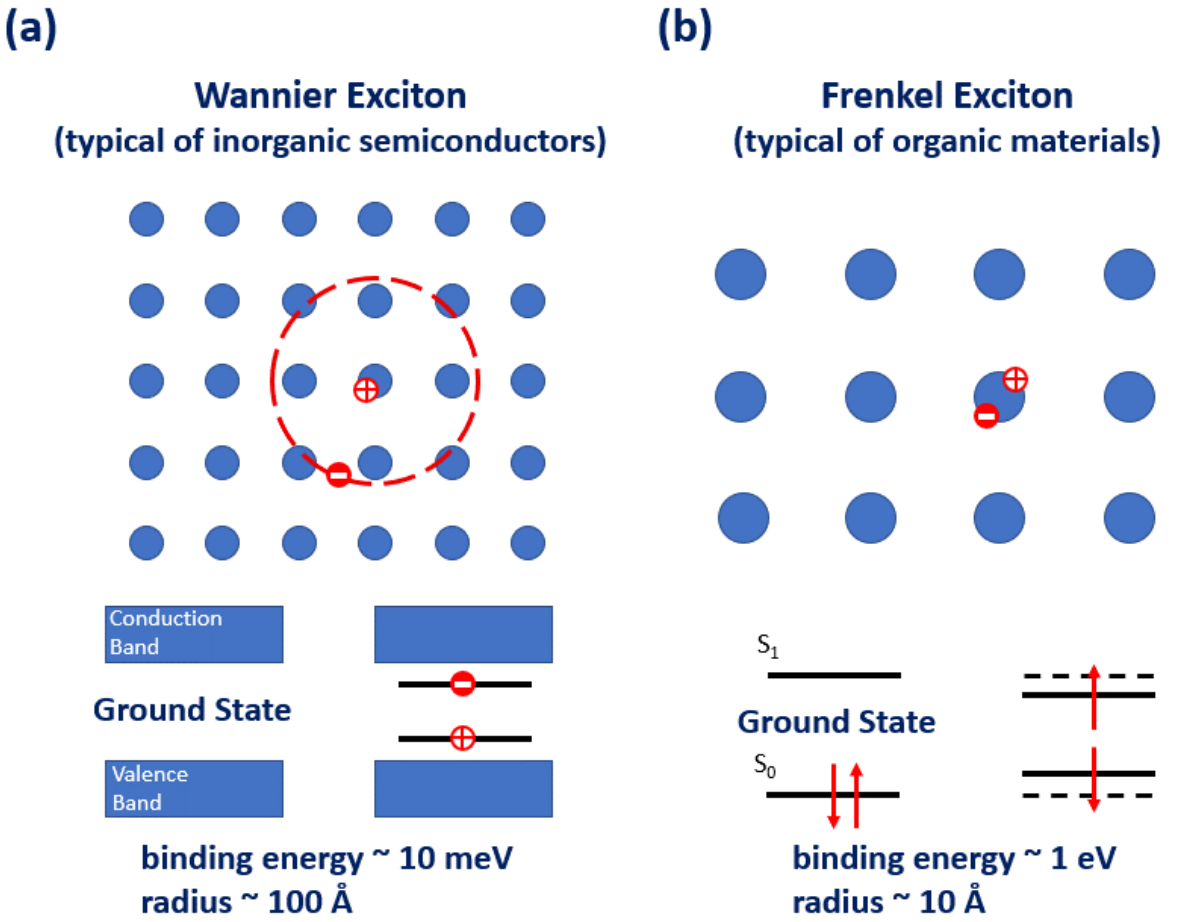

Figure 2-1: Types of excitons in semiconducting media. (a) Wannier type excitons are classically observed in inorganic semiconductors. Such excitons have very low binding energy (~ a few meV) and very large Bohr radius (~ 100 A°), and therefore are not stable at room temperature. They are traditionally observed in small scale III- V semiconducting media like quantum well, quantum dots at cryogenic temperatures. (b) On the other hand, in organic molecular systems, excited states are strongly localized at molecular sites and are therefore strongly bound. Such excitons are stable at room temperature and can have binding energies ranging from several hundreds of meV up to 1 eV. These excitons are referred to as Frenkel excitons.

in TMDs is more than two orders of magnitude higher than that reported for organic semiconductors [62], [93], [94]. The overall transport behaviors, however, are strongly influenced by the surrounding environment and factors, such as impurity and defects [95], [96], energetic disorders [97], surface roughness [98], and dielectric environment [99], etc. The contrasting nature of excitons in organic molecular solids and 2D materials is briefly shown in Figure 2-1.

2.2 Strain-engineered exciton photophysics in organic materials

External pressure has been a widely used tool to perturb the electronic and vibrational spectra of molecular materials and compounds. High-pressure manipulation of physical properties of organic small molecules, conjugated polymers, and their derivates has been studied extensively for a long time [25], [100]. The net effect of external pressure on molecular compounds is to reduce the interaction volume in the medium. External pressure, therefore, reduces intermolecular distance, enhances orbital wavefunction overlap between adjacent molecular sites, and alters the electronic configuration within the molecule. If the pressure is high enough, the molecular structure and the configuration may be altered [26], [27]. Such modifications shift the relative energetic positions of the molecular orbitals which can be measured using optical absorption or fluorescence spectra. A variety of pressure-induced shifts or modifications have been studied in literature such as π electrons in aromatic hydrocarbon crystals, charge transfer between donors and acceptors in molecular complexes, or between ligand and metal in transition metal complexes [100]. The extent of pressure-induced perturbation of electronic spectra in organic molecular semiconductors strongly depends on the nature, geometry, and structure of the molecular compound, nature, and types of intermolecular forces, nature of frontier molecular orbital i.e. bonding or antibonding [101], [102].

The semiconducting properties of conjugated organic compounds and polymers depend strongly on the nature of conjugation among constituent unsaturated units in the polymer chain backbone, the overlapping strength of π orbitals between the molecules of the adjacent chains [15], [103]. Pressure-induced photophysics in these materials, therefore, provides important insights into the nature of structural morphology of the organic polymer, reconfiguration of the polymer backbone [104], [105], the intermolecular interaction within the polymer chain (intra-chain

interaction) [106], [107], inter-chain interaction and so on. In general, all π conjugated polymers show a characteristic redshift in photoluminescence under pressure, which is in stark contrast to inorganic semiconductors. As polymers are compressed, a strong intermolecular interaction due to increased overlap of the π- orbital wavefunctions within the polymer chain leads to increased conformational ordering. This results in a reduction of excited-state energy and eventually a redshift in the photoluminescence [106], [108]. The experimentally observed pressure coefficients for different vibrionic transitions suggest a strong influence of the backbone conformation on the pressure-induced photophysics. The energetic redshift in the electronic transition under pressure is often followed by planarization of the polymer backbone which leads to possible phase transition or co-existence of two different phases in the same polymer system [109], [110]

Along with redshift in the photoluminescence (PL) spectra, the linewidth broadening under pressure shed light on strong interchain and intermolecular interactions in the polymer. Such linewidth broadening strongly depends on the conformation of the polymer backbone, the crystallinity of the polymer structure, molecular weight of the polymer [105], [111]. Increased pressure also opens up an additional non-radiative decay channel accelerated by increased interaction between adjacent polymer chains in the material [112], [113].

Weak electrostatic forces within the molecular chains result in low dielectric constant and therefore, increased exchange-interaction in organic semiconductors. This also leads to highly localized long-lived triplet excited states [114]. In addition to modulation of singlet excited state properties, external pressure also modifies the energetic configuration of long-lived spin unpaired triplet excited states in organic polymers. The energetic modification of the triplet excited states is manifested in the observed redshift in the triplet-triplet absorption using photo-indued absorption spectroscopy [115]. In comparison to energetic modification of the singlet excited states, the triplet

states show a much weaker redshift under pressure, which is attributed to their localized nature [15], [111]. In addition, the narrowing linewidth of triplet-triplet absorption under pressure also shows reduced conformational freedom as the molecules come closer together [116].

The excited state photophysics of organic molecules is strongly affected by a local change in the dielectric environment. Emission from the molecular excited state shows a pronounced redshift as the polarization field in the background environment increases. In solid-state thin films, this phenomenon is known as solid-state solvation. Although the conventional method of triggering such a phenomenon has been changing the doping of highly polar guest molecules in a relatively non-polar host matrix, recent work from Cheng and co-workers showed, for the first time, the solvatochromic shift in molecular thin films can take place under external pressure [14]. Using a motorized mechanical pressure stage, a pronounced spectral redshift was shown in two different guest: host media – PS: DCM2 and Alq_3: DCM2 [14].

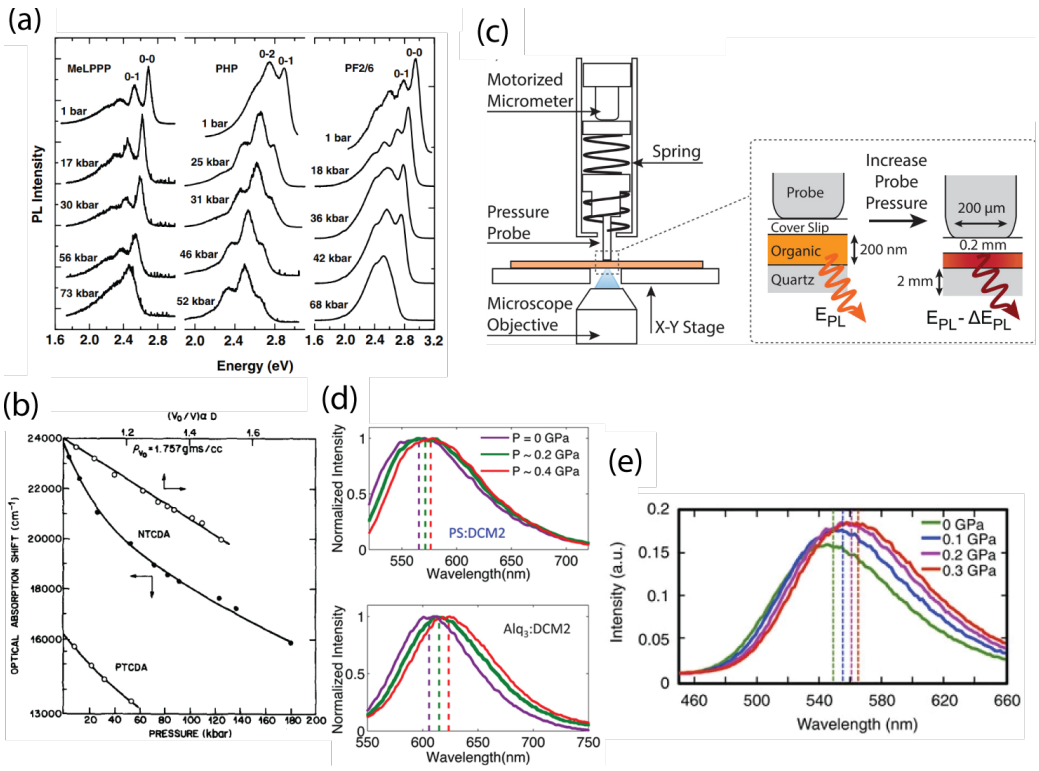

Figure 2-2: Pressure induced photophysical manipulation in organics. (a) Pressure induced photophysical change in conjugated polymers at 300K. The photoluminescence from polymers show redshift under increased pressure due to increased wavefunction overlap between molecules alongside pressure induced smearing of the vibrionic progression. *Reprinted (adapted) with permission from Guha, S., and M. Chandrasekhar. "Photophysics of organic emissive semiconductors under hydrostatic pressure." physica status solidi (b) 241.14 (2004): 3318-3327.* (b) Shift in optical absorption spectra for thin films of small molecule organics PTCDA and NTCDA under pressure. A gradual redshift is observed under pressure in both the molecules. *Reprinted (adapted) with permission from Jayaraman, A., M. L. Kaplan, and P. H. Schmidt. "Effect of pressure on the Raman and electronic absorption spectra of naphthalene-and perylenetetracarboxylic dianhydrides." The Journal of chemical physics 82.4 (1985): 1682-1687.* (c) Experimental set-up for in-situ photoluminescence measurement from an organic thin film under pressure. The motorized micrometer and the spring together apply a linear pressure on the thin film sandwiched between quartz substrate and a cover slip. (d) Dynamic pressure induced solvatochromic shift in PS: DCM2 and Alq_3: DCM2 systems. A clear pronounced red shift is observed as a function of pressure in both thin films. (c) and (d) - *Reprinted (adapted) with permission from Chang, Wendi, Gleb M. Akselrod, and Vladimir Bulovic. "Solid-state solvation and enhanced exciton diffusion in doped organic thin films under mechanical pressure." ACS nano 9.4 (2015): 4412-4418. Copyright 2015 American Chemical Society.* (e) Pressure induced spectral red-shift in a donor: acceptor blend (1:1 m-MTDATA: 3TPYMB). The redshift in photoluminescence is attributed to both solvation and reduced molecular proximity under increased pressure. *Reprinted (adapted) with permission from Chang, Wendi, et al. "Spin-dependent charge transfer state design rules in organic photovoltaics." Nature communications 6.1 (2015): 1-6.*

2.3 Strain engineered exciton photophysics in inorganic van der Waals materials

Strain engineering has long been used as a powerful tool for enhancing the performance of semiconductor electronic and optoelectronic devices [43], [117]–[120]. As seen in traditional bulk semiconductors, the electronic bandstructure of TMD monolayers demonstrates sensitivity to externally applied mechanical strain albeit the sensitivity is much stronger. For instance, while the excitonic deformation potential modulation in ZnO microwires is about 27.3 *meV/%* [121], monolayer TMDs show modulation in excess of 45 *meV/%* [122]. Theoretical bandstructure calculation predicts a lowering of bandgap in these material monolayers with increasing tensile strain and an eventual transition from semiconducting to metallic phase at high enough strain amplitudes [84], [123]. This gradual lowering of the bandgap is not typically accompanied by equal modulation of quasiparticle energies at the conduction and valance band extrema [124], [125] i.e. the conduction and valence band energies at their respective extrema do not get modulated equally under strain. Furthermore, external strain modifies the energy band curvature at different symmetry positions leading to changes in the carrier effective mass at different valleys [126], [127]. Recent experimental reports on strained layered semiconductors have led to many new opportunities and challenges for fundamental physical investigations and exciting device applications [12], [128], [129].

In strain engineering, 2D semiconductors offer a unique advantage over their bulk counterparts due to their ability to withstand large mechanical deformation [40], [43], [128], [130] For instance, monolayer MoS_2 has been reported to withstand external strain greater than 10% while the direct to indirect bandgap transition point reportedly occurs at 2%. The monolayer finally undergoes semiconducting to metallic phase transition at tensile strains of about 10-15% [123], [131]. On the contrary, bulk materials like silicon can only sustain strains up to 1.5% [83]. Strain

engineering also modifies the enriched excitonic properties in the monolayer TMDs. A direct consequence of bandgap modulation under strain is observed from the measurement of the excitonic photoluminescence (PL) and absorption spectra [43], [132], [133]. For instance, the absorption spectra of monolayer WSe_2 reportedly show uniaxial strain tunability of about 47 mev/% - 60 meV/% [134], [135] on an absolute scale, determined from experiments. Besides, external strain causes modification in the exciton-phonon scattering in the monolayer [136], evident from the strain modulation of exciton linewidth [134], [137], increases exciton population in the lower-energy *K* valley by reducing *KQ* intervalley exciton scattering and, enhances the radiative recombination rate of *K* valley excitons, resulting in an increase in the PL emission [48].

In recent years, several approaches have been followed and studied by research groups across the world for controlled strain application on TMD monolayers. One of the most common approaches includes controlled bending of flexible substrates like polydimethylsiloxane (PDMS) [45][138], polyethylene terephthalate (PET) [139], polyethylene napthalate (PEN) [140] etc. following the mechanical transfer of the monolayer. The advantages of the flexible substrate approach include possible dynamic control over the applied strain, reproducibility, ease of operation, possible application of both compressive and tensile strain using the same substrate, and many more [42], [128]. However, the poor strain transfer efficiency of substrates with low Young's modulus, and monolayer slippage due to weak van der Waals interaction during the bending process are some of the limitations of such a method [128]. A more controlled approach has been demonstrated by the usage of micro-mechanical actuation [46], [141]. The mechanical transfer of TMD monolayers on pre-patterned substrates has been another widely studies way to apply large strains on the monolayers. Using nanofabrication techniques like lithography, ion-

etching, wet etching, ion- milling, and deposition various types of surface structures like periodic ripple [142], nano-pillar [94], [143]–[145], nano-cone [146] have been fabricated on traditional Si substrates. More recently, III-V nanowires have been used to create uniform strain over monolayer TMDs [147]. Other methods of applying large strains in monolayer TMDs include wrinkle generation by using elastomeric substrates [45], [148], proton-irradiation [149].

Solid-state single photon emitters or quantum emitters find their application niche in technologies like computing, sensing, metrological investigation, and so on [150], [151]. Strained monolayer TMDs have been explored as an attractive media for quantum confined light sources due to their strong light-matter interaction, scalability, large elastic deformation limit, and promise for integration with nano-scale on-chip photonic platforms [152]. Such quantum emitters are realized by transferring TMD monolayers on top of pre-patterned geometries like nanopillars [143], [144], etched patterns [153], monolayer nano-indentation [154], gate electrostatics [155], [156], artificial functionalization for transition to other excitation modes [157], [158]. More recently, quantum emitters operating up to the range of 150K through strain engineered emission from defect states have been demonstrated in monolayer WSe_2 [159].

As excitons are charge-neutral species, they are not influenced by a spatial electric field gradient. However, directional exciton flux control can be achieved under a spatial modulation in the exciton energy landscape i.e., exciton potential. A spatial modulation in exciton potential would exert a directional force on an exciton resulting in drift velocity, $v = \mu \frac{dU}{dx}$; where $v, \mu, \frac{dU}{dx}$ refer to the exciton velocity, mobility, and exciton potential respectively. Since external strain modulates the band structure of TMD monolayers and therefore, the exciton potential, directional exciton transport can be achieved by applying a non-uniform strain gradient in an excitonic semiconducting medium. Fu and co-workers reported the first experimental observations on the

dynamics of excitons in bent ZnO microwires [121] using picosecond resolved cathodoluminescence. Due to their giant bandgap tunability, flexible nature, and ability to withstand large mechanical deformation and strong light-matter interaction, TMDs are also an attractive platform for studying directional exciton transport under a non-uniform strain gradient – a phenomenon commonly referred to as *exciton funneling* [48], [124], [160], [161]. Room temperature exciton funneling in TMD monolayers has been experimentally reported using patterned substrates [94], controlled nano-scale deformation under AFM tips [48], or metallic probes [49]. Under high strain, such funneling can also lead to quasiparticle inter-conversion [47]. However, the efficiency of such a funneling process is limited by the balance between drift and diffusion processes at thermal equilibrium, exciton lifetime in the medium under study, and non-radiative recombination processes that dominate at high excitation density [162]. At room temperature, the theoretical limit of such a funneling process has been reported to be 50% which can be further improved at low temperatures where exciton drift dominated over diffusive transport [162]. The funneling efficiency and the transport distance can be largely improved by using TMD hetero bilayers with a long radiative lifetime [163], [164]. Some key results of strain tuned exciton modulation in inorganic layered semiconductors from different research groups are summarized in Figure 2-3 and Figure 2-4.

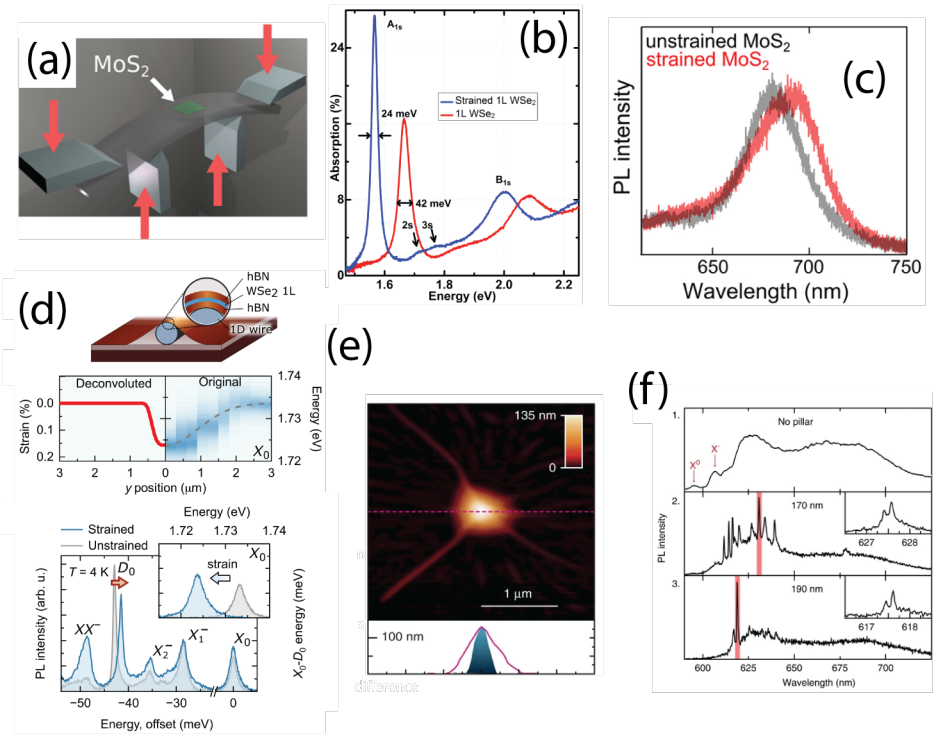

Figure 2-3: Static strain induced excitonic photophysical manipulation in TMDs. (a) Schematics of strain application on monolayer TMD by bending flexible substrates. *Reprinted (adapted) with permission from Conley, Hiram J., et al. "Bandgap engineering of strained monolayer and bilayer MoS_2." Nano letters 13.8 (2013): 3626-3630. Copyright 2013 American Chemical Society.* (b) Absorption spectra of strained (2.1%) and unstrained monolayer WSe_2. The strained monolayer absorption shows a clear redshift and reduction in linewidth due to bandgap reduction and reduced exciton-phonon coupling. *Reprinted (adapted) with permission from Aslan, Ozgur Burak, Minda Deng, and Tony F. Heinz. "Strain tuning of excitons in monolayer WSe_2." Physical Review B 98.11 (2018): 115308.* (c) Strain induced exciton photoluminescence modulation in monolayer MoS_2 that shows a clear redshift. *Reprinted (adapted) with permission from Castellanos-Gomez, Andres, et al. "Local strain engineering in atomically thin MoS_2." Nano letters 13.11 (2013): 5361-5366. Copyright 2013 American Chemical Society.* (d) Local strain profile as a function of spatial co-ordinates normal to the nanowire direction. The nanowires are used to strain the monolayer. The bottom panel shows the PL spectra of strained and unstrained monolayer flake as a function of energy relative to the neutral exciton (X_0) resonance. The neutral exciton (X_0) PL spectra for strain and unstrained monolayer is shown in the inset figure. *Reprinted (adapted) with permission from Dirnberger, Florian, et al. "Quasi-1D exciton channels in strain-engineered 2D materials." Science advances 7.44 (2021): eabj3066."* (e) AFM micrograph of a monolayer WSe_2 transferred on a nanopillar geometry. The AFM line profile of the pillar (shaded blue) and the monolayer flake (pink line) are shown in the bottom figure. (f) PL spectra of 1L-WS_2 at 10 K. The PL spectra taken on an unstrained region (panel 1) shows no fine peak features. Panels 2 and 3 shows the PL spectra from monolayer WS_2 on 170 and 190 nm nanopillars respectively. (e) and (f) - *Reprinted (adapted) with permission from Palacios-Berraquero, Carmen, et al. "Large-scale quantum-emitter arrays in atomically thin semiconductors." Nature communications 8.1 (2017): 1-6.*

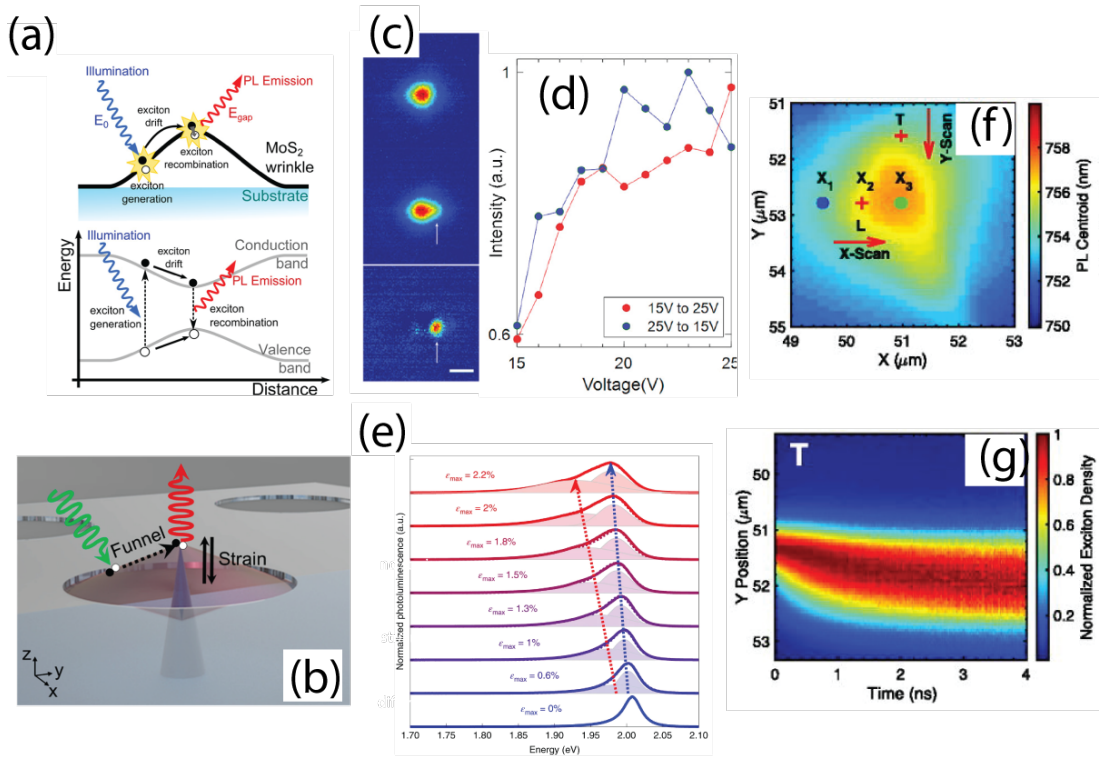

Figure 2-4: Static strain induced exciton transport in monolayer TMDs. (a) Schematics of strain induced exciton funneling in monolayer TMD under local tension. Excitons *funnel* towards the position of minimum energy and undergo radiative recombination there, enhancing the PL emission. *Reprinted (adapted) with permission from Castellanos-Gomez, Andres, et al. "Local strain engineering in atomically thin MoS_2." Nano letters 13.11 (2013): 5361-5366. Copyright 2013 American Chemical Society.* (b) Schematic illustration of generating dynamically controlled local strain in monolayer TMDs using an AFM tip. (c) Experimental results of exciton *funneling* under AFM tip induced strain in monolayer WSe_2. The CCD images show PL intensity without (top), and under AFM indentation (middle) on the monolayer. The bottom image shows the difference that shows the funneled fraction of excitons. The scale bar is 1 μm. (d) Reversible control over PL excitation due to exciton *funneling* under AFM indentation. (b), (c), and (d) - *Reprinted (adapted) with permission from Moon, Hyowon, et al. "Dynamic exciton funneling by local strain control in a monolayer semiconductor." Nano Letters 20.9 (2020): 6791-6797. Copyright 2020 American Chemical Society.* (e) Normalized PL spectra from monolayer WS_2 under strain that shows a clear shift. Two gaussian fitting of the PL spectra at different strain levels show conversion from exciton to trion under large strain in the monolayer. *Reprinted with permission from Harats, Moshe G., et al. "Dynamics and efficient conversion of excitons to trions in non-uniformly strained monolayer WS_2." Nature Photonics 14.5 (2020): 324-329.* (f) Room temperature PL centroid map of a monolayer WSe_2 transferred on a SiO_2 nano-pillar pattern that shows clear redshift at the position of the nano-pillar. (g) Normalized exciton density extracted from diffusion measurement at room temperature. The measurement position is marked in (f). The exciton flux shows a clear drift towards the position of maximum strain on the monolayer alongside diffusive transport at room temperature. (f) and (g) - *Reproduced from Cordovilla Leon, Darwin F., et al. "Exciton transport in strained monolayer WSe_2." Applied Physics Letters 113.25 (2018): 252101, with the permission of AIP Publishing.*

Although spatially varying static strain provides a unique way of directing exciton flux in semiconductors, traveling strain wave can also be used to achieve directional exciton transport. Such traveling strain waves can be generated by surface acoustic waves (SAW) propagating on piezoelectric substrates [165], [166]. The dynamic strain generated by such a propagating surface wave produces an out-of-phase band edge modulation in a semiconducting media, resulting in periodic modulation of exciton potential, thereby creating potential pockets moving at a velocity of the SAW wave [52], [167]. Such out-of-phase modulation is commonly referred to as type- I modulation. Using such a scheme, Rudolph et al. [53], [167] demonstrated the transport of indirect excitons up to several hundreds of μms at cryogenic temperatures. Such long-range transport is primarily attributed to the long recombination lifetime of indirect excitons in the III-V quantum well system, which can extend up to several hundred on ns [168], [169] and high low-temperature intrinsic exciton mobility which allows efficient coupling of photogenerated excitons to the traveling potential lattice [53], [170]. Such long rage transport phenomenon has been successfully extended for the realization of scalable interconnects at cryogenic temperatures [54]. More recently, such a traveling acoustic field has been successfully used to achieve long-range exciton transport in TMD monolayers [171] and hetero- bilayers [55]. Some key results of surface acoustic wave-mediated exciton transport in III-V semiconductors and TMDs are summarized in Figure 2-5.

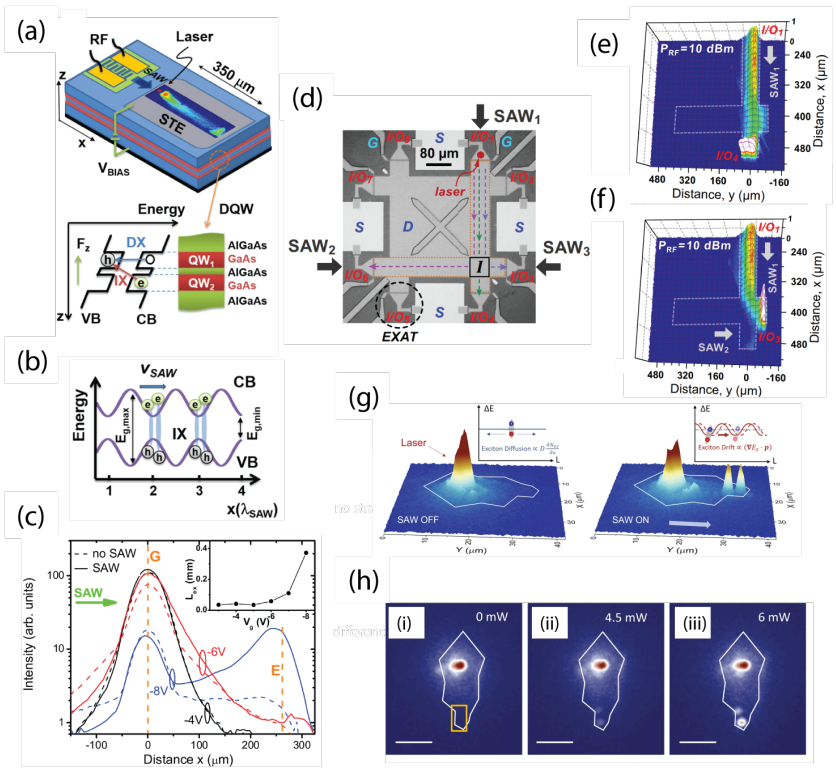

Figure 2-5: Acoustic field induced manipulation of excitons. (a) Schematic illustration of the GaAs/ AlGaAs device geometry with the patterned IDTs and the generation and excitation positions. The prolonged lifetime of the indirect excitons is sustained along the channel by applying an out-of-plane electric field. (b) Schematic illustration of type – I band edge modulation where the conduction and valance bands are modulated out of phase under strain. (a) and (b) - *Reprinted (adapted) with permission from Violante, Adriano, et al. "Dynamics of indirect exciton transport by moving acoustic fields." New Journal of Physics 16.3 (2014): 033035*. (c) Spatial PL profiles from indirect excitons for different gate voltages Vg in the absence (dashed lines) and presence (solid lines) of a SAW with P_{rf}24 dBm. The inset shows the diffusion length L_{ex} extracted from the decay of the profiles towards negative X. *Reprinted (adapted) with permission from Rudolph, J., R. Hey, and P. V. Santos. "Long-range exciton transport by dynamic strain fields in a GaAs quantum well." Physical Review Letters 99.4 (2007): 047602.* (d) Cryogenic excitonic multiplexing circuit based on the concept of dynamic strain induced exciton transport. Acoustic transport of IX excitons under 10 dBm RF excitation at (e) input port 1 (SAW_1) and (f) input ports 1 and 2 (SAW_1 and SAW_2 inputs are active at the same time). (d), (e), and (f) - *Reprinted (adapted) with permission from Lazić, S., et al. "Scalable interconnections for remote indirect exciton systems based on acoustic transport." Physical Review B 89.8 (2014): 085313.* Long range exciton transport under dynamic strain in 2D heterostructure at 100 K. (g) When the SAW is off the indirect excitons shows diffusive transport behavior. As the SAW is turned on, two bright peaks appear at the far end of the flake due to the exciton transport by dynamic acoustic lattice. (h) Acoustic lattice mediated exciton transport in TMD heterostructure under different RF excitations (i) 0 mW (ii) 4.5 mW (iii) 6 mW. (g) and (h) - *Reprinted (adapted) with permission from Peng, Ruoming, et al. "Long-range transport of 2D excitons with acoustic waves." Nature communications 13.1 (2022): 1-7.*

Chapter 3 Strain Tuned Solvatochromism in a Molecular Host: Guest Blend

3.1 Authorship and copyright disclaimer statement

The contents of this chapter were published in ACS Applied Nanomaterials in December 2019 [172] and Optical Materials Express in December 2020 [173]. I retain the rights to include the results and contents of the publications in this dissertation provided that it's not used commercially. The other co-authors were Parag B Deotare from the University of Michigan, Ann Arbor, Michigan, USA.

3.2 Background

In recent years, organic semiconductors have been extensively used in electronic, optoelectronic, and photovoltaic devices due to their unique photo-physical properties such as tunable energy gap, high exciton binding energy, and thermal independence along with the mechanical flexibility and compatibility with large-scale continuous production processes such as roll-to-roll printing and solution processing [174]–[178]. Particularly, in applications demanding mechanical flexibility and light weight such as wearable devices, organic materials offer unique advantages over their inorganic counterparts [179]–[181]. However, since the molecules in organic semiconductors are held together by weak van der Waals forces, the elastic properties of an organic thin film can largely vary from its bulk form [182]. To harness the full potential of organic

materials for flexible thin film nanoscale devices, a proper understanding and knowledge of mechanical properties such as elastic modulus are important.

Over time, various techniques and methods have been employed to estimate the elastic modulus of organic thin films (both polymers and small molecules), with reported values ranging from 1-120 GPa [181], [183]–[189]. Such a large discrepancy mostly stems from the dependence and interaction of the measurement technique with the substrate material. For instance, buckling techniques based on the formation of sinusoidal wrinkles on a compliant substrate rely on the elastic modulus of the compliant substrate [183]–[185]. Another standard method to determine the elastic modulus of thin films is nanoindentation, which consists of applying a load and measuring the displacement of the indenter to determine the mechanical properties of the thin films. This technique too is strongly affected by the nature of the substrate material due to the substrate-indenter interaction [188]. In addition, the difference in the thin film density and aggregate formation that may occur during the vacuum deposition of thin films on substrates could also trigger a discrepancy in elastic modulus estimation [188]. The difference in molecular packing and distribution in bulk and thin film forms could also trigger changes in the measured elastic properties. For instance, a 70% increase in elastic modulus was observed as the thickness of vapor-deposited Tris-(8-hydroxyquinoline)aluminum (Alq_3) thin film was reduced to 10 nm [187]. In addition, time of flight-based techniques such as laser-generated surface acoustic waves as well as picosecond ultrasonics has been successfully used to determine the elastic properties of low-dielectric constant(low-k) material. [165], [190]–[194] However, both the techniques are limited to certain thicknesses of films. [193], [195]. Another non-contact approach is based on Brillouin Light Scattering (BLS), where experimentally measured dispersion of acoustic phonon modes in a thin film medium is used to extract elastic properties [195]–[197]. This method requires

knowledge about the mass density of the thin film which could be different in bulk and thin film forms [195]. Some other non-contact methods reported include those based on ellipsometric porosimetry [198], [199] and elastocapillary bending [200]. Besides experimental methods, the elastic modulus of organic small molecules has also been computed using molecular dynamics simulation which further adds to the discrepancy [189]. In this work, we report a non-invasive technique based on strain-generated solvatochromism in a solid-state organic medium that overcomes some of the underlying issues discussed earlier and can be used for bulk as well as thin films.

We use the residual stress in silicon dioxide (SiO_2) thin films to generate controlled axial strain on an overlying organic thin film. Residual stress is generated due to differential thermal expansion of the substrate and the thin film during the growth phase. The microbeams were patterned on the substrates using optical lithography, followed by reactive ion etching, and released from the substrate using a gas-phase etching process, followed by the evaporation of the organic thin film. Please refer to Appendix A for detailed fabrication steps. From our measurements, we show that microbeams fabricated on a thin film under residual stress can generate as high as 1% local strain when released from the substrate. The elastic modulus of the organic thin film was extracted by fitting a model based on solid-state solvation with the observed shift in the photoluminescence (PL) spectrum of the strained organic thin films. We further verify the estimated value by dynamically tuning the tensile strain on the organic thin film using a MEMS device fabricated on low stress, low-pressure chemical vapor deposited (LPCVD) silicon nitride (Si_3N_4) platform. In the current work, we choose to work with Tris-(8-hydroxyquinoline)aluminum (Alq_3) and 4-(Dicyanomethylene)-2-methyl-6-(4-dimethylaminostyryl)-4H-pyran (DCM) as a representative of a guest: host system of organic semiconductors. Alq_3 is widely used as an electron

transport layer as well as an active emission layer in organic light-emitting diodes (OLEDs) [201]. Further, the emission wavelength and the electroluminescence efficiency of Alq_3 based OLEDs can be modulated by introducing small molecule dopant materials in specific concentrations and thereby changing the non-radiative energy transfer from host Alq_3 molecules to guest dopant molecules [202]. In this regard, DCM has been widely used as a luminescent red dopant in Alq_3 host matrix due to high Förster energy transfer efficiency [203], [204]. Hence, we believe that estimation of mechanical properties of such a representative system using an optical non-contact approach could be helpful for flexible optoelectronic device applications.

3.3 Estimating axial strain along a buckled SiO_2 microbeam

The axial strain along the microbeam axis was measured using white light interferometry and polynomial fitting of the out-of-plane deflection of the microbeam [172]. The 2D surface map of a representative microbeam obtained using white light interferometry is shown in Figure 3-1(a). The maximum out-of-plane deflection and tensile strain at the point of maximum deflection for different beam lengths are shown in Figure 3-1(b). Although, out-of-plane microbeam deflection increases as the beam length increases, the resulting axial strain at the maximum deflection point decreases with beam length. The measurements show that the microbeam geometry can generate an axial strain of about 0.9% at the position of maximum deflection which is lower than the reported yield strain of Alq_3, extracted from atomistic simulation [189]. In addition, the generated axial strain is lower than the strain applied in most bucking-based methods as well as the reported yield point for similar small-molecule organic materials [183], [185], [205], [206]. Since the maximum strain applied in this work is within the yield limit of the thin film under study, the mechanical properties of the organic thin film in this work are expected to be governed by the linear regime of the stress-strain relationship. Figure 3-1(c) – (e) shows the out-of-plane deflection

(obtained from the 2D surface map and polynomial fitting), the radius of curvature, and the axial tensile strain respectively, along the linear section, labeled M – N in Figure 3-1(a).

Due to the uneven nature of gas-phase XeF_2 etching [207], the microbeams tend to deflect asymmetrically when released. This deflection may be non-uniform along the normal to the beam axis as can be found elsewhere [172]. This asymmetric deflection could also strain the thin film normal to the beam axis. We extracted the strain profile along the normal to the beam axis at the position of maximum deflection [172]. Along the normal direction, the measured surface profile does not show any significant curvature and hence the strain along this direction was found to be negligible. Therefore, any modulation in the emission spectrum of the organic thin film is expected to be dominated by the axial strain on the deflected microbeam. Besides the generated strain being lower than the yield point of the thin film, from our estimation, the force on the fluorescent organic emitters generated by the axial tensile strain is insufficient to cause any change in the molecular structure or strain in the molecular bonds [172].

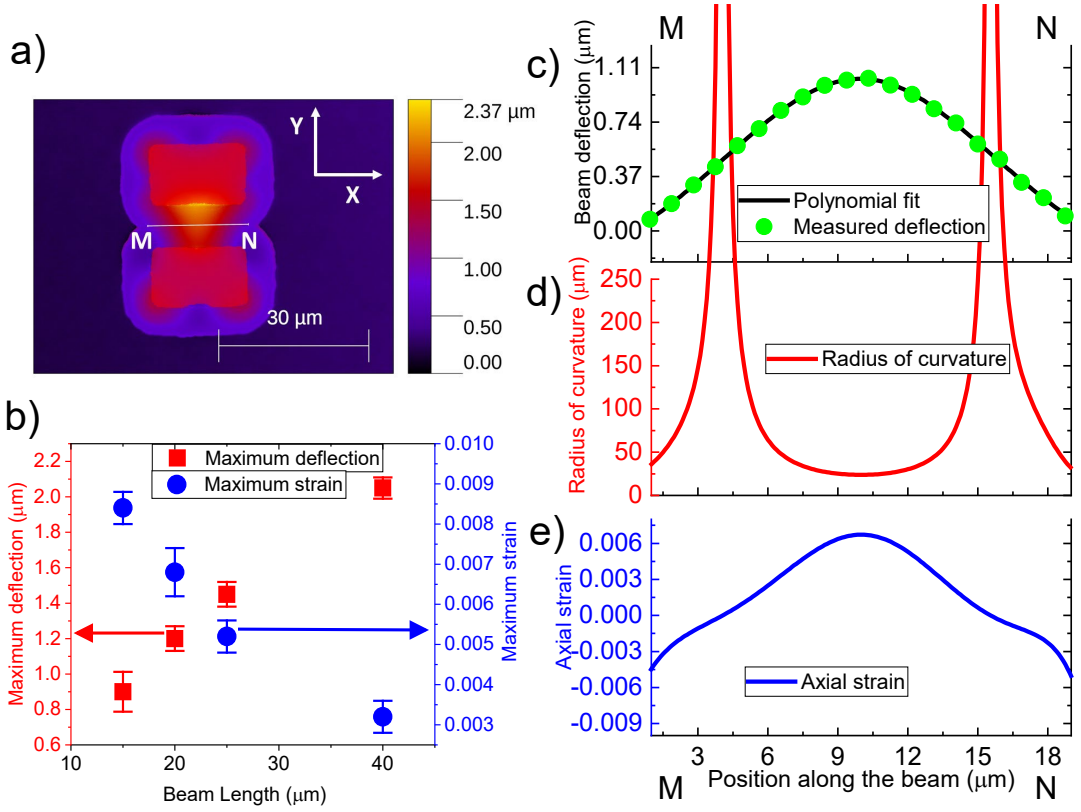

Figure 3-1: Axial strain on buckled SiO_2 microbeam: (a) Surface profile of a doubly supported SiO_2 microbeam released by gas-phase XeF_2 etching step. The surface profile is extracted using non-contact white light interferometry. (b) Maximum deflection of buckled microbeam, and the corresponding axial strain measured at the maximum defection point for different beam lengths. The axial strain at maximum deflection point decreases with increased beam length. (c) Deflection profile of the buckled microbeam shown in (a), along a linear section labeled M-N, through the middle of the buckled beam. The figure also shows a polynomial fit of the extracted surface profile along the linear section. (d) Radius of curvature extracted from the fitted deflection profile. (e) Axial strain profile calculated from the radius of curvature using the formulation discussed in the text.

3.4 Solid-state solvation in a strained amorphous organic thin film

In our study, we use Alq_3: DCM as an archetype host: guest system (Figure 3-2(a) and (b)) [208]–[210]. DCM molecules suspended in a relatively non-polar Alq_3 background matrix undergo solid-state solvation (under no mechanical stimuli) which triggers a pronounced redshift of the emission spectrum. Following the electronic transition by absorption of a photon, the solute molecules reach an initial excited state commonly referred to as the Franck- Condon state [211]. For molecules having a large transition dipole moment, an equilibrium excited state is established by the interaction between the excited solute molecules and the surrounding electrostatic medium. In a doped host: guest medium, this local polarizable medium is created by polar guest molecules and the local electric field becomes stronger with guest doping. This phenomenon is called self-polarization. Figure 3-2(c) shows a simple schematic of the mechanism of solvatochromism in an amorphous organic thin film under external mechanical tension. As the thin film is axially stretched, the local molecular density decreases triggering a decrease in self polarization and a reduction in the energy required for relaxation from the short-lived Franck-Condon state. As a result, a blueshift in the emission spectrum of the molecule is observed. From the measured spectral variation of DCM emission and axial strain on the thin film, we can extract the spatial modulation of the dielectric polarizability under axial strain and estimate the strain sensitivity of dielectric polarization in the host: guest medium.

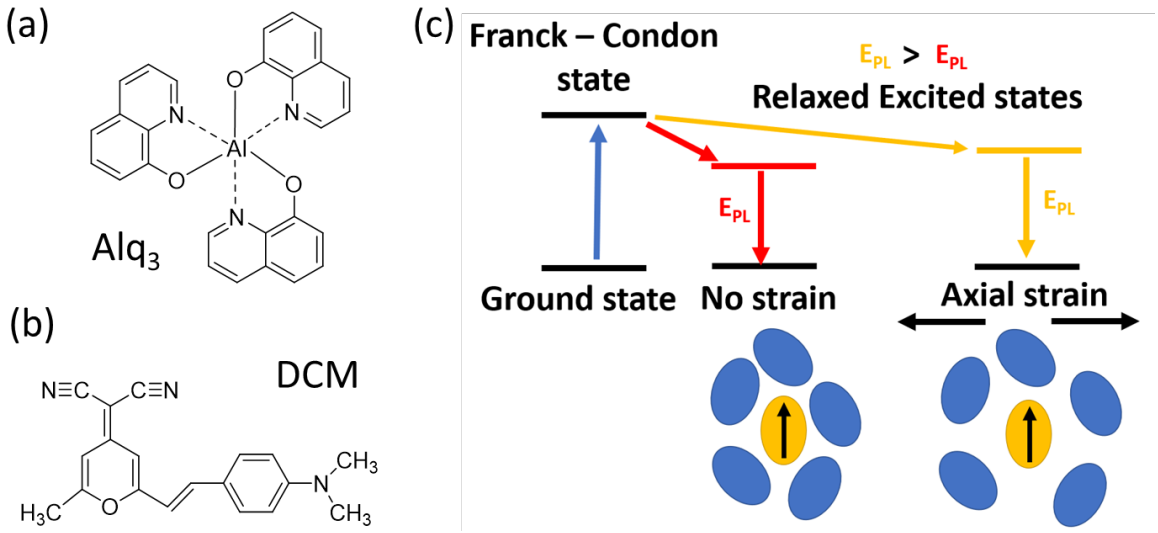

Figure 3-2: (a) Molecular structures of the materials used in this work: (a) Alq_3 & (b) DCM. (c) Simple schematic representation of solid- state solvation under tensile strain. Here the center molecular dipole is shown to be surrounded by solvent molecules. Under tensile strain, the molecular density decreases and the resulting reduction in self-polarization triggers a blueshift in the emission of DCM molecules at a specific doping.

The solvatochromic spectral shift due to solute-solvent interaction in a dielectric medium is generally represented by the Lippert- Mataga equation [212], [213]:

$$\upsilon_a - \upsilon_f = \frac{2}{hc}\left(\frac{\varepsilon-1}{2\varepsilon+1} - \frac{n^2-1}{2n^2+1}\right)\frac{(\mu_E-\mu_G)^2}{a^3} + C \qquad \text{(Equation 3.1)}$$

Here, υ_a and υ_f refer to the peak absorption and emission wavenumbers of solute molecule in cm^{-1}, ε and n refer to the dielectric constant and refractive index of the surrounding solid-state solvent medium respectively, h and c refer to the Planck's constant and the speed of light respectively, μ_E and μ_G refer to the dipole moment of the solute molecules in the excited and ground-state respectively, a is the radius of the cavity from Onsager reaction field theory [214],

and *C* refers to a constant that represents the unperturbed spectral shift of the solute emission. The term $\frac{\varepsilon-1}{2\varepsilon+1}-\frac{n^2-1}{2n^2+1}$ generally referred to as the orientational polarizability [215], represents the local dielectric polarization of the medium. The first term $\frac{\varepsilon-1}{2\varepsilon+1}$ represents the effect on Stokes shift due to both electronic and molecular reorientation of the solvent dipoles around the excited solute molecules. On the other hand, the second term $\frac{n^2-1}{2n^2+1}$ represents the high-frequency response due to electronic re-orientation. Therefore, the difference between the two terms accounts for the net dielectric polarization due to molecular reorientation in a solute-solvent medium. In solid-state doped thin films, orientational polarizability increases as the concentration of polar guest molecules in a relatively non- polar background host matrix is increased.

Figure 3-3 shows the effect of axial strain on the emission properties of Alq_3: DCM thin film for 1.5% DCM doping. Figure 3-3(a) shows false-color SEM micrographs of representative SiO_2 released microbeams with an overlying organic thin film. Figure 3-3(b) shows normalized PL intensity profiles at three different positions on the microbeam – positions M, N, and P. Figure 3-3(c) shows the axial strain along the microbeam calculated from the out-of-plane deflection. Due to the nature of deflection, the strain generated along the microbeams can range from 0.2 - 0.3% compressive (at the anchor position) to about 0.9% tensile (at the position of maximum deflection). In Figure 3-3(c), positions M & N represent the location of zero strain on the released microbeams. Position P represents the maximum strain location on the beam and the position of maximum out-of-plane deflection. From the figure, we see that the axial strain gradually increases as we approach position P from position M, reaches the maximum value at position P (~0.9%), and gradually decreases as we approach position N. Figure 3-3(d) shows the peak photoluminescence emission wavelength measured along the microbeam on the left y-axis. We observe a gradual blueshift in the peak emission wavelength from the zero strain positions (M & N) to the maximum strain

position (position P). We observe a blueshift of nearly 6 nm for an axial tensile strain of about 0.9 % (also seen in Figure 3-3(b)) as a result of solvatochromism under tensile strain. We note that no significant change in the PL linewidth was observed, suggesting that the axial strain did not affect the homogeneous distribution of molecules in the host: guest medium. We also estimated the axial strain profile and the measured peak emission wavelength of DCM for 2.5% and 5% doped thin films [173].

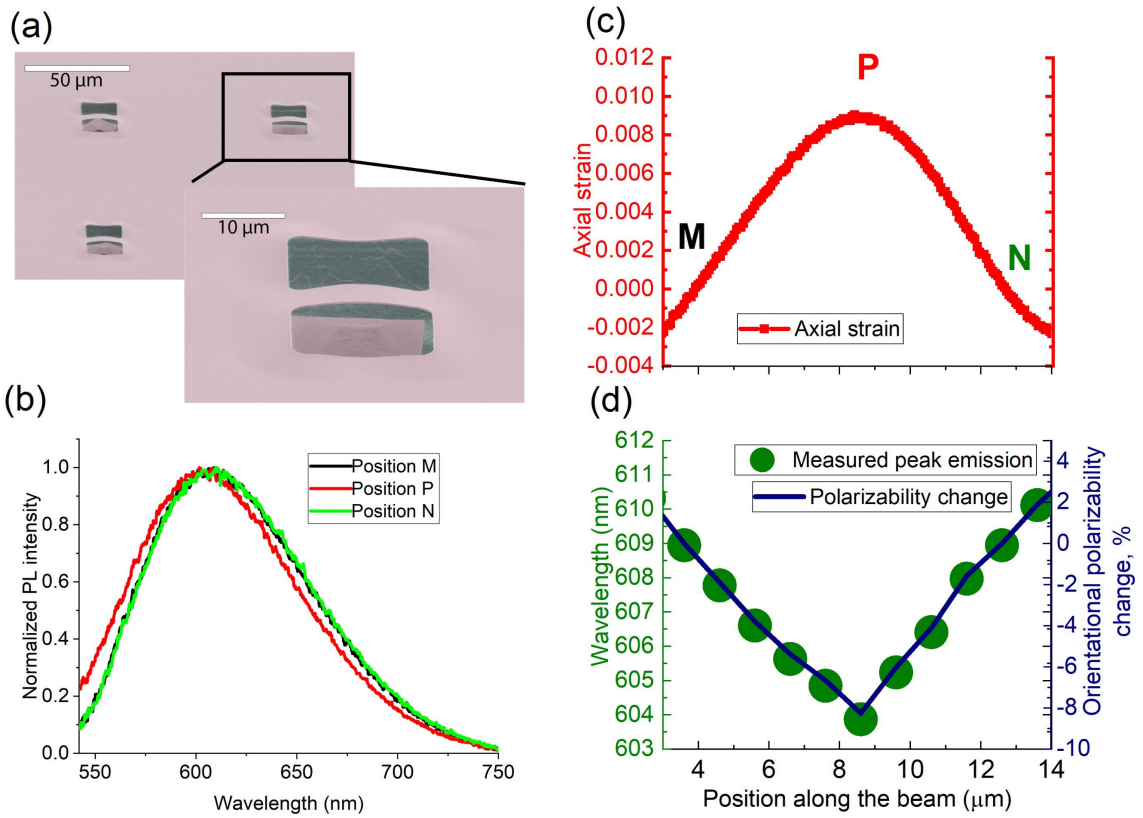

Figure 3-3: Effect of axial strain on solvatochromic shift for a 1.5% DCM doped Alq_3: DCM thin film. (a) False color SEM micrograph of SiO_2 microbeams (length 15 µm) released using XeF_2 gas phase etching following thermal evaporation. (b) Normalized PL intensity profile at three different positions on the beam. The normalized PL intensity at position P (maximum strain) shows a clear blueshift with respect to normalized intensity at positions M and N (zero strain). (c) Axial tensile strain along the released SiO_2 microbeams with the zero strain positions (M & N) and maximum strain position highlighted (P). (d) Peak emission wavelength of DCM and fractional change in orientational polarizability along the microbeam extracted from photoluminescence measurements.

From the measured peak PL emission, one can extract the local orientational polarization (Δf) along the strained thin films for different DCM doping concentrations. We rewrite Equation 3.1 as:

$$\upsilon_a - \upsilon_f = m\Delta f + C \quad \text{(Equation 3.2)}$$

where,

$$m = \frac{2}{hc}\frac{(\mu_E - \mu_G)^2}{a^3} \quad \text{(Equation 3.3)}$$

$$\Delta f = \frac{\varepsilon - 1}{2\varepsilon + 1} - \frac{n^2 - 1}{2n^2 + 1} \quad \text{(Equation 3.4)}$$

We use the reported values of m and C of 7.94×10^3 cm^{-1} and 2.74×10^3 cm^{-1} respectively [212], [216] and the DCM absorption peak wavelength of 480 nm [217] to extract the orientational polarizability based on the measured PL emission peaks. We assume a negligible change in the absorption spectrum of DCM due to axial tension on the thin film. The solvatochromic shift due to molecular reorientation takes place over a long time scale (~10^{-9} s) compared to light absorption(~10^{-15} s), justifying the assumption [211]. The spatial variation of the change in orientational polarizability along the 1.5% doped DCM doped thin film is plotted in Figure 3-3(d) (right y-axis). The orientational polarizability decreases gradually from the zero-strain position and reaches its minimum value at the maximum tensile strain position on the microbeam. Based on the results, ~9% change in the orientational polarization was estimated under axial tension of 0.9%. The spatial variation of the orientational polarizability for a 2.5 % and 5 % DCM doped strained thin film has also been estimated from PL measurements [173].

From our measurement, we observe a linear relationship between the peak DCM emission energy and the axial tensile strain for different DCM doping concentrations as shown in Figure 3-4. However, the rate of a solvatochromic shift under strain was different at different DCM doping

concentrations. We observed the highest slope of 0.016 eV/% in the 1.5 % doped film, reduced to 0.006 eV/% for 5% doped film.

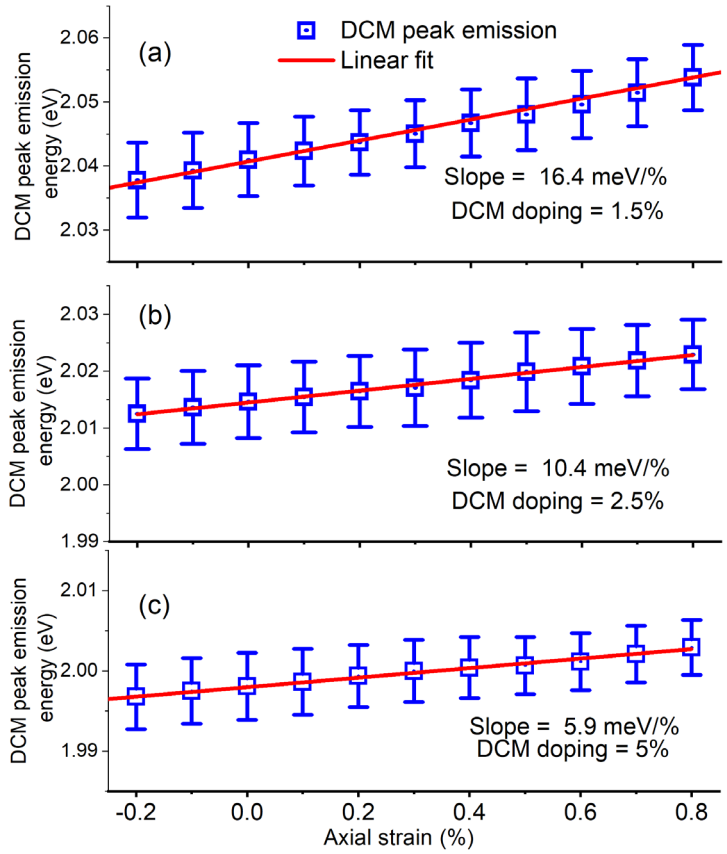

Figure 3-4: Linear fit of DCM peak emission energy with axial strain at for different DCM doping. (a) 1.5%; (b) 2.5%; (c) 5% DCM doping concentrations. Even though DCM peak emission energy shift consistently follows a linear relationship with axial strain, the range of peak emission energy modulation under strain decreases with DCM doping. The error bar in the figures represents the range of DCM peak emission energies from different samples.

To understand the relationship of DCM peak emission energy to external axial strain, we use the Clausius- Mossoti relation that relates the dielectric response of a homogeneous medium, $\frac{\varepsilon-1}{\varepsilon+2}$ with molecular polarizability, α as [218]:

$$\frac{\varepsilon-1}{\varepsilon+2}=\frac{n\alpha}{3\varepsilon_0} \quad \text{(Equation 3.5)}$$

Here, n refers to the molecular density of the medium (N/V where we assume the number of molecules dispersed in volume V is N), and ε_0 refers to the free space dielectric constant. Since the high-frequency refractive index is not affected by axial tension on the thin film, any effect on the dielectric polarizability under external strain must be due to changes in the dielectric function,

$$\Delta f(\varepsilon)=\frac{\varepsilon-1}{2\varepsilon+1} \quad \text{(Equation 3.6)}$$

Under strain, the thin film undergoes local volumetric change (Δv) that modulates the molecular density at a specific doping level. We estimate the volumetric change under axial tension by considering a small volumetric segment of the thin film as shown in Figure 3-5(a). The length, width, and height of the segment are presented as X, Y, and Z. The out-of-plane deflection of the microbeams elongates the thin film uniaxially (along the x-direction in Figure 3-5(a)) and therefore, due to the Poisson effect, the thin film is compressed along y and z directions. We represent the elongation of the thin film along the microbeam axis as Δx and the orthogonal compression as Δy and Δz. Defining the Poisson ratio of the thin film as ν, the orthogonal compressions can be written as $\Delta y=-\nu Y\varepsilon_x$ and $\Delta z=-\nu Z\varepsilon_x$.

Therefore, under uniaxial strain, the volumetric change in the thin film (Δv) due to small axial elongation under strain, can be related to the initial volume, V as [219]:

$$V+\Delta v=XYZ(1+\varepsilon_x)(1-\nu\varepsilon_x)^2$$
$$\Rightarrow 1+\frac{\Delta v}{V}=(1+\varepsilon_x)(1-2\nu\varepsilon_x)+\nu^2\varepsilon_x^2(1+\varepsilon_x)$$

$$\Rightarrow \frac{\Delta v}{V} = (1 - 2\nu)\varepsilon_x$$

In the first order, the dielectric polarizability under tensile strain $\Delta f(\varepsilon)$ is related to the volumetric change by the following linear relationship:

$$\Delta f(\varepsilon) \approx \frac{N\alpha}{3\varepsilon_0(V+\Delta v)} \approx \frac{N\alpha}{3\varepsilon_0 V(1+\frac{\Delta v}{V})} \approx \frac{N\alpha}{3\varepsilon_0 V}(1 - \frac{\Delta v}{V}) \approx M(1 - (1 - 2\nu)\varepsilon_x) \quad \text{(Equation 3.7)}$$

where *M* is a proportionality constant. Therefore, for a specific DCM doping, under small volumetric deformation, the local dielectric property in the thin film is linearly proportional to the axial strain. This leads to a linear shift in solvatochromic energy in the DCM emission under mechanical strain. From the observed peak DCM emission energy under strain, we estimated the orientational polarization of the host: guest medium at different guest molecule doping concentrations that shows a linear relationship with the applied tensile strain [173].

3.5 Strain tuned solid-state solvation at different DCM doping

From our steady-state PL measurement on different DCM doped strained thin films, we can estimate the strain sensitivity of DCM peak emission energy in the Alq_3 background matrix. We define the DCM strain sensitivity as $E_{peak}(\varepsilon) - E_{peak}(0)$, where $E_{peak}(\varepsilon)$ and $E_{peak}(0)$ refer to DCM peak emission energy in strained and unstrained thin films respectively. The observed modulation of DCM peak emission energy is a direct consequence of strain-modulated dielectric polarization in the thin film and hence corresponds to the sensitivity of dielectric polarizability to external strain. Figure 3-5(b) shows the estimated strain sensitivity of DCM peak emission shift in Alq_3: DCM thin films at different DCM doping concentrations. As the DCM doping increases, orientational polarizability and the resulting solvatochromic shift in the thin film become less sensitive to the external uniaxial strain and so does the observed spectral shift.

The observed trend in strain sensitivity of orientational polarization for different doping concentrations can be explained by the physical origin of the solvatochromic shift in the host: guest Alq_3: DCM system. At very low concentrations, the emission properties of organic fluorophores are strongly affected by the electric field from surrounding fluorophores in a host: guest medium [220]. The increase in DCM doping reduces the intermolecular separation between DCM dipoles and enhances the dielectric polarization and the net local field on a molecular dipole. This leads to an increase in the energy required for molecular orientation after photoexcitation and a stronger stabilization of the excited state. In our experiment, the mechanical properties of the system are dominated by the host Alq_3 matrix. Therefore, under uniaxial tensile strain, the intermolecular distance between neighboring DCM molecules dispersed in the Alq_3 matrix increases. Besides, as the thin film is uniaxially elongated, compression due to the Poisson effect also reduces intermolecular distance orthogonal to the elongation axis. These two mechanisms result in a net molecular density and net dielectric polarizability in the medium that governs the energy shift due to solvatochromism. At a low DCM doping level, due to low molecular density and large intermolecular distance, uniaxial elongation of the thin film leads to a reduction in net molecular density and reduces the net local electric field on a molecular dipole. Therefore, we observe a larger modulation of the orientational polarizability under strain at lower DCM doping concentration. However, as the DCM doping increases, due to reduced intermolecular separation, orthogonal compression of the thin film due to the Poisson effect reduces the net change in orientational polarization due to elongation under axial tensile strain. To further support this argument, we performed PL measurements on 5% DCM doped compressively strained organic thin films and observed a similar trend in the orientational polarizability and peak DCM emission to compressive strain [173]. Since we observe similar modulation in orientational polarizability

and emission energy under both uniaxial compressive and tensile strain for a 5% DCM doped thin film, we conclude that the orientational polarizability (and in turn dielectric polarizability) of the medium under external strain indeed becomes less sensitive as the guest molecular doping increases. Our observation of solvatochromic shift under strain, therefore, reveals the critical role of molecular doping in the modulation of dielectric polarizability of host: guest medium under external mechanics.

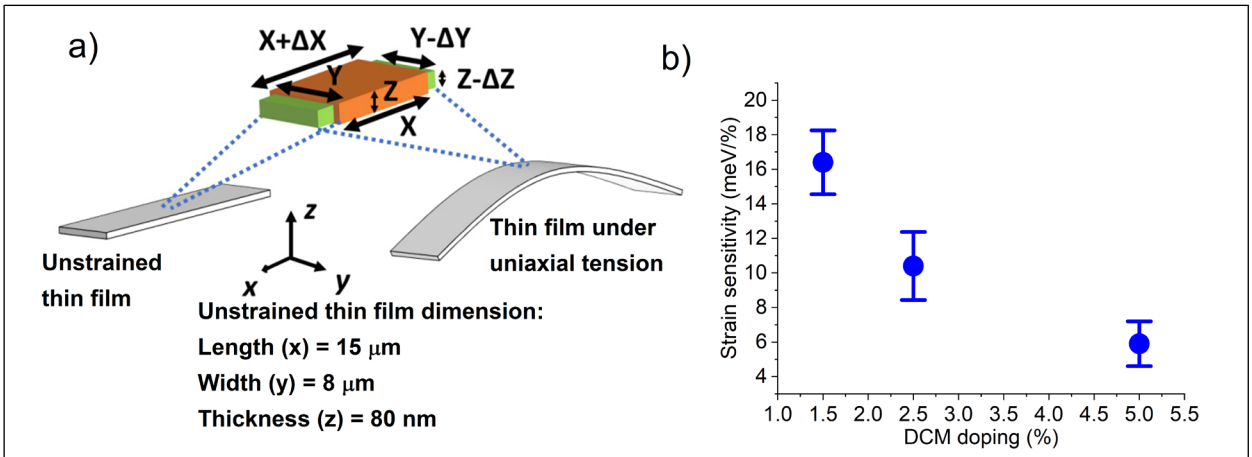

Figure 3-5: (a) Simple schematic representation of an organic thin film under axial tensile strain. While the dimensions of the unstrained thin film are mentioned in the figure, the figure is not drawn to scale. (b) Strain sensitivity of the orientational polarization in Alq_3: DCM host: guest medium at different DCM doping. The error bars represent the range of strain sensitivity extracted from PL measurements on microbeams at different DCM doping.

3.6 Dynamically tuned solid-state solvation using MEMs actuator

Since the axial strain generated on the self-strained silicon oxide microbeams changes gradually along the beam axis, such microbeam-generated strain may or may not accurately portray the dynamic behavior of a strained organic thin film. To address this, we fabricated MEMS thin film membrane devices on low-stress Si_3N_4/Si substrate that utilizes electrostatic actuation of a proof mass structure to dynamically strain an organic thin film evaporated on top of the devices. We numerically modeled the dynamic actuation behavior of the MEMS thin film membrane device structure under applied electrostatic force using COMSOL Multiphysics [221] and extracted the device dimensions for fabrication [172]. The fabrication process of the MEMS thin film devices has been discussed in Appendix B.

Figure 3-6 (a) shows the SEM micrograph of a representative MEMS membrane device fabricated on low-stress Si_3N_4. A higher magnification SEM micrograph of the area of the device structure where axial tensile strain is generated is also shown. As the proof mass structure deflects downward due to electrostatic actuation, tensile strain is generated along the microbeams AA′ and BB′. Under electrostatic actuation, each of the microbeams AA′ and BB′ acts as a cantilever beam under point load applied at the free end. For a cantilever beam under point load, the maximum axial tensile strain is generated at the fixed end [219]. The fixed end position of beam AA′ is marked as F. To determine the position of maximum tensile strain along the beam (the fixed end position of the microbeam), we performed PL scan at 1 μm steps along the microbeam under applied electrical bias of 0 V to 150 V and extracted the DCM emission energy from the centroid of the measured PL spectra. From the evolution of DCM emission energy with applied bias voltage, measured at different positions along the microbeam, we estimated the position of the maximum tensile strain. The results of PL measurements at different positions along the

microbeam are discussed in Datta et al. [172]. Figure 3-6(b) shows a schematic drawing of the MEMS thin film device structure (not drawn to scale). The electrostatic actuation of the proof mass generates axial strain (ε) along the support beam (beam AA′ in Figure 3-6(a)) with the maximum strain generated at the fixed end position (position F in Figure 3-6(a)).

Figure 3-6(c) shows the centroid of the measured PL spectra (1.5 % DCM doped thin film) at the position of the maximum tensile strain on the microbeam at different applied voltages along with the axial tensile strain simulated using COMSOL Multiphysics [221]. As the axial tensile strain increases with applied voltage, the PL centroid shows a gradual blueshift due to a reduction in local molecular density. The fitting of DCM emission energy from the measurements with simulated axial tensile strain is shown in Figure 3-6(d). Figure 3-6(e) shows the normalized PL intensity at the position of maximum tensile strain under two different applied voltages – 0V and 150V. The normalized PL intensity at 150 V applied voltage shows a clear blue shift due to the tensile train.

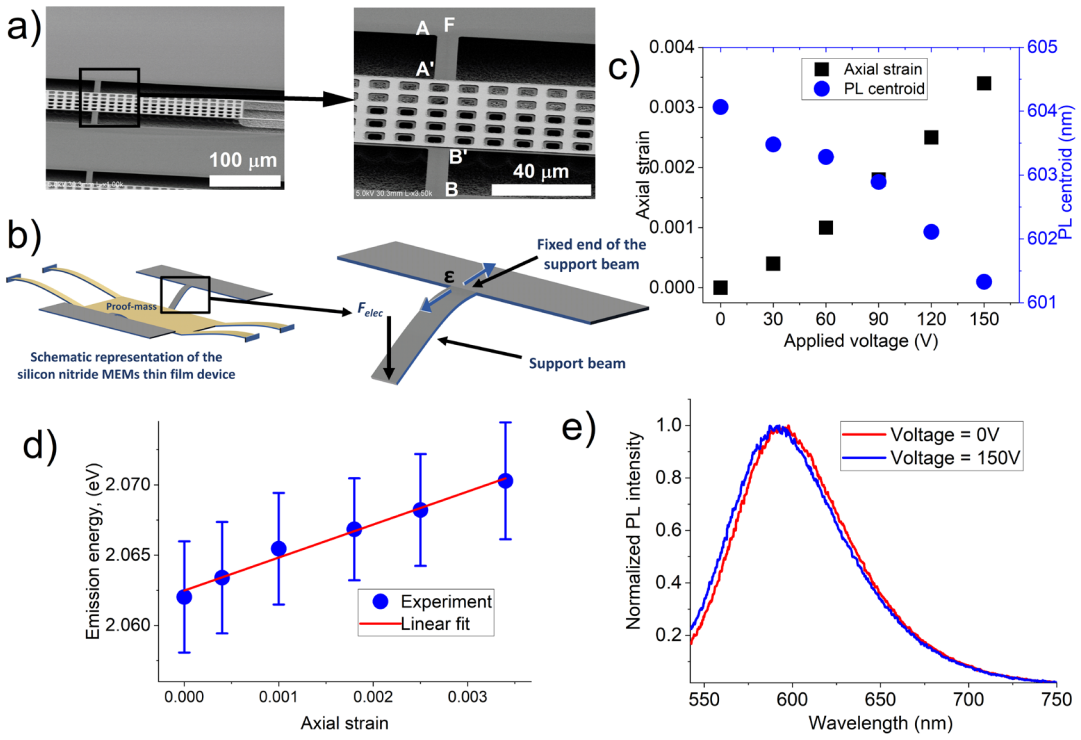

Figure 3-6: Dynamic strain on organic thin film using a MEMS thin film membrane actuator: (a) SEM micrograph of a representative MEMS membrane device used in this work. The higher magnification figure shows microbeams AA′ and BB′ along which axial tensile strain is generated under applied voltage. The fixed end position of microbeam AA′ is marked by F. (b) Schematic drawing of the MEMS device (not drawn to scale) under electrostatic actuation showing the position of axial strain (ε) generation. (c) Axial tensile strain at the fixed end positions from COMSOL simulation and measured PL centroid under applied voltage. The PL centroid shows a gradual blue-shift under applied voltage due to increasing axial tensile strain. (d) Fitting of DCM emission energy under applied voltage with simulated tensile strain at maximum strain position with error bar. Here error bar represents the range of DCM emission energy from PL measurement at maximum strain position. (e) Normalized PL intensity profile at the measurement position in (c) at two different applied bias voltages: 0V and 150V that shows a blueshift under applied voltage due to tensile strain.

3.7 A possible non-destructive approach toward the estimation of Young's modulus

Since external strain(pressure) reduces(increases) the volumetric molecular density of a guest: host medium and therefore the dielectric susceptibility, for small deformation, the polarizability of the background matrix has been shown to be linearly proportional to applied mechanical strain. Therefore, for a homogeneous guest: host medium under compression, the measured spectral shift, ΔE_{PL} under axial tension, ε can be written as:

$$\Delta E_{PL} = A\alpha P = A\alpha Y\epsilon \qquad \text{(Equation 3.8)}$$

Here, *P* refers to the applied pressure on the organic guest: host medium under study. α is the proportionality constant that relates the volumetric change in molecular density to applied uniaxial pressure. For a host: guest system, the parameter is found to be dependent on the host molecules. It depends on the Poisson's ratio and elastic modulus of the thin film material and has been extracted from the solvatochromic shift of organic guest: host thin film under pressure [14]. The value of parameter A depends on the organic molecule under study and has been reported to have similar values for similar molecules in different dielectric environments [22]. Under small deformation, the applied pressure, P can be related to axial strain by $P=Y\varepsilon$, where Y refers to the Young's modulus of the thin film. Therefore, by measuring the photoluminescence from a dopant molecule embedded in a background matrix under external pressure and strain, one can estimate the Youngs modulus using Equation 3.8. In our work, we have estimated the Young's modulus of the background Alq_3 matrix using the photoluminescence shift from the dopant DCM molecules. From our measured photoluminescence shift under axial strain, we extract the Young's modulus to be 2.81±1.28 GPa. The value of Young's modulus extracted using the solvatochromic shift appears to be slightly higher than those reported using buckling method for Alq_3 thin film [187]

although they are of the same order of magnitude. The estimated values are also in the same order of magnitude as other amorphous organic materials [183],[222]. However, the reported values are much smaller than the one reported using nano-indentation that overestimates the elastic modulus due to substrate-indenter interaction [188]. Such a non-invasive approach based on local electric field properties of molecular thin films is extremely beneficial for on-chip determination of elastic properties and could be extended for extraction of other relevant mechanical properties.

3.8 Comment on solid state solvation and possible alteration of the molecular morphology under strain

The observed blue shift in DCM emission energy with axial tensile strain along the SiO_2 buckled microbeams and its dependence on the DCM doping strongly suggests that axial strain triggered the solvatochromic shift in the doped guest: host thin film. However, previously observed photoluminescence spectral shift under external pressure in small molecule thin film [24] and conjugate organic polymers [15], [104] suggests that such spectral modification could also be triggered by a change in the morphology, and structure of the guest molecule under study [24], [25], [102]. To note, the hydrostatic pressure required to induce spectral modification due to possible deformation in molecular morphology has been reported to be more than 10 kbar or 1 GPa [15], [27]. However, from our estimated axial strain on the thin film, using Young's modulus [187], we estimate the maximum applied pressure range on the Alq_3: DCM to be 0.02 GPa, which is two orders of magnitude lower than the ones reported in the literature [15], [24], [104]. We also note that, under a possible pressure-induced morphological modification of the DCM molecule, the spectral shift under similar axial strain range, from thin films at different DCM doing, is expected to be similar, which is not observed in our PL measurements. These results, therefore, strongly suggests that the observed spectral shift in our work is primarily triggered by a strain

induced change in molecular density that results in a decrease in background polarizability as axial strain on the thin film is increased.

3.9 Summary

Using self-strained -SiO_2 microbeams to apply controlled axial tensile strain on an organic host: guest medium, we show precise modulation of the solvatochromic spectral shift in a molecular doped host: guest medium at different guest doping concentrations. Our measurements show that the spectral shift due to solvation at different doping concentrations of the guest molecule follows a linear relationship with applied strain. From the solvatochromic spectral shift, using Lippert- Mataga equation we show that the dielectric polarizability of the host: guest medium shows greater sensitivity at low guest molecule doping. As the dielectric nature of the medium is externally increased by guest molecular doping, short-range intermolecular interactions strongly dominate the solvation properties in the medium and the dielectric properties of the medium become less sensitive to external mechanical stimuli. The reported results can greatly aid in the design of wearable and large-scale flexible optoelectronic devices based on excitonic modulation under external mechanical stimuli. Moreover, the use of self-strained SiO_2 microbeams and MEMS thin film devices fabricated on the Si_3N_4 platform enable a non-contact and hence non-destructive method to measure the mechanical properties of organic thin films by changing the local dielectric properties. The microstructures allow the application of controlled tensile strain on the overlying thermally evaporated organic guest: host thin film. Using solvatochromic spectral shift, we have successfully extracted Young's modulus of the organic thin film to be within 2.81-3.88 GPa. Such strain-based optical non-contact method can be used for accurately measuring the elastic modulus of organic semiconductor thin films for flexible and wearable nanoscale devices for optoelectronic and photovoltaic applications. The method described in this work can be

extremely useful for on-chip characterization of elastic properties of small molecule organic semiconductor thin films and can be extended for estimating other relevant nanoscale mechanical properties as well as precise and dynamic tuning of nanoscale exciton energy transfer in organic thin film devices.

Chapter 4 Exciton Photoluminescence Modulation under Strong Piezoelectric Screening in Monolayer Semiconductors

4.1 Authorship and copyright disclaimer statement

The contents of this chapter were published in ACS Nano in June 2021 [223]. I retain the rights to include the results and contents of the publications in this dissertation provided that it's not used commercially. The other co-authors were Zidong Li, Zhengyang Lyu, Parag B Deotare from the University of Michigan, Ann Arbor, Michigan, USA.

4.2 Background

In recent years, semiconducting transition metal dichalcogenide (TMD) monolayers have garnered widespread interest and persistent investigation from research communities across the world [224], [225]. The optical properties of these materials are dominated by excitons: coulomb-bound electron-hole pairs that are known for very large oscillator strength [226]. The strong quantum confinement and reduced dielectric screening results in large excitonic binding energy [227]–[229] that enables manipulation of the excitonic response even at room temperature using an external electric field or strain. Surface acoustic waves (SAW) on a piezoelectric substrate provide a universal platform to simultaneously study the effect of both manipulation approaches. While SAW devices have been widely used in wireless RF communication, they have been

profoundly influential in advancing fundamental research. For instance, SAW has been used as an effective tool for spatial and temporal manipulation of excitonic properties [50], [51] in embedded semiconducting nanostructures such as quantum well [230], [231], quantum wire [232], [233] quantum dot [234], [235] and more recently monolayer two-dimensional materials such as MoS_2 [236], [237] and hexagonal boron nitride (h-BN) [238]. Surface acoustic wave has also been used to realize high-performing optoelectronic devices that operate on the principles of piezoelectric dissociation [239], [240] and to study charge transport in low-dimensional materials [241]–[245]. More importantly, SAW devices can generate a large in-plane piezoelectric field, which aligns with the large polarizability in TMDs [246]–[248] compared to a few orders of magnitude lower out-of-plane polarizability [249]–[251].

In this section, we discuss the interaction of excitons in monolayer WSe_2 with SAW generated using Lithium Niobate ($LiNbO_3$) as the piezoelectric material at room temperature. The interaction of SAW with excitons in semiconducting nanostructures strongly depends on the type of band edge modulation in the semiconducting medium. In type-I band edge modulation, the spatial modulation of the conduction and valence bands with opposite phases creates periodic spatiotemporal traps [52] that act as an efficient conveyor for excitons [53]. On the other hand, in type-II modulation, strong built-in electric fields generated by the same spatial phase modulation of conduction and valence bands result in exciton dissociation into electron-hole pairs trapped at the piezoelectric potential pockets [252]. Under the latter scheme, the dissociated charges may be transferred and later recombined at a remote location as the electric field due to SAW is screened/removed by external means [252]. In our experiment, we observed the dominance of type-II modulation using high-frequency Rayleigh SAW waves [253] that were generated on a 128^0 Y-cut $LiNbO_3$ substrate using interdigitated transducers (IDTs, period (λ_{SAW}) of 6 μm). The

finger width of the IDTs was kept at half the IDT period and the acoustic aperture (the IDT finger overlap length) was > 30λ (acoustic measurements of the SAW transducers are shown in Figure 4-1(a)). Mechanically exfoliated WSe_2 monolayer was transferred on the delay line of the SAW device. We observed that the high dielectric constant of the piezoelectric substrate contributed to the increased dielectric screening [39], [254]–[256] of the coulomb interaction between bound electron-hole pairs in the monolayer reducing the exciton binding energy. Probing the monolayer photoluminescence (PL), we observed dissociation of excitons and trions under RF excitation along with a gradual shift of the overall distribution towards trion. The dissociation was accompanied by a strong Stark shift of the PL spectrum by the in-plane electric field of the SAW and PL linewidth broadening due to exciton ionization under the piezoelectric field. The observed dissociation, spectral shift, and broadening of the PL were strongly dependent on the optically generated free carrier screening in the monolayer. Based on the results, we estimated the in-plane polarizability of neutral excitons to be $8.43 \pm 0.18 \times 10^{-6}$ Dm/V, which agrees well with the theoretically predicted and experimentally reported values [247], [257]. Such controlled manipulation of different excitonic species under external stimulus in a dielectrically screened environment can prove useful for next-generation excitonic devices serving applications from sensing, and detection to on-chip communication, as well as integration of TMDs to substrates beyond silicon.

4.3 Dissociation of exciton and trion in monolayer WSe_2 under strong piezoelectric screening

A brightfield image of a mechanically exfoliated monolayer WSe_2 transferred along the SAW delay line is shown in Figure 4-2(a), where the arrow marks the propagation direction of the acoustic wave. Under increased RF input power, the native band structure of the material is

modified by the SAW's piezoelectric field (type-II band edge modulation dominates due to the proximity of the monolayer to the piezoelectric material) resulting in potential pockets, which are spatially separated by half of the acoustic wavelength ($\lambda_{SAW}/2$) [252]. A simple schematic representation of such modulation is depicted in Figure 4-2(b). The strong piezoelectric field dissociates the optically generated excitons and confines the electrons and holes in the lateral potential pockets (conduction band minima ($E_{cmin,\ SAW}$) and valence band maxima ($E_{vmax,\ SAW}$)). Figure 4-2(c) shows the PL intensity (at 6μW optical power) and centroid maps of the monolayer at RF input power levels of -60 dBm (the minimum RF power used in this work) and 20 dBm. The observed uniform spatial quenching of the integrated PL intensity with SAW confirms type – II band edge modulation by the traveling piezoelectric field as reported previously in III-V semiconducting nanowires [233]. The PL quenching is accompanied by a redshift of the monolayer's PL centroid as evident from the centroid histogram for various RF input power as shown in Figure 4-2(d). The redshift is attributed to the stark shift by the in-plane component (in the direction of propagation) of the propagating electric field of the SAW [248] which is discussed later.

The effect of SAW piezoelectric potential on the dissociation of trions and excitons can be analyzed separately by extracting the integrated intensity of trions ($\int_\lambda I_{PL,tr}(\lambda)d\lambda$) and excitons ($\int_\lambda I_{PL,ex}(\lambda)d\lambda$) at different RF input power levels as shown in Figure 4-3(a) and Figure 4-3(b) respectively. Here, $I_{PL,ex}(\lambda), I_{PL,tr}(\lambda)$ refer to the estimated PL spectrum for the excitons and trions. These are extracted by fitting the spectra using two Gaussian functions corresponding to neutral A-excitons and trions respectively [258]–[263] (We show two Gaussian fitting of a representative PL spectrum at 0.5 μW optical power at -60 dBm RF excitation in Figure 4-4(a). The neutral A- exciton and trion Gaussian peaks are located at ~1.664 eV and ~1.638 eV

respectively. Consistent with the dissociation model due to the piezoelectric field, we observe a gradual reduction in the neutral and charged exciton PL with the increase in the RF power. The corresponding PL spectra can be found in the supporting information section 6 of Datta et al. [223]. For a given RF level, the dissociation is reduced for higher optical incident powers [223]. This is because the SAW piezoelectric field is screened by the optically generated free carriers, thereby reducing the effective electric field that contributes to PL quenching. As a result, a higher electric field is required to achieve the same level of PL quenching. We observed no spectral shift or broadening in the monolayer PL for a range of optical incident power between 0.5 μW to 6 μW at very low RF input power levels of -60 dBm [223]. Hence, we rule out the contributions from optically induced heating and/or, possible scattering with free carriers at higher excitation power. In addition, the integrated PL intensity of the exciton and trion peaks showed no signature of excitation-dependent nonlinearity [223], [264]. Further analyses are thereby limited to the linear response regime.

We investigated the effect on the steady-state equilibrium between the excitonic species in the monolayer by extracting the spectral weight of trion, $\eta_{PL,tr} = \frac{\int_\lambda I_{PL,tr}(\lambda)d\lambda}{\int_\lambda I_{PL}(\lambda)d\lambda}$ and exciton, $\eta_{PL,ex} = \frac{\int_\lambda I_{PL,ex}(\lambda)d\lambda}{\int_\lambda I_{PL}(\lambda)d\lambda}$; where $\int_\lambda I_{PL}(\lambda)d\lambda = \int_\lambda I_{PL,ex}(\lambda)d\lambda + \int_\lambda I_{PL,tr}(\lambda)d\lambda$. We observe a gradual evolution of the spectral weight towards trions with an increase in the RF input power as shown in Figure 4-3(c). The results indicate that the ionization rate for excitons is larger than that of trions [223]. Furthermore, we found no variation in the spectral weight with respect to optical excitation power at RF input power levels of -60 dBm [223]. Hence, we conclude that the observed spectral weight shift in the PL is triggered by the exciton dissociation due to the in-plane electric field component of the traveling SAW field. This results in an increase in the trion formation rate as more free carriers become available due to the piezoelectric dissociation [265], [266]. The conclusion is

further supported by the observed increase in the trion binding energy at high RF power, which is strongly correlated to the free carrier density in the system [223], [267], [268].

We also compare the observed PL quenching in our work with exciton dissociation in other low-dimensional excitonic media like GaAs [252], [269] and ZnCdSe [270] quantum wells. Even though almost complete quenching of photoluminescence under the piezoelectric field has been reported in these works, we do not observe such strong dissociation within our experimental range. This is explained by large exciton binding energy in monolayer semiconductors. This observation also aligns with recent theoretical work by Huang et al.[271] where exciton ionization under electric field in monolayer semiconductors was shown to be significantly weaker than in GaAs system.

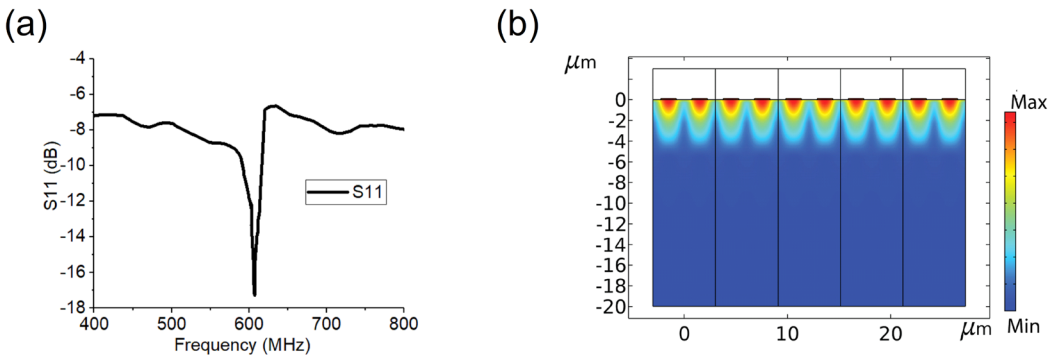

Figure 4-1: (a) Reflection co-efficient(S11) of the SAW transducer that shows a sharp resonance at ~610 MHz. (b) Simulated surface displacement profile of the SAW transducer resonance frequency using COMSOL Multiphysics.

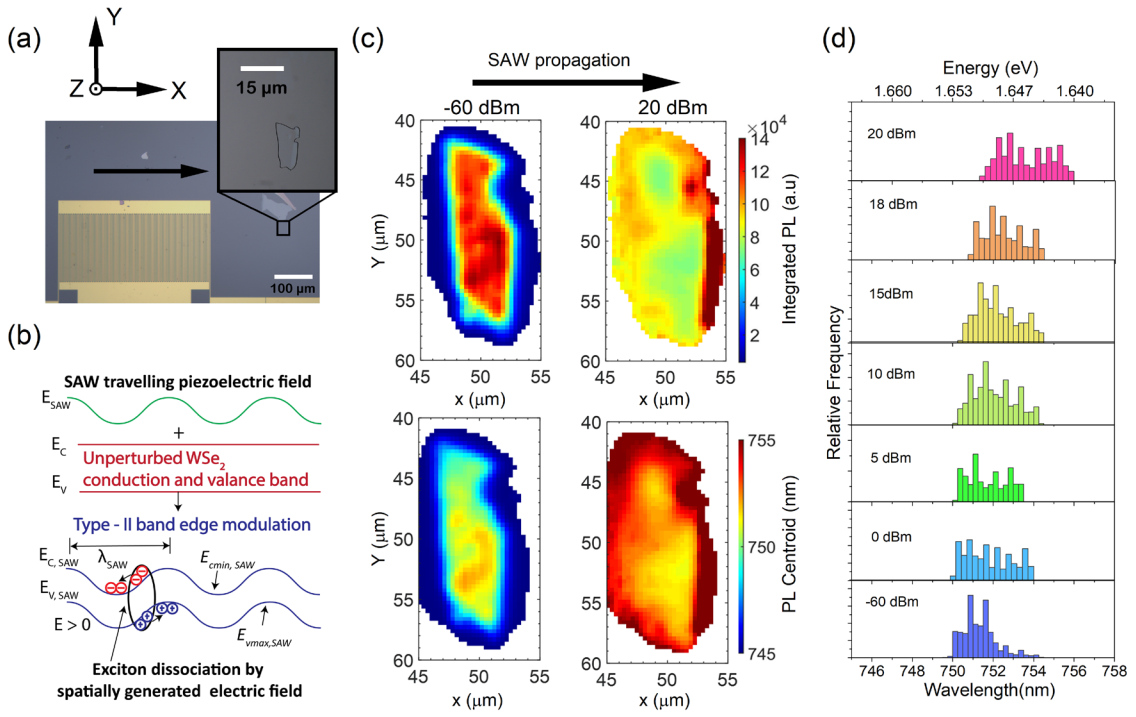

Figure 4-2: Exciton dissociation under surface acoustic wave in monolayer WSe_2. (a) Transferred monolayer WSe_2 (marked by black lines) on the delay line of the SAW device. The arrow in the figure shows the propagation direction of the acoustic wave. (b) A schematic representation of SAW induced exciton dissociation by type – II band edge modulation. Dissociated electrons and holes are accumulated at the conduction band minima ($E_{cmin,\ SAW}$) and valence band maxima ($E_{vmax,\ SAW}$) respectively. (c) Integrated PL intensity and PL centroid map of the monolayer WSe_2 at -60 dBm and 20 dBm RF input power levels (6 μW optical excitation power). The SAW propagation direction is shown by the arrow on top. Strong PL quenching is observed as the SAW power is increased due to dissociation of excitons and trions into free carriers by the in-plane electric field. The centroid map shows stark effect induced redshift under SAW excitation. (d) Histogram of the PL centroid extracted from the PL map in (c). The centroid distribution in the histogram shows a gradual redshift as the RF input power is increased.

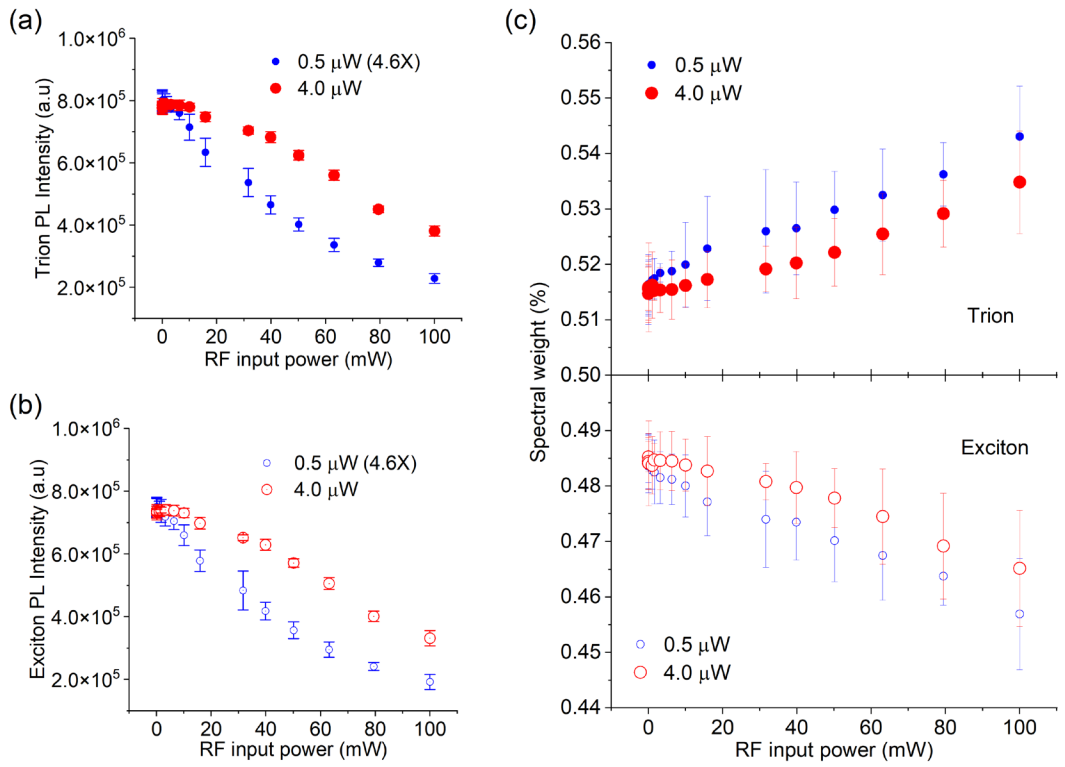

Figure 4-3: Effect of SAW on (a) trion and (b) exciton PL intensity with RF power at different optical excitations. To improve clarity of presentation, the exciton and trion PL intensities at 0.5 μW have been multiplied by a factor of 4.6. Accumulation of dissociated free carriers results in screening that leads to a decrease in the steady state exciton and trion dissociation. The screening effect increases with optical excitation power. (c) Change in the exciton and trion spectral weight by the SAW electric field. An increase in the trion spectral weight and decrease in exciton spectral weight is observed with increased RF excitation input. The total range of spectral weight change varies with optical excitation, which confirm screened piezoelectric field in the monolayer at high optical excitations.

4.4 Stark shift in monolayer semiconductor under piezoelectric field

As mentioned earlier, alongside dissociation, the piezoelectric field also triggers PL Stark shift. The spectral redshift of the excitonic energy level due to the electric field of a SAW has been reported for low dimensional quantum well structures [272]–[274]. The excitonic spectral redshift (ΔE) is generally represented by:

$$\Delta E = -\frac{1}{2}\alpha {E_X}^2 \qquad \text{(Equation 4.1)}$$

where α and E_X refer to the in-plane neutral exciton polarizability and the applied electric field respectively. The net spectral redshift of the neutral exciton due to the piezoelectric field varied with optical incident power [223]. Figure 4-4(a) shows two Gaussian fitting of monolayer PL spectra at 0.5 μW optical input power under -60 dBm acoustic excitation. Figure 4-4(b) and Figure 4-4(c) show the redshift of the neutral exciton with the estimated electric field at 0.5μW and 4 μW optical incident power respectively. The electric field is estimated from the observed PL quenching as described in [223]. The error bar represents the spread from PL measurements at four locations on the monolayer. We extract the exciton polarizability by fitting the spectral redshift of the exciton peak with the estimated electric field using Equation 4.1. Based on the experiments at different optical excitation power [223], we estimate the neutral exciton polarizability in the monolayer to be $8.43 \pm 0.18 \times 10^{-6}$ Dm/V. We attribute the observed spectral shift to the in-plane electric field of the SAW since the out-of-plane polarizability of monolayer excitons is smaller by a few orders of magnitude [249], [250]. The estimated in-plane polarizability is about an order higher than the reported values in a lower dielectric constant environment (h-BN) [248] and SiO_2 [275]. The observed large in-plane polarizability in this work is due to the strong screening effect from the $LiNbO_3$ substrate that weakens the interaction between the bound electron and hole,

thereby causing the excitonic state to be more susceptible to the applied electric field. This leads to a larger spectral shift in the monolayer PL. In general, it is difficult to verify such an effect due to challenges in fabricating device structures that can apply the in-plane electric field. However, the transfer of monolayer TMD on a piezoelectric substrate such as used in this work offers a simple platform to probe spectral change due to an in-plane electric field. We note that the observed spectral redshift cannot be accounted for due to heating by the surface acoustic wave [223]. In addition, as discussed in the earlier section, we rule out any possible heating due to optical excitation.

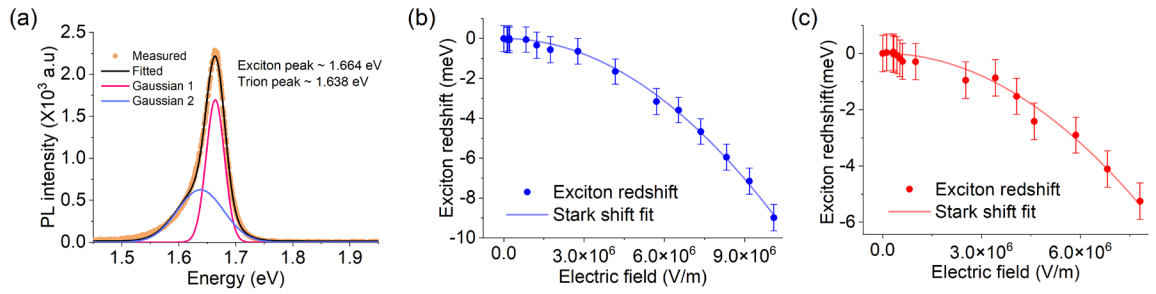

Figure 4-4: Spectral modulation of monolayer WSe_2 excitons under SAW electric field. (a) Two gaussian fit of measured monolayer PL spectra at 0.5 µW optical input power and -60 dBm input RF excitation. Fit to the excitonic redshift at (b) 0.5 µW average optical power using the quadratic stark shift equation that yield the in-plane neutral exciton polarizability of 8.36×10^{-6} Dm/V and (c) 4 µW average optical power that yields a neutral exciton polarizability of 8.49×10^{-6} Dm/V. The error bar in (b) and (c) corresponds to the spread of PL measurements at different location on the monolayer sample. The quadrature dependence of the exciton spectral shift with the screened electric field confirms that the observed spectral shift is induced by the piezoelectric SAW field.

4.5 Exciton photoluminescence broadening under acoustic modulation

In low dimensional semiconductor systems, the broadening of PL can be attributed to various physical mechanisms such as elastic and inelastic scattering with free carriers, phonons, exciton ionization under applied electric field, and dynamic modulation of the bandgap through lattice deformation due to strain [50]. We observe no broadening of the PL spectra with optical input power [223], and hence we rule out broadening due to lattice heating under optical excitation. Alongside, we rule out substrate heating as the dominant mechanism for spectral modulation [223]. Linewidth broadening due to exciton-free carrier scattering takes place at high excitation densities $>10^{12}$ cm^{-2} [276], which is one-two orders of magnitude higher than the excitation density used in the current experiments. Hence, we assume a negligible contribution from scattering with free carriers. Therefore, we attribute the linewidth broadening of the exciton PL to dynamic strain [52] (type-I modulation) in the monolayer and piezoelectric field-induced ionization (type-II modulation).

We estimate the effect of dynamic strain on the exciton spectral linewidth by calculating the strain tensor,

$$\varepsilon_k = \sum_{i=1}^{3} d_{ik} E_i \qquad \text{(Equation 4.2)}$$

where d is the matrix for the converse piezoelectric effect in the material (128^0 $LiNbO_3$ for this work) and E is the piezoelectric field. Based on the strain tensor, we estimate a maximum volumetric strain of ~0.05% at maximum RF input power of 100 mW using the estimated piezoelectric field in the substrate at acoustic resonance. Finally, we use the strain sensitivity (58 meV/%) of the bandgap of monolayer WSe_2 reported in the literature [122], [277] and estimate the broadening (Γ_ε) due to dynamic strain by the formulation presented in Weiβ *et al.* [50].

We estimate the linewidth broadening due to piezoelectric field (Γ_{ion}) by following a two-dimensional exciton ionization model [278]. However, to account for strong screening from the surrounding dielectric environment, we use a scaled version of the relationship:

$$\Gamma_{ion}(E) = \beta E_b \sqrt{\frac{\gamma F_0}{F}} exp\left(-\frac{32}{3}\frac{\gamma F_0}{F}\right) \quad \text{(Equation 4.3)}$$

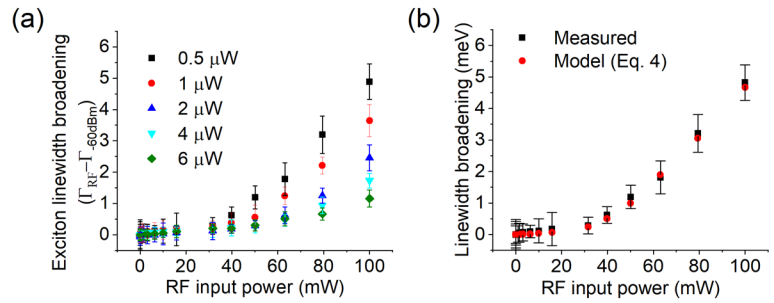

Figure 4-5: Exciton linewidth modulation by piezoelectric interaction in monolayer WSe_2. (a) Extracted linewidth broadening of the exciton peak from PL spectra at different RF input power. A clear dependence on the free carrier screening process can be observed from the figure. We observe the maximum broadening at the minimum optical power input. (b) Linewidth broadening fitted as a combined effect of dynamic strain and field induced ionization (as shown in Equation 4.4). The black squares in the figure represent the median of our extracted broadening from PL measurement. The error bar in both the plots represents the spread of PL measurements at different positions on the sample.

where β and γ are dimensionless parameters that account for substrate-induced dielectric screening that modifies the Coulomb interaction in the monolayer. A smaller value of the scaling factor (γ <1) refers to a stronger screening and hence, a larger linewidth broadening change under electric field and vice versa. F_0 represents the field required for exciton ionization under substrate-induced screening: $F_0 = \frac{E_b^*}{e a_b^*}$; where, E_b^* and a_b^* are the screened exction binding energy and Bohr radius respectively and e is the electronic charge. The total linewidth broadening under RF excitation can now be written as:

$$\Gamma_{RF} - \Gamma_{-60dBm} = \Gamma_{ion}(E) + \Gamma_{\varepsilon}$$

$$= \beta E_b \sqrt{\frac{\gamma F_0}{F}} exp\left(-\frac{32}{3}\frac{\gamma F_0}{F}\right) + \Gamma_{\varepsilon} \qquad \text{(Equation 4.4)}$$

As seen from Figure 4-5(a), the neutral exciton peak broadens with RF power, but the broadening effect decreases with an increase in optical power. The results imply that the PL linewidth broadening is primarily affected by exciton dissociation.

Figure 4-5(b) shows the measured linewidth broadening of the neutral exciton peak and the fitted broadening using Equation 4.4 for 0.5 μW optical input power. We obtain best fit for β = 9.054± 1.491 and γ = 0.245± 0.009. Contrary to the electric field dependence derived from the simple Hydrogen atom model (γ =1) [278], our experimentally measured broadening of the neutral exciton state shows a stronger dependence on the SAW electric field, - a clear signature of substrate-induced screening of Coulomb interaction. The strong substrate screening is also observed from the linewidth broadening at different optical input power [223]. Therefore, we conclude that the observed broadening in the excitonic linewidth has contributions from both, the

piezoelectric field (*i.e.*, exciton ionization by the electric field), and dynamic modulation of the monolayer bandgap by the acoustic strain field. The contribution due to the field-induced ionization is significantly larger than the strain-induced broadening.

4.6 Acoustically modulated exciton time-resolved photoluminescence under strong piezoelectric screening

To obtain more insight into the piezoelectric dissociation of excitons under RF excitation, we have performed transient photoluminescence (TRPL) using 405 nm pulsed excitation source. In the absence of piezoelectric dissociation, the TRPL from WSe_2 monolayer can be fitted with two exponential functions:

$$I(t) = A\,exp(-k_f t) + B\,exp(-k_s t) \quad \text{(Equation 4.5)}$$

where the fast (k_f) component is attributed to the decay (radiative and nonradiative) from the excitonic state and slow (k_s) component is typically attributed to the emission from defect-bound states [279]–[282]. For TRPL under RF excitation, we define, an effective decay rate, k_{eff} that is written as:

$$k_{eff} = k_{decay,-60dBm} + k_{ion,piezoelectric} \quad \text{(Equation 4.6)}$$

where, $k_{decay,-60dBm} = \frac{1}{\tau_{decay,-60dBm}}$ refers to the decay rate of the excitons due to radiative and non-radiative processes (without any RF excitation, *i.e.* at -60 dBm), $k_{ion,piezoelectric}$ refers to the ionization of photogenerated excitons by the SAW piezoelectric field [283].

A representative biexponential fit under no RF excitation is shown in Figure 4-6(a). Using $k_{eff} = k_f$, we extracted the ionization rate of excitons at various RF power. Using Equation 4.6 the ionization rate, therefore, can be written as:

$$k_{ion,piezoelectric} = k_{eff} - k_{decay,-60dBm} \quad \text{(Equation 4.7)}$$

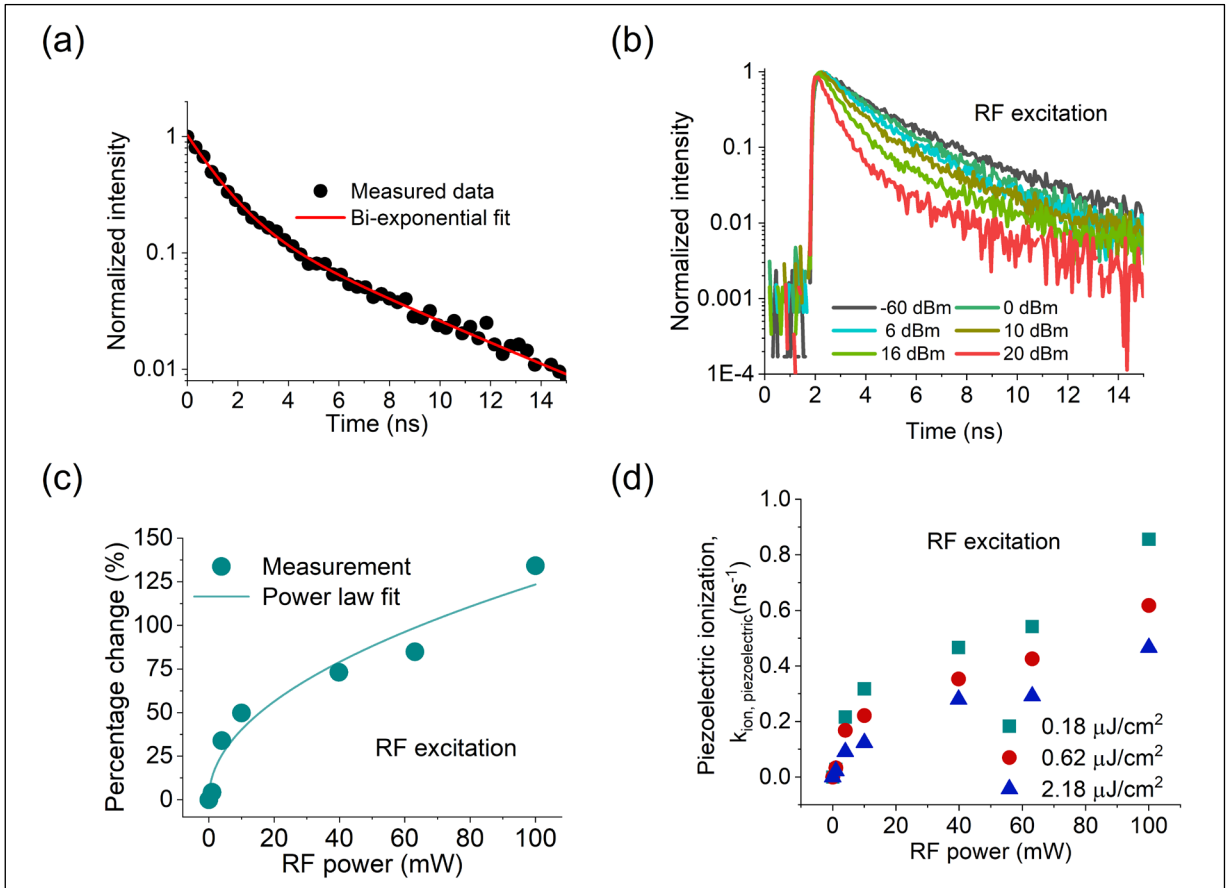

Figure 4-6: Time resolved photoluminescence (TRPL) measurement under RF excitation. (a) Bi-exponential fit of the TRPL measured from our work at 0.18 μJ/cm^2 under -60 dBm RF excitation. (b) Normalized TRPL measurements from monolayer WSe_2 showing dependence on RF excitation at 0.18 μJ/cm^2. (c) Percentage change in the exciton decay under RF excitation within our experimental range for 0.18 μJ/cm^2 excitation fluence. Our experiment reveals that the decay rate increases by > 140%. The increase in decay rate can be fitted using a power law ($\propto$ (RF power)$^{\beta}$); $\beta = 0.49 \pm 0.08$, confirming that the decay rate shows a linear dependence with the SAW electric field. (d) Estimated exciton ionization rate, that shows an increase with RF power. The ionization rate also shows an inverse relationship with optical fluence due to optically generated free carrier screening process.

Figure 4-6(b) shows monolayer TRPL Figure 4-6(c) shows the percentage change in the decay rate under RF excitation at 0.18 μJ/cm^2 excitation fluence. We observe that at 100 mW RF power, k_{eff} changes from $\sim 0.64\ ns^{-1}$ to ~ $\sim 1.49\ ns^{-1}$, an increase of >140 %. Figure 4-6 (d) shows the ionization rate for various RF excitations at three different optical pump fluences: 0.18 μJ/cm^2, 0.62 μJ/cm^2 and 2.18 μJ/cm^2. In all the cases, we see an increase in the ionization rate of the TRPL signal intensity under RF excitation. At a constant optical fluence, the effective decay rate k_{eff} increases with RF excitation due to increased piezoelectric dissociation of photogenerated excitons. In addition, the observed ionization rate shows an inverse dependence with optical fluence due to the optically generated free carrier screening process. This agrees with the steady-state PL quenching observed at different optical input powers.

4.7 Summary

In conclusion, we have experimentally investigated the interaction of excitons in monolayer WSe_2 with the piezoelectric field of a surface acoustic wave. The strong dielectric screening from the $LiNbO_3$ substrate weakens the Coulomb interaction between the electron and hole of the bound excitonic state, thereby increasing the neutral exciton polarizability. Under RF input excitation, the photogenerated excitonic species are readily dissociated *via* field-induced ionization. We show that the spectral modulation of the monolayer PL can be controlled by the optically generated free carrier screening. The study, therefore, demonstrates two simultaneous yet independent approaches to control excitonic properties in TMDs. Such control using artificially engineered environmental screening can prove to be extremely beneficial for the realization of next-generation high-speed optoelectronic devices that require rapid and strong dissociation of photogenerated excitonic species.

Chapter 5 Room Temperature Exciton Transport Under Traveling Strain in Monolayer Semiconductors

5.1 Authorship and copyright disclaimer statement

The contents of this chapter were published in Nature Photonics in March 2022 [171]. I retain the rights to include the results and contents of the publications in this dissertation provided that it's not used commercially. The other co-authors were Zhengyang Lyu, Zidong Li, Parag B Deotare from the University of Michigan, Ann Arbor, Michigan, USA, Takashi Taniguchi from the International Center for Materials Nanoarchitectonics, National Institute for Materials Science, Tsukuba, Japan, Kenji Watanabe from Research Center for Functional Materials, National Institute for Materials Science, Tsukuba, Japan.

5.2 Background

Coulombically bound electron-hole pair commonly known as an exciton provide an effective platform to transport energy at the nanoscale. The small dimension and seamless transition with a photon make excitons an ideal candidate for applications in energy conversion [58], light emission [284], chemical sensing [285], and information processing and communication [286], [287]. Such applications can significantly benefit under controlled spatial manipulation of exciton fluxes, especially at room temperature. With the recent emergence of 2D semiconductors such as transition metal dichalcogenides (TMDs) that support excitons with high diffusivity and

binding energy (>100 meV) [224], [227], the feasibility of room temperature excitonic devices is no longer questionable [288]. Unlike charged particles that drift under an externally applied electric field, directed transport of charge-neutral exciton flux is achieved by spatial tuning of exciton potential by external stimuli such as mechanical strain [48], [94] or electric field [163], [289]–[292]. Traveling surface acoustic waves (SAWs) can utilize both effects dynamically to achieve long-range transport. While most of the reported SAW-assisted transport is based on transporting the individual charges following exciton dissociation by the piezoelectric field, exciton transport under dynamic strain from SAWs has also been achieved in III-V quantum well systems [52]–[54]. However, it is limited to cryogenic temperatures and utilizes indirect excitons that are created using an external electrical field. With large sensitivity of the bandgap to external strain [11], [43], TMDs are well suited to achieve room temperature, and directional transport of direct excitons, solely under dynamic strain. In monolayer materials, SAWs have been successfully utilized for long-range carrier transport [241], [242], improved photoconductivity [293], and modulation of phonons [294] and excitonic photoluminescence [223], [237]. In this work, we study spatiotemporal control of exciton flux in a monolayer tungsten diselenide (WSe_2) system at room temperature. High frequency (~745 MHz resonance frequency) Rayleigh type SAWs are generated in a piezoelectric 128^0 Y-cut lithium niobate substrate ($LiNbO_3$) using interdigitated electrodes (IDTs). For a detailed fabrication process of SAW filters on piezoelectric $LiNbO_3$, please refer to Appendix C. Mechanically exfoliated monolayer WSe_2 encapsulated in hexagonal boron nitride (h-BN) was transferred on the SAW delay line using a dry transfer technique. Using phase-synchronized spatiotemporal measurements and utilizing photogenerated free carriers to screen the in-plane electric field, we report directed exciton transport under type-I bandgap modulation.

5.3 Sample description and room temperature photoluminescence characterization

Figure 5-1(a) shows a schematic of the device geometry used in this work. Figure 5-1(b) and (c) show a false-color brightfield optical image of the sample and the photoluminescence (PL) map of the h-BN encapsulated monolayer WSe_2. The h-BN encapsulation is critical to improving the transport properties of the excitons by suppressing non-radiative recombination processes [295], surface roughness [98], energetic disorder [97], and scattering from impurities and surface states [296]. More importantly, the underlying bulk h-BN moderates the dielectric environment surrounding the monolayer thereby increasing the exciton binding energy when compared to the monolayer directly placed on $LiNbO_3$ substrate. This reduces exciton dissociation under SAW piezoelectric field (type-II modulation) due to increased binding energy [223], [255]. The dissociation can be further reduced by screening the piezoelectric field, thereby enabling the study of excitonic interactions with type-I modulation (bandgap change due to strain). In this work, we achieve it by utilizing the optically generated free carriers to screen the in-plane electric field of the traveling SAW wave. Figure 5-1(d) plots the PL quenching ($r_Q = \frac{I_{PL,RF}}{I_{PL,-60dBm}}$) due to dissociation as a function of RF input power for various optical excitations. Here, $I_{PL,RF} = \int I_{RF}(\lambda)\, d\lambda$ and $I_{PL,-60dBm} = \int I_{-60dBm}(\lambda)\, d\lambda$ refer to integrated PL intensity measured at a given RF input power and at -60 dBm (1 nW, the minimum RF input power used in this work), respectively. The net quenching at a given RF power, reduces with increase in optical excitation density due to optically generated free carrier screening [223], [269]. Thus, the excitation optical fluence provides a knob to control the dissociation and thereby investigate effects of type-I modulation on exciton transport.

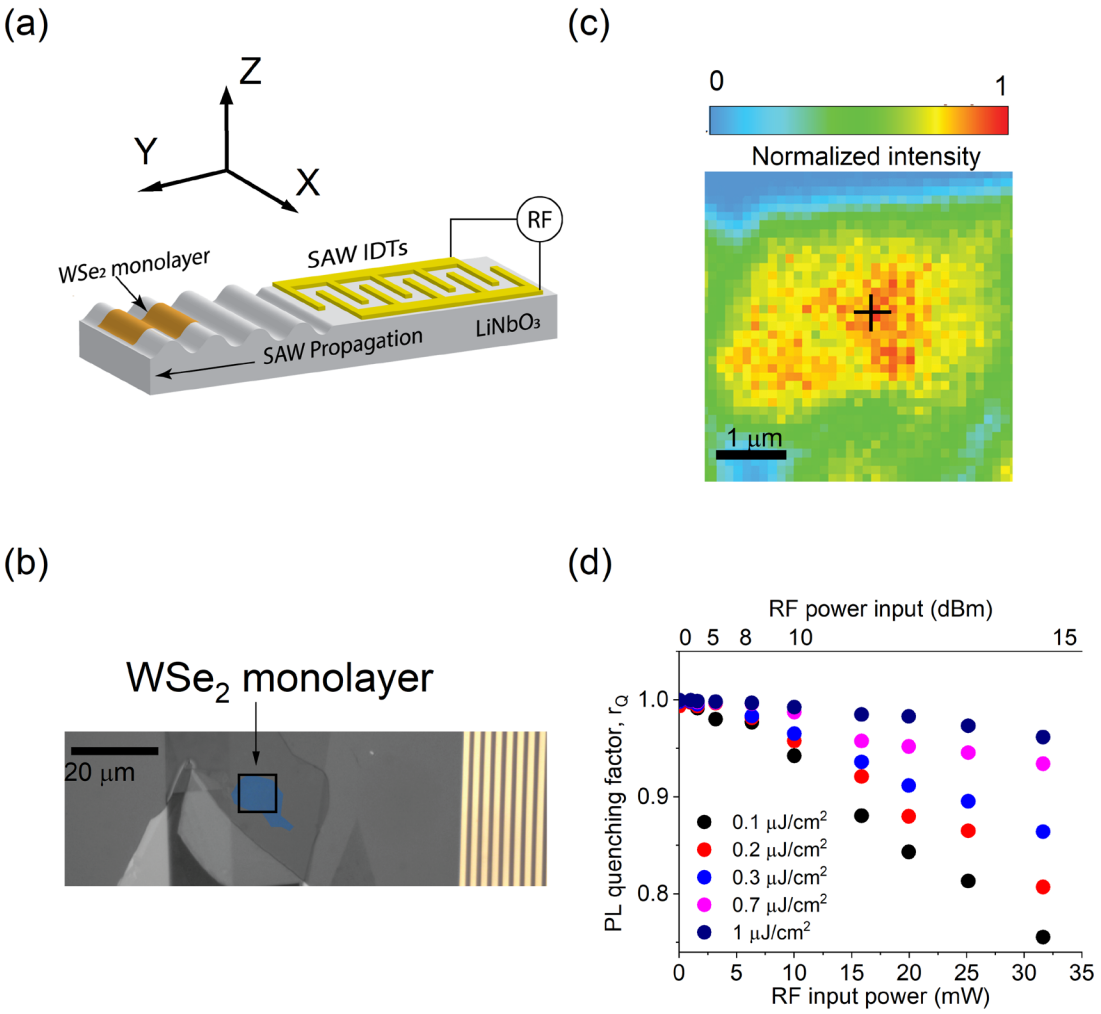

Figure 5-1: Modulation of h-BN encapsulated monolayer WSe_2 photoluminescence (PL) by traveling piezoelectric field of the surface acoustic wave. (a) A schematic representation of the transferred monolayer WSe_2 on the SAW delay line. (b) Brightfield optical image of a h-BN encapsulated monolayer WSe_2 transferred on lithium niobate substrate. (c) Integrated PL intensity map of monolayer area represented by the square in (b). (d) PL intensity modulation under increased RF power at various optical excitation densities. The monolayer PL emission decreases with increase in RF power. The net PL quenching, however, reduces with increasing optical power density due to screening from optically generated free carriers.

5.4 Exciton transport under dynamic strain wave

Figure 5-2 shows the results of excitonic energy transport measured using a scanning SPAD technique described in our previous work [94]. A detailed diagram of the experimental setup can be found in Appendix D. Figure 5-2(a) and (b) show the spatiotemporal exciton density distributions at -60 dBm (~1 nW) and 13 dBm (~20 mW) RF input power respectively at an optical fluence of 1.2 $\mu J/cm^2$ (type-I modulation dominates since PL quenching was under ~2 % under the experimental conditions). Figure 5-2(c) and (d) show the exciton density distribution normalized along space at each time instance from Figure 5-2(a) and (b), respectively. The symmetric exciton density distribution at -60dBm resembles typical anomalous exciton diffusion in monolayer WSe_2 [94], [171]. In this case, the peak position of the distribution does not show any spatial drift with time, indicating the absence of a local strain gradient in the monolayer. When the RF excitation is turned ON, the exciton density distribution shifts along the propagation direction of the SAW. Exciton density distribution at two-time instances t =0 ns and t =3.5 ns along with the Gaussian fits are shown in Figure 5-2(e) and Figure 5-2(f) for -60 dBm and 13 dBm RF excitation respectively. The black arrow indicates the direction of SAW propagation.

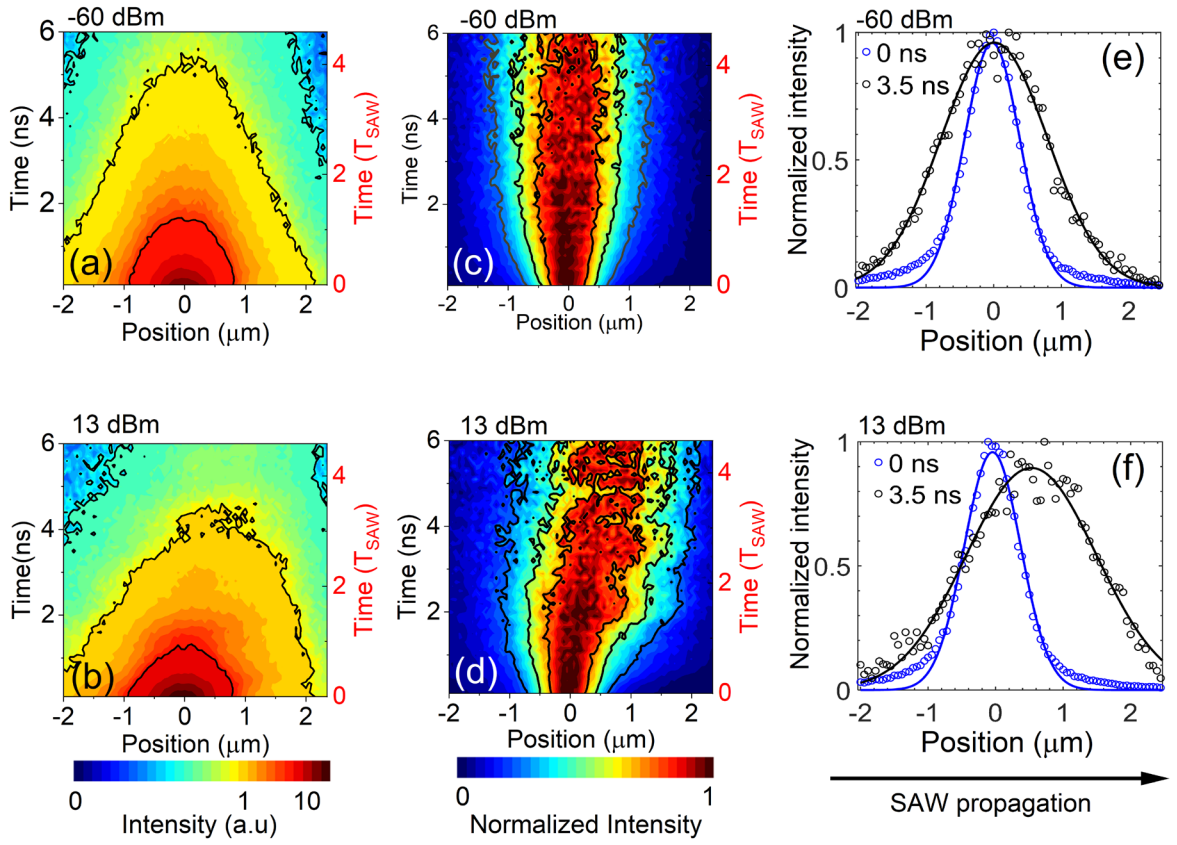

Figure 5-2: Spatiotemporal exciton density profile (log scale) from phase synchronized TCSPC measurement for (a) – 60 dBm; (b) 13 dBm RF excitation input. Spatiotemporal map of exciton density (normalized for each time instance along space) for (c) -60 dBm and (d) 13 dBm RF input power at optical fluence of 1.2 μJ/cm^2. A spatial shift in exciton density can be observed under RF excitation. Normalized exciton density profiles at different time instances as a function of space along with the Gaussian fit under (e) -60 dBm and (f) 13 dBm RF input power. At minimum RF input power (-60 dBm), the exciton density broadens symmetrically in space due to exciton diffusion in the monolayer. At high RF input, an asymmetric spatial shift of the exciton density in the direction of the acoustic wave propagation is observed with the observed shift increasing with time. To improve the signal to noise ratio, the raw data was binned using a 100 ps window.

Figure 5-3 (a) shows the spatial evolution of the gaussian exciton density peak as a function of time. With increasing RF power, we see a gradual increase in the spatial shift. In addition, we observe periodic oscillations corresponding to the SAW period. This suggests a weak coupling regime between the excitons and the traveling strain wave (discussed in the following section), where the exciton drift velocity is insufficient to keep up with the traveling wave and hence, results in a net spatial shift over time of the exciton density. We model the evolution of the gaussian peak under dynamic strain over time using a linear relationship (solid line in Figure 5-3(a)):

$$h(t) = v_{avg}t + h_{offset} \quad \text{(Equation 5.1)}$$

where $h(t)$ refers to the net displacement of the generated exciton density over many SAW periods, v_{avg} refers to the average drift velocity of the exciton density under applied dynamic strain, and h_{offset} is a constant to accommodate the fitting error. Figure 5-3(b) plots the v_{avg} for various volumetric strain estimated at different RF input power. A linear trend with volumetric strain indicates a proportional increase in exciton coupling efficiency with the dynamic strain field. Further improvement in v_{avg} can be achieved by increasing the strain gradient or increasing exciton diffusivity by suppressing scattering from impurity states and surface roughness [296].

We determine the extent of exciton coupling to the dynamically varying strain field of the SAW by estimating the instantaneous velocity from the measured instantaneous displacement of the exciton density. The time derivative of the measured displacement at 13 dBm RF input power gives the instantaneous velocity of the exciton flux as shown in Figure 5-3(c). The instantaneous drift velocity reaches a maximum value of 600 m/s, which is smaller than the SAW velocity (v_{saw}) in $LiNbO_3$ (3979 m/s [166]). Since the maximum drift velocity of the exciton flux is nearly six times smaller than the acoustic wave velocity ($v_{max,13\ dBm} < v_{saw}$), the exciton flux cannot keep pace

with the traveling strain wave (weak coupling regime). This results in asymmetric exciton funneling (in opposite directions) during each SAW period. Hence, we observe oscillations in the peak position of the exciton distribution and a net spatial shift over time in the direction of the traveling strain field as seen in Figure 5-2(d) and Figure 5-3(a). The observation closely resembles carrier drift under a dynamic electric field in the weak coupling regime presented in García-Cristóbal et al. [283]. Under strong coupling, the excitons would funnel to the lowest potential, followed by transport of the trapped excitons with the strain wave. In such a case, the transport distance is expected to be limited by the radiative lifetime and sample size. Such a regime of exciton transport has been observed in III-V semiconducting quantum wells at cryogenic temperatures [52], [53].

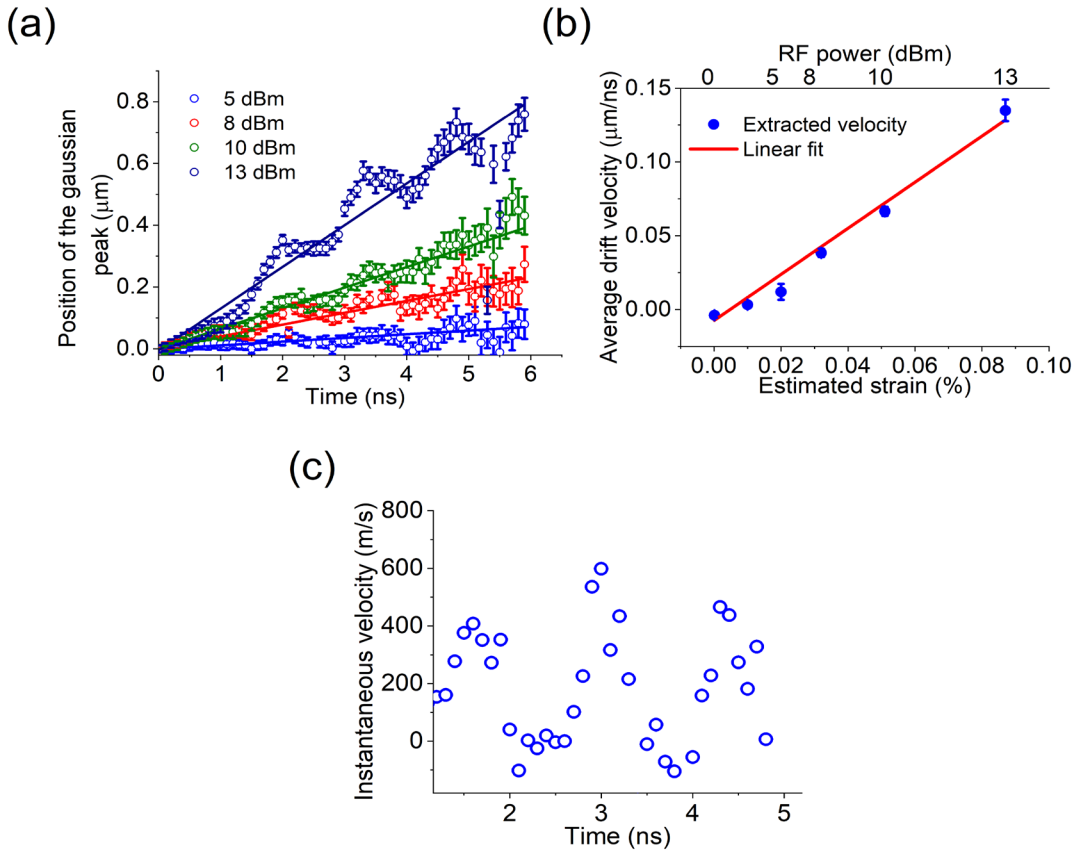

Figure 5-3: Exciton transport in monolayer WSe_2 under incremental RF power at 1.2 μJ/cm^2 optical fluence. (a) Spatiotemporal evolution of the exciton density peak extracted using gaussian fits (circles) and the approximate linear fit (solid lines) at various acoustic power. The error bars represent the uncertainties in the gaussian fit. (b) Effective shift in the position of the gaussian peak extracted from the model introduced in the text that shows an increase in transport length as RF input power is increased. The maximum shift of the Gaussian peak increases with applied RF input power, clear signature of long-range energy transport under dynamic strain in the monolayer. (c) The time derivative of the 13 dBm data in (a). The instantaneous velocity of the exciton flux reaches 600 m/s but is still lower than the acoustic wave velocity (3979 m/s). To improve the signal to noise ratio, the raw data was binned using a 100 ps window.

Under a dynamically varying strain field, the maximum exciton drift velocity can be written as:

$$v_{max} = \mu \left|\frac{\partial E_g}{\partial \varepsilon}\right| \frac{\partial \varepsilon}{\partial x}|_{max}$$

$$= \mu \left|\frac{\partial E_g}{\partial \varepsilon}\right| k\varepsilon_0 \qquad \text{(Equation 5.2)}$$

where μ, $\frac{\partial E_g}{\partial \varepsilon}$, $k = \frac{2\pi}{\lambda_{SAW}}$, and ε_0 refer to the exciton mobility, strain sensitivity of monolayer bandgap [122], acoustic wave momentum, and maximum dynamic strain in the monolayer, respectively. λ_{SAW} refers to the wavelength of the acoustic wave ($\lambda_{SAW} = 4.7\ \mu m$). Based on the measured PL quenching (Figure 5-1(d)), we calculate the maximum dynamic strain amplitude (ε_0) to be ~ +0.086 % (tension) at 13 dBm RF power using the converse piezoelectric matrix [297] of 128^0 $LiNbO_3$ and the estimated piezoelectric field in the substrate [171]. Using the estimated value of maximum drift velocity at 13 dBm RF input power (600 m/s, about 15% of the SAW velocity) in Equation 5.2, we extract the exciton mobility in the monolayer to be 900 $cm^2/eV/s$. The extracted exciton mobility is nearly two orders lower (exceeding 10^4 $cm^2/eV/s$ [52], [170], [298]) compared to indirect excitons in III-V quantum well structures at cryogenic temperatures that show long-range transport [52], [53]. The small exciton mobility, resulting from scattering with defects and phonons at room temperature, along with short radiative lifetime results in a smaller transport distance (~μm) under dynamic strain in monolayer TMDs. However, the results show the potential of the material system for future room-temperature excitonic devices, especially as defect densities get lowered with rapid progress in material growth.

We note that the total bandgap modulation ($\delta E_g = 2 * 0.086 * 60 = 10.3\ meV$) is smaller than the room-temperature thermal energy (25.7 meV). However, the observed directional

transport primarily results from the combination of the strong bandgap sensitivity of TMD monolayers, and the strain gradient generated by the SAW wave, which leads to drift dominating over diffusion transport at room temperature [171]. At the same time, we assume negligible decoupling of the dynamic strain to the WSe_2 monolayer through the underlying h-BN flakes due to the high mechanical strength [299] and small thickness (20-30 nm; measured using white light interferometry) compared to the acoustic wavelength (4.7 μm) [53], [54]. Therefore, the extracted values of average drift velocity set the lower limit at room temperature. We also expect negligible contributions to the observed transport from strain-induced binding energy change of neutral excitons as such modulations are significantly smaller compared to strain-induced bandgap modulation based on theoretical calculations [69], [125], [300]. Finally, we expect a negligible contribution to the quasiparticle conversion (exciton to trion) under strain [47], [301] and type-II bandgap modulation [223] due to much lower strain amplitude (<0.1%) and screening due to the underlying h-BN spacer.

Exciton transport under type-I modulation takes place by spatial trapping at the minimum energy locations [167] (please refer Figure 5-4(a)-(d) for a schematic representation of the exciton potential under a dynamic strain field. We verified that the observed spatiotemporal modulation in the exciton density is due to type-I modulation by performing three experiments. First, we conduct transport measurements at an order of lower optical fluence. Since the effective mobility of the photogenerated excitons increases with optical fluence [302], the excitons experience efficient coupling with the traveling strain field at high optical excitation densities. For the same set of RF powers (constant strain), we observed reduced modulation in the exciton density and a decrease in average exciton spatial drift for lower optical fluence (as discussed in a later section). Second, we measured time-dependent photoluminescence (TRPL) as a function of optical fluence. At low

fluence, the TRPL decays faster with an increase in RF power due to increased ionization [223], [278] (additional decay) resulting from type-II modulation. At high fluence, the reduction in TRPL decay rate is slower [171], confirming the screening of the in-plane piezoelectric field by the free carriers. Under this condition, type-I modulation dominates and the TRPL oscillates at the SAW frequency. The strain-induced oscillations result from the dynamic modulation of the energy separation between K and Q valleys under the traveling strain wave [171]. We also note that the observations have been reproduced on multiple samples with different RF resonance frequencies [171].

5.5 Acoustic steering of photogenerated excitons

The dynamic acoustic strain field generated by a SAW wave can be represented by:

$$\varepsilon(x,t) = \varepsilon_0 \, cos(\, \omega t - kx + \varphi) \qquad \text{(Equation 5.3)}$$

where, ε_0 refers to the amplitude of the strain field, ω refers to the angular frequency ($\omega = 2\pi f_{SAW}$; f_{SAW}refers to the acoustic resonance frequency), and φ refers to the instantaneous phase of the acoustic wave. Therefore, for a given optical excitation position from the IDT, the generated exciton density interacts with a certain phase of the traveling strain field. Using Equation 5.3, the dynamic strain-induced drift velocity of the exciton flux can be written as [94]:

$$v_{ex}(x,t) = \mu_\varepsilon \frac{\partial \varepsilon(x,t)}{\partial x} = \mu_\varepsilon k \, sin(\, \omega t - kx + \varphi) \qquad \text{(Equation 5.4)}$$

where $\mu_\varepsilon = \mu \frac{\partial E_g}{\partial \varepsilon}$ refers to the strain mobility of the excitons [94]. At photoexcitation (t=0), the instantaneous velocity of the exciton flux is a function of the acoustic phase, $v_{ex}(x,0) = \mu_\varepsilon k \, sin(\, - kx + \varphi)$. Therefore, precise control over the direction of photogenerated exciton flux can be achieved by controlling the relative phases as shown in Figure 5-4(a) – (d). We achieve such control by introducing a delay, τ ($\varphi = \frac{2\pi}{T}\tau; T = \frac{1}{f_{SAW}}$) in the laser trigger signal (refer Appendix D for schematics of the characterization setup). Figure 5-4(e) plots the spatiotemporal evolution of the center of the exciton density distribution as a function of the time delay (τ) with increments of T/4, which were further numerically modeled using the following modified drift-diffusion equation [94]:

$$\frac{\partial n_{ex}(x,t)}{\partial t} = D_{ex}\frac{\partial^2 n_{ex}(x,t)}{\partial x^2} + \frac{\partial (v_{ex} n_{ex}(x,t))}{\partial x} + G - \frac{n_{ex}(x,t)}{\tau_{ex}} - \frac{n_{ex}(x,t)}{\tau_{ion}} \quad \text{(Equation 5.5)}$$

$$v_{ex} = \mu_{\varepsilon}\frac{\partial \varepsilon(x,t)}{\partial x} \quad \text{(Equation 5.6)}$$

$$\frac{1}{\tau_{ion}} = \frac{\varepsilon_{2D}}{\hbar}\frac{8}{\sqrt{2\pi}}\sqrt{\frac{E_{ion}}{|E|}}\, exp(-\frac{4}{3}\frac{E_{ion}}{|E|}) \quad \text{(Equation 5.7)}$$

$$E_{ion} = \frac{\varepsilon_{2D}}{a_{2D}} \quad \text{(Equation 5.8)}$$

Here, D_{ex} refers to diffusion co-efficient of neutral excitons, respectively. μ_{ex} refers to the mobility of electron/hole/ neutral excitons respectively, $E(x,t)$ and $\varepsilon(x,t)$ refer to SAW piezoelectric field and dynamic strain field, respectively. *G* refers to the photogenerated exciton density under optical excitation. τ_{ex} refers to the radiative recombination lifetime of neutral excitons. μ_{ε} refers to the strain mobility of neutral excitons in the monolayer. τ_{ion} refers to the ionization time of the photogenerated neutral exciton [283] which effectively introduces an additional decay channel for the excitons. E_{ion} refers to the electric field required for ionization [278], [283] of excitonic species in the monolayer. ε_{2D} and a_{2D} refer to the exciton binding energy and the Bohr radius in the monolayer WSe_2 [171].The photogenerated exciton density, G was estimated to be $2.4\text{x}10^{11}/\text{cm}^2$ [171], assuming 10% absorbance for monolayer WSe_2 [303]. For simulation, we used the time-dependent exciton diffusivity under no RF [171]. The parameters used for simulation are shown in Table 5-1.

Table 5-1: Parameters used for simulating the exciton density modulation under dynamic strain

Parameter	Value
Exciton drift mobility	65 $cm^2/\%/s$
Exciton radiative lifetime, τ_{ex}	0.7 ns (Refer [171])
Electric field, E	5 $x10^6$ V/m (Refer [171])

The solid lines in Figure 5-4(e) are fits from the numerical simulation that successfully captures the observed dynamics at different SAW phases [171] under the same RF excitation power. Consistently, we observed similar progressive evolution with the instantaneous phase in the TRPL [171].

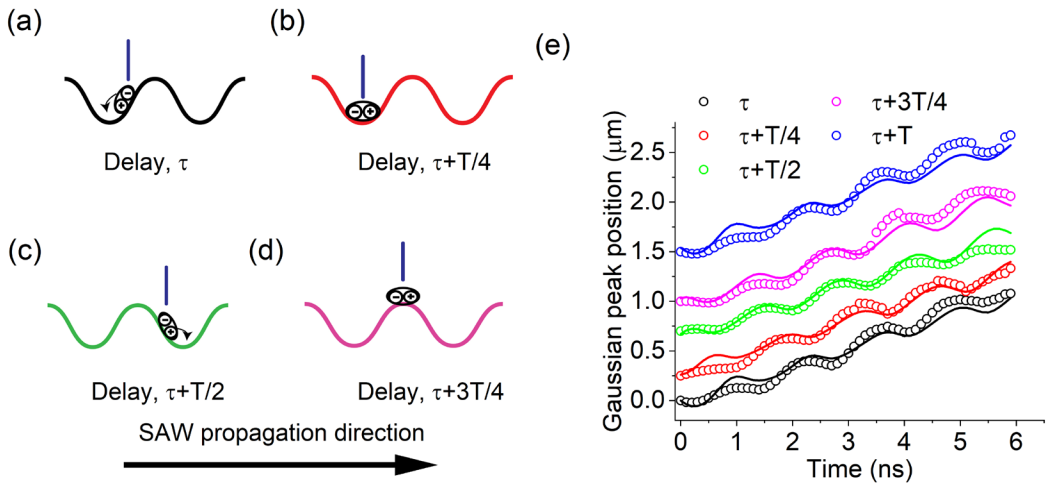

Figure 5-4: Spatiotemporally controlled energy transport under phase modulated optical excitation for 15 dBm RF excitation. Schematic presentation of photogenerated excitons at different SAW phases along with exciton potential: (a) τ; (b) τ + T/4; (c) τ + T/2; (d) τ + 3T/4. The vertical blue line represents the position of excitation pulse on SAW wave. For τ, the excitons are generated at a position such that the energetically stable position lies in the opposite direction of SAW propagation. Therefore, immediately after photogeneration, the exciton density distribution shifts in the opposite direction of SAW propagation. However, as the excitons couple to the traveling strain field, a net drift in the direction of SAW was observed. For τ+T/4, excitons are generated at the positions of lowest bandgap (position of maximum tensile strain corresponding to minimum exciton potential but lowest energy gradient). Hence, the exciton density distribution does not undergo immediate spatial shift after photogeneration. At τ+T/2, following photoexcitation, the energy gradient drives the exciton flux forward towards the stable position of maximum tensile strain. Therefore, the generated density distribution moves immediately in the direction of SAW propagation. For τ+3T/4, the excitons are generated at the position of maximum compressive strain *i.e.*, maximum bandgap and hence results in no spatial shift immediately after photogeneration. (e)Phase synchronized evolution of the gaussian peak position(circles) extracted by fitting the normalized exciton density measured using TCSPC technique. The gaussian peak position oscillates at the period of the SAW wave. A progressive delay in the Gaussian peak is also observed as the time delay is increased at an increment of T/4. Alongside oscillations, a net drift in the Gaussian peak is observed in the direction of acoustic wave propagation. The solid line in the figure shows numerical fit using the model discussed in the text.

5.6 Optical fluence as a possible control knob for exciton transport

In monolayer semiconductors, the exciton transport properties are strongly influenced by density-dependent non-linear phenomenon such as non-radiative Auger scattering [280], [304], halo formation [93], hot exciton effects [305], [306], non-equilibrium phonon drug effects [307]. While exciton transport under low optical excitation follows Fick's law [302], at elevated excitations, strong non-linear interactions result in a highly mobile excitonic species with large kinetic energy, and therefore density-dependent increment in mean squared displacement is observed [93], [302]. We also observe similar effects in our optical excitation-dependent transport measurements without RF excitation. We present the results of transport measurement at different exciton densities in the absence of RF excitation in Figure 5-5(a). As the exciton density is increased, a clear monotonic increase in the mean squared displacement is observed with the time evolution of the mean squared displacement becoming non-linear with excitation fluence, highlighting an increase in exciton diffusivity due to non-linear interactions. We note that the generated exciton density is still an order lower than the reported exciton-Mott transition in monolayer TMDs [227], [276] and therefore, the increase in mean squared displacement is not triggered by the exciton transition into the electron-hole liquid phase [308].

The results of transport measurement at a lower exciton density (0.2 $\mu J/cm^2$) under -60 dBm and 13 dBm RF excitation are shown in Figure 5-5(b) and Figure 5-5(c) respectively. In contrast to the normalized spatiotemporal exciton density presented in the previous section (Figure 5-2) under a higher excitation fluence, the average drift in the exciton population over time is suppressed. This is more clearly seen in the temporal evolution of the fitted gaussian peak under RF excitation (Figure 5-5(d)). Even though, the gaussian peak position shows signatures of oscillatory behavior under RF excitation, the average drift of the exciton population is smaller than

Figure 5-3(a) (discussed later in this section). This is attributed to the decrease in exciton kinetic energy at lower densities that further weakens the effective coupling of excitons to the traveling strain field. Figure 5-5(e) shows the TRPL measured at the minimum exciton density as a function of RF excitation that shows enhancement in exciton decay rate with RF power due to exciton dissociation which is also observed in the CW PL measurement.

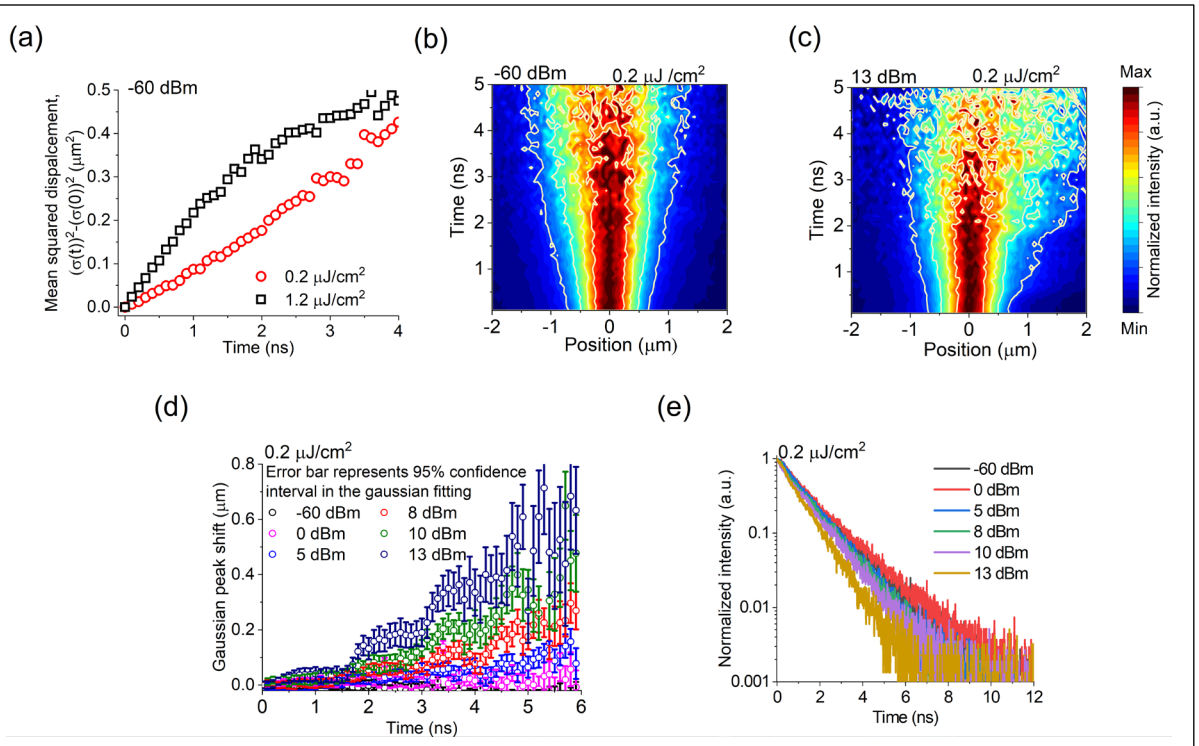

Figure 5-5: Optical excitation dependent exciton diffusion in h-BN/WSe_2/h-BN sample. (a) Mean squared displacement as a function of time at two exciton densities i.e. optical fluence under -60 dBm RF excitation. A clear increase in the mean squared displacement can be observed because of density dependent non-linear interactions. Spatiotemporally resolved normalized exciton density profile at the minimum optical fluence under (b) -60 dBm and (c) 13 dBm RF excitation. In comparison with the observed spatial translation in Figure 3-2, the spatial exciton drift is small. (d) Spatial shift in the gaussian peak position at different RF excitation. The error bars represent the uncertainties in the gaussian fitting of the measured exciton densities. (e) Time resolved photoluminescence at the minimum exciton density at different RF excitation. A strong RF excitation dependent increase in the exciton decay rate is observed due to reduced free carrier screening at lower optical fluence.

In Figure 5-6 we show the comparison between the transport dynamics at two optical generation densities under RF excitation. To capture the spatial transport of the exciton density under the surface acoustic wave, we subtract the spatiotemporal exciton density map at -60dBm RF excitation from 13 dBm RF excitation at two optical fluences. The subtracted spatiotemporal density contour maps are shown in Figure 5-6(a) and Figure 5-6(b) respectively. We observe that the exciton density shows stronger modulation under the SAW wave at higher optical fluence, a clear signature of higher kinetic energy, and therefore stronger coupling to the traveling strain wave. The stronger exciton coupling to the SAW wave at higher optical excitation is more clearly seen in Figure 5-6(c) and Figure 5-6(d) which shows normalized exciton densities at different time instances under 13 dBm RF excitation. Clearly, at higher optical excitation, excitons travel further due to improved coupling to the traveling strain wave. To verify this observation, we also fit the spatial shift of the gaussian peak position at 0.2 $\mu J/cm^2$ optical fluence under13 dBm RF excitation using linear fit and extract the average drift velocity to be 79± 3 m/s which is close to an order smaller than the average drift velocity extracted at higher optical fluence (1.2 $\mu J/cm^2$)(Figure 5-6(e)). The extracted average drift velocity, therefore, indicates stronger coupling at higher optical excitation due to highly mobile exciton species.

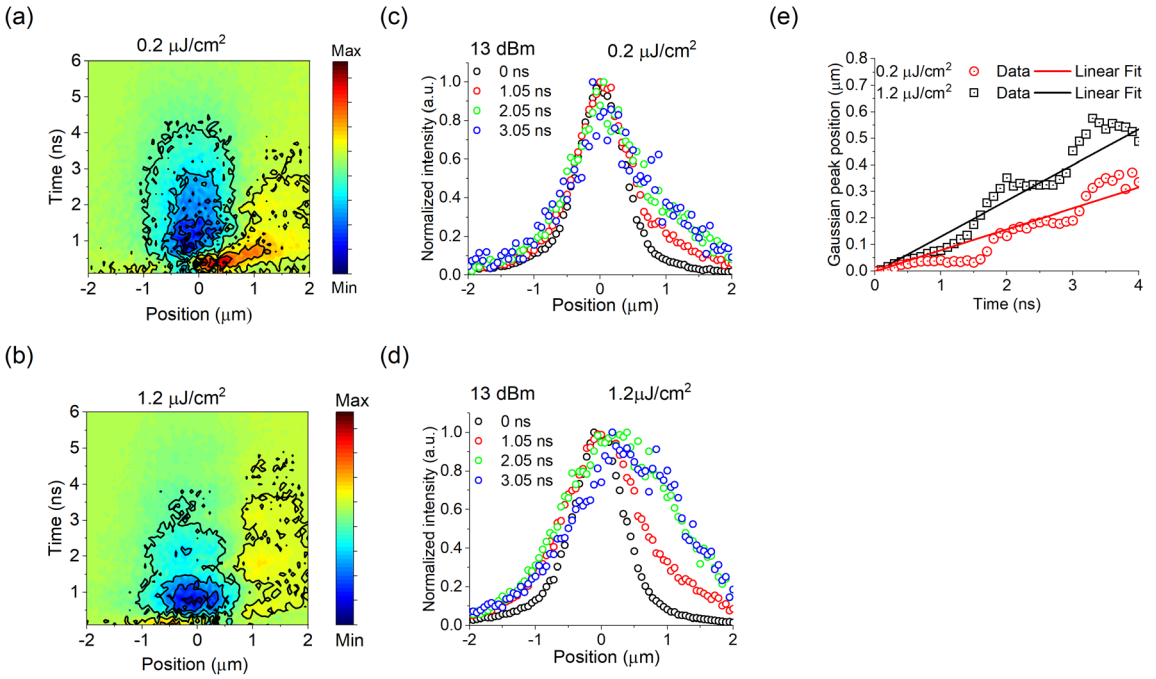

Figure 5-6: Optical excitation dependent exciton dynamics under RF excitation. Change in the spatiotemporally resolved exciton density map (density at lowest RF excitation (-60 dBm) subtracted from high RF excitation (13 dBm)) at (a) 0.2 μJ/cm^2 and (b) 1.2 μJ/cm^2 excitation fluence. Normalized exciton density at different time instances under 13 dBm RF excitation for (c) 0.2μJ/cm^2 and (d) 1.2 μJ/cm^2. (e) Peak position of the exciton density extracted from the gaussian fitting for two exciton densities under 13 dBm RF excitation. The average drift of exciton density under RF excitation is clearly higher for higher exciton density.

From our observations, we thereby conclude that the exciton transport by the SAW wave is triggered by exciton coupling to the traveling strain field in the medium under RF excitation (type – I band edge modulation). Even though we operate in the weak coupling regime (discussed in the previous section), the density-dependent transport properties of excitons also strongly affect

the extent of the coupling. At the same time, at lower excitation densities, exciton dissociation is strengthened by the weaker free carrier screening process (type – II band edge modulation). This further lowers the kinetic energy of the exciton density by exciton dissociation and further reduces the coupling efficiency to the traveling strain field. This results in a smaller average drift velocity for the same RF excitation power at lower optical fluence.

5.7 Summary

In summary, we demonstrated room-temperature, directed exciton energy transport in monolayer WSe_2 under a traveling strain field. The dynamic strain gradient obtained under the experimental condition was sufficient to study the weak coupling regime between excitons and the strain wave. Our results show that the weak coupling leads to oscillations in the transported exciton density since the exciton drift velocity is lower than the velocity of the traveling wave. Based on the measurement, we estimate the neutral exciton mobility in the monolayer to be 900 $cm^2/eV/s$ which is in good agreement with the values reported in the literature for the same material. The results show that coupling between excitons and dynamic strain waves in TMDs strongly depends on the transport properties and therefore, is expected to be influenced by various factors like intrinsic and extrinsic defect states, lattice disorders, substrate roughness, scattering from charged and neutral impurities. Hence, an improved material system with higher strain gradients would provide a pathway to reach the strong coupling regime. In addition, the use of TMD heterostructures that offer a long lifetime could aid in improving the overall transport length. Finally, we also demonstrated controlled acoustic steering of the photogenerated excitons by precisely tuning the exciton photogeneration with respect to the phase of the acoustic wave and

provide a modified drift-diffusion model to describe the observations. The reported results pave the way for exciting future applications that include efficient energy conversion, sensing, detection, and room temperature on-chip excitonic information processing and communication.

Chapter 6 Summary and Future Directions

In the previous chapters, we have included experimental results on manipulating excitonic photophysics in van der Waals solids – organic semiconductors and monolayer TMDs at room temperature. In chapter 3, we have demonstrated solid-state solvation in a doped host: guest media under axial tensile strain. Photoluminescence measurement reveals that the strain sensitivity of such organic doped host: guest media varies inversely with the guest doping. We have further demonstrated dynamic control over local molecular density by fabricating MEMs electrostatic thin film actuators. Contrary to traditional approaches like chemical synthesis or direct doping of the host media by guest molecules, such a platform that utilized residual stress of SiO_2 thin films can be highly beneficial for on-chip applications.

In chapter 4, we have discussed the photophysical manipulation of excitons at room temperature in a monolayer TMD system under strong dielectric screening by a piezoelectric field. A reduction in exciton binding energy under dielectric screening results in strong dissociation and photoluminescence quenching which can be further controlled by optical excitation. The observed excitation-dependent photophysical manipulation is further supported by the experimentally extracted neutral exciton polarizability, excitation-dependent broadening of exciton photoluminescence, and transient photoluminescence decay.

In chapter 5, we have tried to elucidate the physics of exciton transport under traveling strain waves in a monolayer semiconductor using phase synchronized picosecond resolved diffusion measurement techniques. We have demonstrated a delicate interplay between type – I

and type – II band edge modulation under a traveling acoustic field that governs the coupling of photogenerated excitons to the traveling strain field. From our observation, we conclude that the excitons in monolayer TMDs are expected to couple *weakly* to the traveling strain field at room temperature due to limited intrinsic mobility. We have demonstrated room-temperature *acoustic steering* by controlling exciton generation at different phases of the traveling acoustic field.

Although the results and analyses presented in this work show that exciton transport under dynamic strain wave in monolayer semiconductors at room temperature is expected to take place in the *weak coupling* regime, further improvements toward the *strong coupling* regime can be made by adopting approaches such as increasing RF power, increasing SAW frequency and so on. While such traditional approaches can lead to larger strain amplitude, the substrate-induced piezoelectric field is also expected to increase which would lead to larger exciton dissociation. Although optical excitation can be increased to screen the piezoelectric field, in TMD monolayers non-linear density-dependent processes such as exciton-exciton annihilation [309], transition to electron-hole plasma regime [310], [311] are expected to increase with excitation density and therefore such results need to be analyzed carefully.

Another viable approach could be the artificial enhancement of exciton coupling to the traveling strain wave by increasing the exciton mobility through strain engineering at room temperature. As the extent of coupling between photogenerated exciton density and traveling strain wave strongly depends on the intrinsic exciton mobility, exciton in strained TMDs should be highly suitable for transport under SAW. Theoretical bandstructure calculation shows that under tensile strain the electron and hole effective mass get reduced [126], [312], [313]. As a result, an exciton in a strained monolayer TMD is expected to have a lower translational mass and therefore can attain higher mobility and achieve better coupling to the traveling strain wave.

Further enhancement can be obtained by suppressing the lattice scattering at a lower temperature where the exciton mobility is expected to be limited by scattering from defect sites or impurities. Therefore, exciton coupling to traveling strain can be further improved in materials with ultra-low defect density at low temperatures.

Even though we have investigated exciton transport under traveling strain waves in TMD monolayers, other excitonic media that can sustain excitons with high binding energy and high exciton mobility can be utilized. With the recent progress of crystallization methods [314], [315] the intrinsic exciton mobility in various disordered systems can be improved to be used as the exciton transport media.

As discussed in Chapter 2, patterned substrates are traditionally used for generating non-uniform strain gradients in monolayer semiconductors. Due to their large flexibility and mechanical strength, once mechanically transferred on such patterned substrates, the monolayer adopts the pattern geometry without deformation and gets strained. The strain gradient generated using this approach can be used for directional exciton flux control. Such patterned substrates traditionally have fixed spatial dimensions and are typically fabricated using dry phase etching techniques [129], [316], [317]. However, due to the possible roughness of the etched sidewalls, the patterned regions can result in local strain hot-spots [318], [319]. An alternative and cost-effective approach for obtaining such nanoscale geometries can be wet chemical etching. In traditional substrates like thermally grown SiO_2/ Si, the etch rate of SiO_2 can be precisely controlled by the temperature and the concentration of the etchant solution [320], [321].

Gate tunable electrostatic potential modulation has long been used traditionally to direct exciton flux in III-V quantum well structures at cryogenic temperature [287], [289], [322], TMD heterostructures at cryogenic [288], [292], [323]–[325] and room temperature [291]. Application

of an electrostatic field normal to the exciton flow generated by a nonuniform strain gradient can be utilized to achieve excitonic switching.

Spatially indirect long-lived interlayer excitons in TMD hetero- bilayers are uniquely suited for achieving long-range exciton transport under strain not only because of their long lifetime but also for their larger deformation potential constant than the constituent monolayers [326], [327]. The exciton dipole moment in such hetero- bilayers is oriented out-of-plane and therefore the exciton energy can be tuned by applying an out-of-plane electric field. Under such a modulation scheme, the strained interlayer exciton potential can be gradually tuned along a fabricated *nano-ridge* geometry. This allows the creation of an *interlayer exciton link*.

Strained monolayer TMDs have been explored as potential candidates for realizing ultra-low dimensional single photon emitters that can be seamlessly integrated to nanophotonic platforms. Although waveguide coupled single photon emitters have been realized using monolayer WSe_2 on SiN/ Si substrates [318], [319] using anisotropic reactive ion etching techniques. The single photon emission takes place from the defect-bound states on the edge of the waveguide geometry and therefore such emitters suffer from inefficient modal overlap with the fundamental transverse electric (TE) mode of the waveguide. An improved single photon quantum source self-coupled to a waveguide can be realized by incorporating isotropic etching of silicon nitride [328], [329] into the widely used and well-understood anisotropic etching of silicon nitride.

Chapter 7 Conclusion

Engineering excitonic properties in van der Waals materials is critical for enhancing the integration bandwidth of excitonic devices ranging from low-loss, efficient applications such as energy conversion, information processing, and transfer to highly sensitive operations like sensing, and transduction. While chemical synthesis has long been investigated and traditionally adopted to be the go-to approach for engineering exciton photophysics in organic semiconductors, mechanical strain can offer an alternative route to enhance application as well as modular integration with current nanofabrication techniques. Despite extensive study on the effect of hydrostatic pressure on organic polymer and related materials, pressure-induced photophysical manipulation of small-molecule organic thin films has remained a largely unexplored area. On the other hand, high flexibility, ability to undergo large mechanical deformation, and high strain sensitivity makes external strain an exciting and aggressively studied tool for application-specific exciton engineering in TMDs. In this work, we have experimentally demonstrated pathways for exciton engineering in van der Waals materials at room temperature using strain as the primary modulation scheme for on-chip applications and possible modular integration with nano-fabrication and processing techniques. We have demonstrated a low-footprint reliable platform for modulating background polarizability in a small molecule host: guest media by decreasing the local molecular density. On the monolayer TMD materials, we have utilized strong background screening and optical generation as effective means for modulating excitonic photoluminescence under a traveling piezoelectric field. Finally, we have demonstrated directional exciton transport

under a traveling strain wave in a monolayer semiconductor at room temperature. We have also discussed possible future application directions and pathways to explore and further enhance the conceptual demonstrations discussed in this work. The results and observations noted in this work demonstrate that the strain-induced exciton engineering in van der Waals materials is still in infancy and significant research efforts are required to further understand and explore the exciting excitonic properties in TMDs under strain in both static and dynamic realms.

Appendices

Appendix A: Fabrication of Self-strained SiO_2 Microbeams for Solid-state Solvatochromism in Organic Host: Guest Media

The fabrication of the self-strained SiO_2 microbeams was carried out on thermally grown 300 nm SiO_2/ Si substrates. The fabrication process includes standard optical lithography and reactive ion etching (RIE) of the patterned oxide geometry. The fabrication of the microbeams includes the following steps:

1. **Optical lithography**
    a. The sample substrates were cleaned using acetone and isopropyl alcohol (IPA) in gentle to moderate sonication.
    b. Following solvent cleaning, vapor phase deposition of hexamethyldisilazane (HMDS) was performed to promote photoresist adhesion.
    c. As a photoresist, SPR 220 (3.0) was spin-coated at 5000 rpm (approximate thickness ~ 2 μm). The pre-exposure baking of the photoresist was carried out at 115° C for 90 sec.
    d. The samples were exposed in a contact aligner tool for 3.7 seconds. Post-exposure baking was carried out at 115° C for 90 sec. The exposed patterns were developed using AZ 726 in a double puddle recipe.

2. **Reactive ion etching of thermal SiO_2**

    a. The patterned SiO_2 regions were etched using CF_4 and CHF_3 gases (flow rate 15 sccm for both the gases). The RIE chamber pressure was kept at 20 mTorr. The RF power was set at 150 W.

    b. A short deep reactive ion etching (DRIE) step was performed for 60 seconds to etch exposed silicon to facilitate the access of XeF_2 gas used in the release of SiO_2 microbeams. For DRIE, SF6 (flow rate 390 sccm) was used as the etchant gas with C_4F_8 (flow rate 0-30 sccm, ramped) acting as the inert passivation layer.

    c. A short plasma stripping step was performed at low RF power (100 W) and low temperature (60º C) for 40 seconds to remove the C_4F_8 deposited on the sidewalls of the etched silicon region.

3. **Photoresist stripping:**

    a. The photoresist was stripped from the samples by immersing them in PRS 2000 at 60º C for 10 minutes.

    b. PRS immersion was followed by solvent cleaning using acetone and isopropyl alcohol (IPA) in moderate sonication.

4. **Evaporation of organic thin film**

    a. The organic thin film (Alq_3: DCM at different DCM doping) was evaporated using the vapor thermal deposition technique at 2e-6 Torr base pressure. The material thickness was kept at 30 nm. A further 50 nm TPBi was evaporated following the same vapor thermal deposition technique following the evaporation of Alq_3: DCM.

5. **Post-evaporation XeF_2 etching for releasing the microbeam structures**

    a. To release the microbeam structures, a short 3-cycle XeF_2 etching was performed at XeF_2 pressure kept at 3.0 Torr and N_2 pressure kept at 0.0 Torr. The cycle time was kept fixed at 20 s.

The detailed process flow can be found in Figure A1.

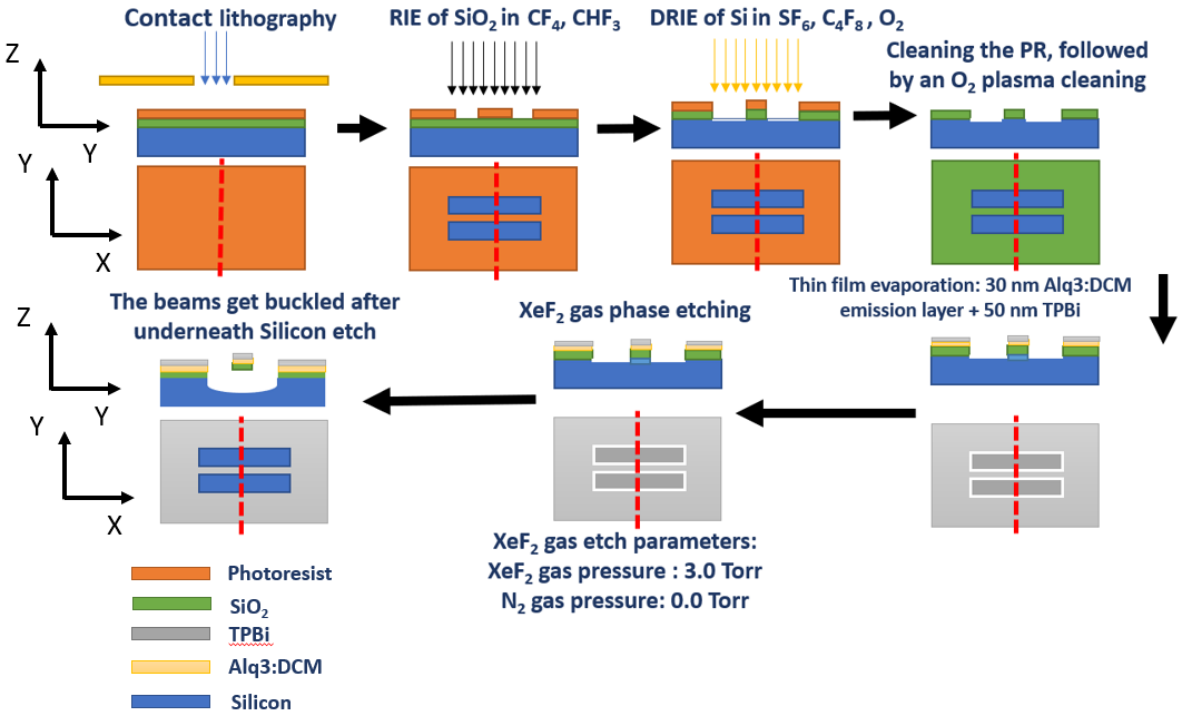

Figure A1: Process flow for fabrication of self-strained SiO_2 microbeams (not drawn to scale). The bottom figure in each of the process steps shows the top view of the device in XY plane. The red dashed line shows the line along which the YZ cross-section is taken. The top figure shows the YZ cross-section of the device structure in each process step. Reprinted with permission from ACS Appl. Nano Mater. 2020, 3, 2, 992–1001. Copyright 2019 American Chemical Society.

Appendix B: Fabrication and Characterization of MEMS Thin Film Membrane Devices on Si_3N_4/ Si Substrates

The fabrication of MEMs thin film membrane devices was carried out on low-pressure chemical vapor deposited (LPCVD) 300 nm Si_3N_4/ Si substrates. The fabrication process includes standard optical lithography and reactive ion etching (RIE) of the patterned oxide geometry. The fabrication of the microbeams includes the following steps:

1. **Optical lithography**
    a. The sample substrates were cleaned using acetone and IPA in gentle to moderate sonication.
    b. Following solvent cleaning, vapor phase deposition of hexamethyldisilazane (HMDS) was performed to promote photoresist adhesion.
    c. As a photoresist, SPR 220 (3.0) was spin-coated at 5000 rpm (approximate thickness ~ 2 μm). The pre-exposure baking of the photoresist was carried out at 115° C for 90 sec.
    d. The samples were exposed using a contact aligner tool for 3.8 seconds. Post-exposure baking was carried out at 115° C for 90 sec. The exposed patterns were developed using AZ 726 in a double puddle recipe.

2. **Reactive ion etching of LPCVD Si_3N_4**

    a. The patterned silicon nitride regions were etched in RIE chamber using CF_4(flow rate 40 sccm) and O_2 (flow rate 2 sccm). The RF power and the chamber pressure were kept at 80 W and 100 mTorr respectively.

    b. Following RIE, the photoresist mask was stripped by immersing the samples in PRS 2000 at 60º C. The samples were also cleaned in acetone and IPA using gentle to moderate sonication.

3. **Metal electrode patterning using optical lithography and deposition:**

    a. Following photoresist stripping and solvent cleaning from the last step, a second HMDS vapor phase deposition was performed to promote photoresist adhesion.

    b. Following the vapor prime step, SPR 220 (3.0) was spin-coated at 5000 rpm, followed by a pre-exposure bake at 115º C for 90 sec.

    c. The samples were exposed in a contact aligner for 3.8 seconds for patterning the metal electrodes. The exposed samples were baked for 90 sec at 115º C.

    d. A short photoresist descum step was performed at 60º C for 20 sec. The RF power was set at 100 W for the descum step.

    e. Following the photoresist descum, the metal evaporation (10 cm Cr / 150 nm Au) was carried out in an EBeam evaporator at a base pressure of 2e-6 Torr.

    f. The metal lift-off was carried out by immersing the samples in Acetone for 12 hours. Later the samples were cleaned using acetone and IPA in gentle sonication.

4. **XeF_2 vapor phase etching for the release of the MEMs membranes:**
    a. To release the MEMs membrane devices, 4 cycles of XeF_2 etching were performed. The XeF_2 and N_2 pressure were kept at 3.0 Torr and 0.0 Torr respectively. The etching cycle time was kept fixed at 20 seconds.

5. **PCB mounting of the devices for optical characterization under electrical excitation:**
    a. After the XeF_2 vapor phase etching step, the samples were mounted on a custom-designed printed circuit board (PCB) using adhesive Loctite-416.
    b. The metal contact pads on the PCB were bonded to the pads on the sample substrate using wire bonding. For wire bonding 0.7 mil (17.78 μm) Al wire was used.
6. **Evaporation of organic thin film**
    a. The organic thin film (1.5% DCM doped Alq_3: DCM) was evaporated using vapor thermal evaporation technique at 2e-6 Torr base pressure. The material thickness was kept at 30 nm.

The detailed process flow of fabrication can be found in Figure B1.

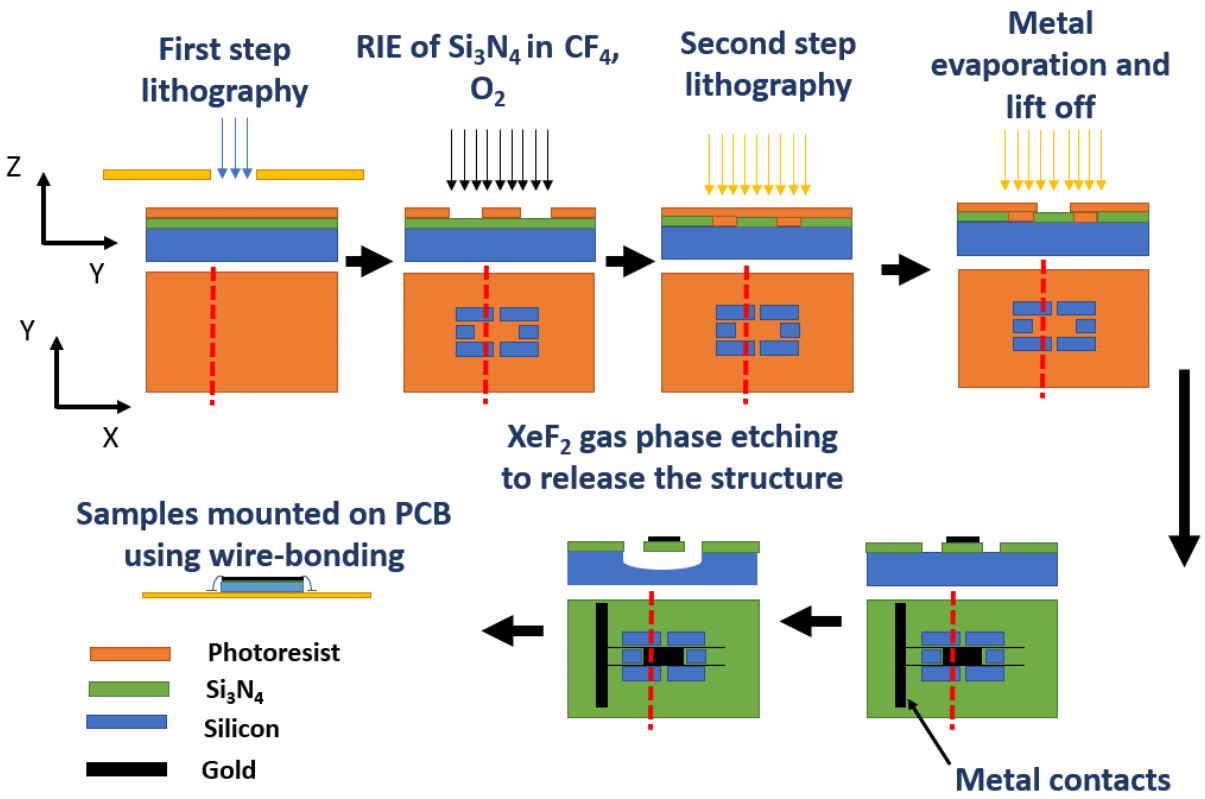

Figure B1: Process flow for the fabrication of MEMS thin film membrane devices on low stress Si_3N_4 along with XY plane top-view and YZ cross-sectional view of the device structure in each process step. The organic material evaporation is not shown here. The red dashed line shows the line along which the YZ cross-section is taken. Reprinted with permission from ACS Appl. Nano Mater. 2020, 3, 2, 992–1001. Copyright 2019 American Chemical Society.

Appendix C: Fabrication of SAW Filters on Piezoelectric $LiNbO_3$ Substrates

The fabrication of SAW filters was carried out on piezoelectric lithium niobate ($LiNbO_3$; 128º Y -cut) wafers using standard projection optical lithography and EBeam meatal evaporation. The detailed description of the fabrication steps is as follows:

1. **Fabrication of inter-digitated electrodes (IDTs) on $LiNbO_3$ substrates**
    a. The substrates were cleaned using acetone and IPA under gentle sonication.
    b. The lithography of the IDTs was carried out using a bilayer resist combination- PMGI SF6 as the lift-off resist and S1813 as the imaging resist. PMGI SF6 was spin-coated at 1000 rpm using manual dispensing. The pre-exposure baking was carried out at 195º C for 5 minutes. S1813 was spin-coated at 4000 rpm and was baked at 110º C for 4 minutes. The samples were then exposed to a 5X reduction projection lithography tool for 0.26 sec. No post-exposure baking was performed. The exposed patterns were developed using a double puddle recipe in AZ 726 MIF developer.
    c. The metal evaporation was carried out using EBeam evaporation at 2e-6 Torr base pressure. 10 nm Cr and 100 nm Au were deposited as the meatal stack for the IDTs. The metal lift-off was carried out by a two-step immersion in Remover PG. At first, the samples were kept soaked in remover PG for 12 hours. Then a second remover

PG bath was used with gentle agitation at 80º C temperature. The remover PG cleaning step was followed by a two-step IPA cleaning under gentle agitation.

2. Fabrication of contact pads for RF characterization and measurement:

a. Following the patterning of the IDTs, SPR 220(3.0) was spin-coated at 2800 rpm. Considering possible damage to the patterned IDTs due to the pyroelectric property of $LiNbO_3$ a slow and gradual thermal ramp step was adopted for pre-exposure baking of the spin-coated resist. Here, the samples were gradually ramped up from 35º C to 95º C using a hot plate. The samples were kept at 95º C for 4 min 30 sec and then the temperature was gradually reduced to 35º C. This ensured little damage to the patterned IDTs.

b. The samples were exposed using a projection lithography tool for 0.3 sec. No post-exposure baking was performed. The exposed patterns were developed using a double puddle recipe in AZ 726 MIF.

c. Following the development, 10 nm Cr and 500 nm Au were evaporated in an EBeam evaporator system at 2e-6 Torr base pressure. The metal lift-off was carried out following the same recipe as the IDT fabrication step.

Appendix D: Exciton Transport Measurement Setup

The optical characterization was carried out using a phase synchronized time-correlated single photon counting (TCSPC) setup. The sample was non-resonantly excited (Excitation wavelength 405 nm) using a pulsed diode (laser diode source - PicoQuant LDH P-C-405 and laser diode driver - PDL 800-D) laser producing pulses ~30 ps in duration. The photoluminescence signal was collected using a highly sensitive avalanche photodiode (MPD PDM series) through a 60X dry objective (NIKON CFI PLAN APO λ 60X / 0.95). The output of the APD was analyzed with a timing module (PicoQuant HydraHarp 400) of ~1 ps time resolution. The TCSPC setup was phase synchronized with a vector network analyzer (Agilent/HP 4396B - used as the RF signal source) using a variable pulsed delay generator (Stanford Research Systems DG645). To achieve complete phase synchronization, the output repetition rate from the delay generator was fixed at an integer multiple of the time-period of the RF signal. The output pulse stream (pulse width ~ 20 ns) from the delay generator was used to trigger the picosecond laser diode module. A complete schematic representation of the phase synchronized setup is given in Figure D1.

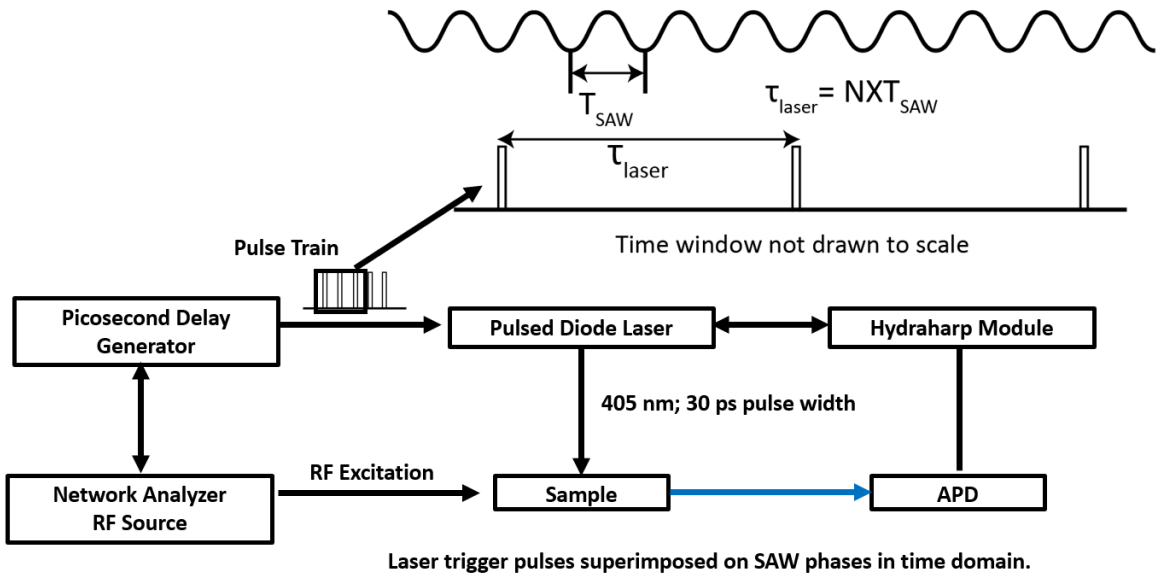

Figure D1: Timing diagram for phase synchronized TCSPC measurement. The internal clocks of the delay generator and the network analyzer are synchronized. The delay generator pulses are generated at a frequency $f_{laser} = \frac{f_{SAW}}{N}$; where N is an integer. The Hydraharp module is synchronized to the pulsed laser controller and is used to collect the sample photoluminescence using a highly sensitive avalanche photodetector (APD). Reproduced with permission from Springer Nature (Nat. Photon. 16, 242–247 (2022).)

Bibliography

[1] S. R. Forrest, *Organic Electronics : foundations to applications.* Oxford Univ Press, 2020.

[2] K. H. J. Buschow, M. C. Flemings, E. J. Kramer, and P. Veyssière, Eds., *Encyclopedia of Materials: Science and Technology*. Elsevier, 2001.

[3] Rubén Mas-Ballesté, Cristina Gómez-Navarro, Julio Gómez-Herrero, and Félix Zamora, "2D materials: to graphene and beyond," *Nanoscale*, vol. 3, no. 1, pp. 20–30, Jan. 2011

[4] M. Knupfer, "Exciton binding energies in organic semiconductors," *Appl. Phys. A 2003 775*, vol. 77, no. 5, pp. 623–626, Oct. 2003

[5] H.-W. Li, Z. Guan, Y. Cheng, T. Lui, Q. Yang, C.-S. Lee, S. Chen, S.-W. Tsang, H. Li, Y. Cheng, T. Lui, Q. Yang, S. Tsang, Z. Guan, C. Lee, and S. Chen, "On the Study of Exciton Binding Energy with Direct Charge Generation in Photovoltaic Polymers," *Adv. Electron. Mater.*, vol. 2, no. 11, p. 1600200, Nov. 2016

[6] J. Frenkel, "On the Transformation of light into Heat in Solids. I," *Phys. Rev.*, vol. 37, no. 1, p. 17, Jan. 1931

[7] G. H. Wannier, "The structure of electronic excitation levels in insulating crystals," *Phys. Rev.*, vol. 52, no. 3, pp. 191–197, 1937

[8] N. P. Wilson, W. Yao, J. Shan, and X. Xu, "Excitons and emergent quantum phenomena in stacked 2D semiconductors," *Nat. 2021 5997885*, vol. 599, no. 7885, pp. 383–392, Nov. 2021

[9] S. W. Koch, M. Kira, G. Khitrova, and H. M. Gibbs, "Semiconductor excitons in new light," *Nat. Mater.*, vol. 5, no. 7, pp. 523–531, 2006

[10] P. Johari and V. B. Shenoy, "Tuning the Electronic Properties of Semiconducting Transition Metal Dichalcogenides by Applying Mechanical Strains," *ACS Nano*, vol. 6, no. 6, pp. 5449–5456, Jun. 2012

[11] Y. Jing, B. Liu, X. Zhu, F. Ouyang, J. Sun, and Y. Zhou, "Tunable electronic structure of two-dimensional transition metal chalcogenides for optoelectronic applications," *Nanophotonics*, vol. 9, no. 7, pp. 1675–1694, Jul. 2020

[12] Z. Dai, L. Liu, Z. Zhang, Z. Dai, L. Liu, and Z. Zhang, "Strain Engineering of 2D

Materials: Issues and Opportunities at the Interface," *Adv. Mater.*, vol. 31, no. 45, p. 1805417, Nov. 2019

[13] Y. Yan, S. Ding, X. Wu, J. Zhu, D. Feng, X. Yang, and F. Li, "Tuning the physical properties of ultrathin transition-metal dichalcogenides via strain engineering," *RSC Adv.*, vol. 10, no. 65, pp. 39455–39467, Oct. 2020

[14] W. Chang, G. M. Akselrod, and V. Bulović, "Solid-state solvation and enhanced exciton diffusion in doped organic thin films under mechanical pressure," *ACS Nano*, vol. 9, no. 4, pp. 4412–4418, 2015

[15] M. Knaapila and S. Guha, "Blue emitting organic semiconductors under high pressure: status and outlook," *Reports Prog. Phys.*, vol. 79, no. 6, p. 066601, Apr. 2016

[16] K. Datta, Z. Li, and P. B. Deotare, "Effect of Strain on Excitons in Van Der Waals Solids," *Ref. Modul. Mater. Sci. Mater. Eng.*, 2022

[17] K. F. Mak and J. Shan, "Opportunities and challenges of interlayer exciton control and manipulation," *Nat. Nanotechnol. 2018 1311*, vol. 13, no. 11, pp. 974–976, Nov. 2018

[18] F. Liu, J. Zhou, C. Zhu, Z. Liu, F. Liu, J. Zhou, C. Zhu, and Z. Liu, "Electric Field Effect in Two-Dimensional Transition Metal Dichalcogenides," *Adv. Funct. Mater.*, vol. 27, no. 19, p. 1602404, May 2017

[19] S. Zhao, X. Li, B. Dong, H. Wang, H. Wang, Y. Zhang, Z. Han, and H. Zhang, "Valley manipulation in monolayer transition metal dichalcogenides and their hybrid systems: status and challenges," *Reports Prog. Phys.*, vol. 84, no. 2, p. 026401, Mar. 2021

[20] T. Smolenski, M. Goryca, M. Koperski, C. Faugeras, T. Kazimierczuk, A. Bogucki, K. Nogajewski, P. Kossacki, and M. Potemski, "Tuning valley polarization in a WSe_2 monolayer with a tiny magnetic field," *Phys. Rev. X*, vol. 6, no. 2, p. 021024, May 2016

[21] W. Chang, D. N. Congreve, E. Hontz, M. E. Bahlke, D. P. McMahon, S. Reineke, T. C. Wu, V. Bulović, T. Van Voorhis, and M. A. Baldo, "Spin-dependent charge transfer state design rules in organic photovoltaics," *Nat. Commun. 2015 61*, vol. 6, no. 1, pp. 1–6, Mar. 2015

[22] C. F. Madigan and V. Bulović, "Solid state solvation in amorphous organic thin films," *Phys. Rev. Lett.*, vol. 91, no. 24, pp. 1–4, 2003

[23] C. M. (V. Bulovic), "Solid State Solvation Effect," pp. 42–45

[24] A. Jayaraman, M. L. Kaplan, and P. H. Schmidt, "Effect of pressure on the Raman and electronic absorption spectra of naphthalene- and perylenetetracarboxylic dianhydrides," *J. Chem. Phys.*, vol. 82, no. 4, p. 1682, Aug. 1998

[25] H. G. Drickamer, "High pressure studies of molecular lumenescence," *Annu. Rev. Phys. Chem.*, vol. 33, no. 1, pp. 25–25, Jan. 1982

[26] C. A. M. Seidel and R. Kühnemuth, “Molecules under pressure,” *Nat. Nanotechnol.*, vol. 9, no. 3, pp. 164–165, 2014

[27] S. Stöttinger, G. Hinze, G. Diezemann, I. Oesterling, K. Müllen, and T. Basché, “Impact of local compressive stress on the optical transitions of single organic dye molecules,” *Nat. Nanotechnol.*, vol. 9, no. 3, pp. 182–186, 2014

[28] V. Bulović, R. Deshpande, M. . Thompson, and S. . Forrest, “Tuning the color emission of thin film molecular organic light emitting devices by the solid state solvation effect,” *Chem. Phys. Lett.*, vol. 308, no. 3–4, pp. 317–322, 1999

[29] V. Bulovic, M. A. Baldo, and S. R. Forrest, “Excitons and Energy Transfer in Doped Luminescent Molecular Organic Materials,” *Org. Electron. Mater.*, 2001

[30] V. Bulović, A. Shoustikov, M. A. Baldo, E. Bose, V. G. Kozlov, M. E. Thompson, and S. R. Forrest, “Bright, saturated, red-to-yellow organic light-emitting devices based on polarization-induced spectral shifts,” *Chem. Phys. Lett.*, vol. 287, no. 3–4, pp. 455–460, 1998

[31] A. Aït-Ouali, R. Y. F. Yip, J. L. Brebner, and R. A. Masut, “Strain relaxation and exciton localization effects on the Stokes shift in $InAs_xP_{1-x}$/InP multiple quantum wells,” *J. Appl. Phys.*, vol. 83, no. 6, p. 3153, Jun. 1998

[32] K. Kash, J. M. Worlock, M. D. Sturge, P. Grabbe, J. P. Harbison, A. Scherer, and P. S. D. Lin, “Strain-induced lateral confinement of excitons in GaAs-AlGaAs quantum well microstructures,” *Appl. Phys. Lett.*, vol. 53, no. 9, p. 782, Jun. 1998

[33] L. Sun, D. H. Kim, K. H. Oh, and R. Agarwal, “Strain-induced large exciton energy shifts in buckled CdS nanowires,” *Nano Lett.*, vol. 13, no. 8, pp. 3836–3842, Aug. 2013

[34] H. Chang Jeon, K. Jae Chung, and K. Jo Chung, “One-dimensional excitons in GaAs quantum wires,” *J. Phys. Condens. Matter*, vol. 10, no. 14, p. 3095, Apr. 1998

[35] Y. Chen, I. E. Zadeh, K. D. Jöns, A. Fognini, M. E. Reimer, J. Zhang, D. Dalacu, P. J. Poole, F. Ding, V. Zwiller, and O. G. Schmidt, “Controlling the exciton energy of a nanowire quantum dot by strain fields,” *Appl. Phys. Lett.*, vol. 108, no. 18, p. 182103, May 2016

[36] G. W. Bryant, M. Zieliński, N. Malkova, J. Sims, W. Jaskólski, and J. Aizpurua, “Effect of mechanical strain on the optical properties of quantum dots: Controlling exciton shape, orientation, and phase with a mechanical strain,” *Phys. Rev. Lett.*, vol. 105, no. 6, p. 067404, Aug. 2010

[37] A. I. Tartakovskii, M. N. Makhonin, I. R. Sellers, J. Cahill, A. D. Andreev, D. M. Whittaker, J. P. R. Wells, A. M. Fox, D. J. Mowbray, M. S. Skolnick, K. M. Groom, M. J. Steer, H. Y. Liu, and M. Hopkinson, “Effect of thermal annealing and strain engineering on the fine structure of quantum dot excitons,” *Phys. Rev. B - Condens. Matter Mater. Phys.*, vol. 70, no. 19, pp. 1–4, Nov. 2004

[38] A. Ramasubramaniam, “Large excitonic effects in monolayers of molybdenum and tungsten dichalcogenides,” *Phys. Rev. B - Condens. Matter Mater. Phys.*, vol. 86, no. 11, pp. 1–6, 2012

[39] H. P. Komsa and A. V. Krasheninnikov, “Effects of confinement and environment on the electronic structure and exciton binding energy of MoS_2 from first principles,” *Phys. Rev. B - Condens. Matter Mater. Phys.*, vol. 86, no. 24, p. 241201, Dec. 2012

[40] A. Castellanos-Gomez, M. Poot, G. A. Steele, H. S. J. Van Der Zant, N. Agraït, and G. Rubio-Bollinger, “Elastic Properties of Freely Suspended MoS_2 Nanosheets,” *Adv. Mater.*, vol. 24, no. 6, pp. 772–775, Feb. 2012

[41] D. Akinwande *et al.*, “A review on mechanics and mechanical properties of 2D materials—Graphene and beyond,” *Extrem. Mech. Lett.*, vol. 13, pp. 42–77, May 2017

[42] R. Roldán, A. Castellanos-Gomez, E. Cappelluti, and F. Guinea, “Strain engineering in semiconducting two-dimensional crystals,” *J. Phys. Condens. Matter*, vol. 27, no. 31, 2015

[43] Z. Peng, X. Chen, Y. Fan, D. J. Srolovitz, and D. Lei, “Strain engineering of 2D semiconductors and graphene: from strain fields to band-structure tuning and photonic applications,” *Light Sci. Appl. 2020 91*, vol. 9, no. 1, pp. 1–25, Nov. 2020

[44] J. Lee, S. J. Yun, C. Seo, K. Cho, T. S. Kim, G. H. An, K. Kang, H. S. Lee, and J. Kim, “Switchable, Tunable, and Directable Exciton Funneling in Periodically Wrinkled WS_2,” *Nano Lett.*, vol. 21, no. 1, pp. 43–50, Jan. 2021

[45] A. Castellanos-Gomez, R. Roldán, E. Cappelluti, M. Buscema, F. Guinea, H. S. J. Van Der Zant, and G. A. Steele, “Local strain engineering in atomically thin MoS_2,” *Nano Lett.*, vol. 13, no. 11, pp. 5361–5366, 2013

[46] J. W. Christopher, M. Vutukuru, D. Lloyd, J. S. Bunch, B. B. Goldberg, D. J. Bishop, and A. K. Swan, “Monolayer MoS_2 Strained to 1.3% with a microelectromechanical system,” *J. Microelectromechanical Syst.*, vol. 28, no. 2, pp. 254–263, 2019

[47] M. G. Harats, J. N. Kirchhof, M. Qiao, K. Greben, and K. I. Bolotin, “Dynamics and efficient conversion of excitons to trions in non-uniformly strained monolayer WS_2,” *Nat. Photonics 2020 145*, vol. 14, no. 5, pp. 324–329, Feb. 2020

[48] H. Moon, G. Grosso, C. Chakraborty, C. Peng, T. Taniguchi, K. Watanabe, and D. Englund, “Dynamic exciton funneling by local strain control in a monolayer semiconductor,” *Nano Lett.*, vol. 20, no. 9, pp. 6791–6797, 2020

[49] Y. Koo, Y. Kim, S. H. Choi, H. Lee, J. Choi, D. Y. Lee, M. Kang, H. S. Lee, K. K. Kim, G. Lee, and K. Park, “Tip-Induced Nano-Engineering of Strain, Bandgap, and Exciton Funneling in 2D Semiconductors,” *Adv. Mater.*, vol. 33, no. 17, p. 2008234, Mar. 2021

[50] M. Weiß and H. J. Krenner, “Interfacing quantum emitters with propagating surface

acoustic waves," *J. Phys. D. Appl. Phys.*, vol. 51, no. 37, p. 373001, Aug. 2018

[51] P. Delsing *et al.*, "The 2019 surface acoustic waves roadmap," *J. Phys. D. Appl. Phys.*, vol. 52, no. 35, p. 353001, Jul. 2019

[52] A. Violante, K. Cohen, S. Lazić, R. Hey, R. Rapaport, and P. V. Santos, "Dynamics of indirect exciton transport by moving acoustic fields," *New J. Phys.*, vol. 16, no. 3, p. 033035, Mar. 2014

[53] J. Rudolph, R. Hey, and P. V. Santos, "Long-range exciton transport by dynamic strain fields in a GaAs quantum well," *Phys. Rev. Lett.*, vol. 99, no. 4, pp. 1–4, 2007

[54] S. Lazić, A. Violante, K. Cohen, R. Hey, R. Rapaport, and P. V. Santos, "Scalable interconnections for remote indirect exciton systems based on acoustic transport," *Phys. Rev. B - Condens. Matter Mater. Phys.*, vol. 89, no. 8, pp. 1–8, 2014

[55] R. Peng, A. Ripin, Y. Ye, J. Zhu, C. Wu, S. Lee, H. Li, T. Taniguchi, K. Watanabe, T. Cao, X. Xu, and M. Li, "Long-range transport of 2D excitons with acoustic waves," *Nat. Commun. 2022 131*, vol. 13, no. 1, pp. 1–7, Mar. 2022

[56] K. J. Moore, G. Duggan, K. Woodbridge, and C. Roberts, "Observations and calculations of the exciton binding energy in (In,Ga)As/GaAs strained-quantum-well heterostructures," *Phys. Rev. B*, vol. 41, no. 2, p. 1090, Jan. 1990

[57] G. Duggan and H. I. Ralph, "Exciton binding energy in type-II GaAs-(Al,Ga)As quantum-well heterostructures," *Phys. Rev. B*, vol. 35, no. 8, p. 4152, Mar. 1987

[58] G. D. Scholes, "Long-Range Resonance Energy Transfer in Molecular Systems," *Annu. Rev. Phys. Chem.*, vol. 54, pp. 57–87, Nov. 2003

[59] W. A. Luhman and R. J. Holmes, "Investigation of Energy Transfer in Organic Photovoltaic Cells and Impact on Exciton Diffusion Length Measurements," *Adv. Funct. Mater.*, vol. 21, no. 4, pp. 764–771, Feb. 2011

[60] D. L. Dexter, R. S. Knox, and T. Förster, "The Radiationless Transfer of Energy of Electronic Excitation between Impurity Molecules in Crystals," *Phys. status solidi*, vol. 34, no. 2, pp. K159–K162, Jan. 1969

[61] D. L. Dexter, "A Theory of Sensitized Luminescence in Solids," *J. Chem. Phys.*, vol. 21, no. 5, p. 836, Dec. 2004

[62] O. V. Mikhnenko, P. W. M. Blom, and T.-Q. Nguyen, "Exciton diffusion in organic semiconductors," *Energy Environ. Sci.*, vol. 8, no. 7, pp. 1867–1888, Jul. 2015

[63] H. Najafov, B. Lee, Q. Zhou, L. C. Feldman, and V. Podzorov, "Observation of long-range exciton diffusion in highly ordered organic semiconductors," *Nat. Mater. 2010 911*, vol. 9, no. 11, pp. 938–943, Oct. 2010

[64] G. M. Akselrod, P. B. Deotare, N. J. Thompson, J. Lee, W. A. Tisdale, M. A. Baldo, V. M. Menon, and V. Bulovic, "Visualization of exciton transport in ordered and disordered molecular solids," *Nat. Commun.*, vol. 5, no. 1, pp. 1–8, 2014

[65] P. Mahato, A. Monguzzi, N. Yanai, T. Yamada, and N. Kimizuka, "Fast and long-range triplet exciton diffusion in metal–organic frameworks for photon upconversion at ultralow excitation power," *Nat. Mater. 2015 149*, vol. 14, no. 9, pp. 924–930, Aug. 2015

[66] S. Imani Yengejeh, W. Wen, and Y. Wang, "Mechanical properties of lateral transition metal dichalcogenide heterostructures," *Front. Phys. 2020 161*, vol. 16, no. 1, pp. 1–7, Oct. 2020

[67] H. Zhan, D. Guo, and G. X. Xie, "Two-dimensional layered materials: from mechanical and coupling properties towards applications in electronics," *Nanoscale*, vol. 11, no. 28, pp. 13181–13212, Jul. 2019

[68] G. Bin Liu, D. Xiao, Y. Yao, X. Xu, and W. Yao, "Electronic structures and theoretical modelling of two-dimensional group-VIB transition metal dichalcogenides," *Chem. Soc. Rev.*, vol. 44, no. 9, pp. 2643–2663, Apr. 2015

[69] T. Mueller and E. Malic, "Exciton physics and device application of two-dimensional transition metal dichalcogenide semiconductors," *npj 2D Mater. Appl. 2018 21*, vol. 2, no. 1, pp. 1–12, Sep. 2018

[70] M. Koperski, M. R. Molas, A. Arora, K. Nogajewski, A. O. Slobodeniuk, C. Faugeras, and M. Potemski, "Optical properties of atomically thin transition metal dichalcogenides: observations and puzzles," *Nanophotonics*, vol. 6, no. 6, pp. 1289–1308, Nov. 2017

[71] Y. Huang *et al.*, "Universal mechanical exfoliation of large-area 2D crystals," *Nat. Commun. 2020 111*, vol. 11, no. 1, pp. 1–9, May 2020

[72] F. Liu, "Mechanical exfoliation of large area 2D materials from vdW crystals," *Prog. Surf. Sci.*, vol. 96, no. 2, p. 100626, May 2021

[73] T. Severs Millard, A. Genco, E. M. Alexeev, S. Randerson, S. Ahn, A. R. Jang, H. Suk Shin, and A. I. Tartakovskii, "Large area chemical vapour deposition grown transition metal dichalcogenide monolayers automatically characterized through photoluminescence imaging," *npj 2D Mater. Appl. 2020 41*, vol. 4, no. 1, pp. 1–9, May 2020

[74] Y. Zhang, Y. Yao, M. G. Sendeku, L. Yin, X. Zhan, F. Wang, Z. Wang, and J. He, "Recent Progress in CVD Growth of 2D Transition Metal Dichalcogenides and Related Heterostructures," *Adv. Mater.*, vol. 31, no. 41, p. 1901694, Oct. 2019

[75] W. Pacuski, M. Grzeszczyk, K. Nogajewski, A. Bogucki, K. Oreszczuk, J. Kucharek, K. E. Połczyńska, B. Seredyński, A. Rodek, R. Bożek, T. Taniguchi, K. Watanabe, S. Kret, J. Sadowski, T. Kazimierczuk, M. Potemski, and P. Kossacki, "Narrow Excitonic Lines and Large-Scale Homogeneity of Transition-Metal Dichalcogenide Monolayers Grown by Molecular Beam Epitaxy on Hexagonal Boron Nitride," *Nano Lett.*, vol. 20, no. 5, pp.

3058–3066, May 2020

[76] S. Vishwanath, X. Liu, S. Rouvimov, L. Basile, N. Lu, A. Azcatl, K. Magno, R. M. Wallace, M. Kim, J. C. Idrobo, J. K. Furdyna, D. Jena, and H. G. Xing, "Controllable growth of layered selenide and telluride heterostructures and superlattices using molecular beam epitaxy," *J. Mater. Res.*, vol. 31, no. 7, pp. 900–910, Apr. 2016

[77] K. Lasek, J. Li, S. Kolekar, P. M. Coelho, L. Guo, M. Zhang, Z. Wang, and M. Batzill, "Synthesis and characterization of 2D transition metal dichalcogenides: Recent progress from a vacuum surface science perspective," *Surf. Sci. Rep.*, vol. 76, no. 2, p. 100523, May 2021

[78] J. K. Ellis, M. J. Lucero, and G. E. Scuseria, "The indirect to direct band gap transition in multilayered MoS_2 as predicted by screened hybrid density functional theory," *Appl. Phys. Lett.*, vol. 99, no. 26, p. 261908, Dec. 2011

[79] C. Pettenkofer, A. Klein, W. Jaegermann, S. Tiefenbacher, and V. Eyert, "Electronic band structure of single-crystal and single-layer WS_2: Influence of interlayer van der Waals interactions," *Phys. Rev. B*, vol. 64, no. 20, p. 205416, Nov. 2001

[80] G. Wang, A. Chernikov, M. M. Glazov, T. F. Heinz, X. Marie, T. Amand, and B. Urbaszek, "Colloquium: Excitons in atomically thin transition metal dichalcogenides," *Rev. Mod. Phys.*, vol. 90, no. 2, p. 021001, Apr. 2018

[81] K. Komider, J. W. González, and J. Fernández-Rossier, "Large spin splitting in the conduction band of transition metal dichalcogenide monolayers," *Phys. Rev. B - Condens. Matter Mater. Phys.*, vol. 88, no. 24, p. 245436, Dec. 2013

[82] Z. Y. Zhu, Y. C. Cheng, and U. Schwingenschlögl, "Giant spin-orbit-induced spin splitting in two-dimensional transition-metal dichalcogenide semiconductors," *Phys. Rev. B - Condens. Matter Mater. Phys.*, vol. 84, no. 15, p. 153402, Oct. 2011

[83] R. Roldán, J. A. Silva-Guillén, M. P. López-Sancho, F. Guinea, E. Cappelluti, and P. Ordejón, "Electronic properties of single-layer and multilayer transition metal dichalcogenides MX_2 (M = Mo, W and X = S, Se)," *Ann. Phys.*, vol. 526, no. 9–10, pp. 347–357, Oct. 2014

[84] H. Shi, H. Pan, Y. W. Zhang, and B. I. Yakobson, "Quasiparticle band structures and optical properties of strained monolayer MoS_2 and WS_2," *Phys. Rev. B - Condens. Matter Mater. Phys.*, vol. 87, no. 15, pp. 1–8, 2013

[85] W. Zhao, R. M. Ribeiro, and G. Eda, "Electronic structure and optical signatures of semiconducting transition metal dichalcogenide nanosheets," *Acc. Chem. Res.*, vol. 48, no. 1, pp. 91–99, Jan. 2015

[86] A. Kuc, N. Zibouche, and T. Heine, "Influence of quantum confinement on the electronic structure of the transition metal sulfide TS_2," *Phys. Rev. B - Condens. Matter Mater. Phys.*, vol. 83, no. 24, p. 245213, Jun. 2011

[87] K. F. Mak, K. He, J. Shan, and T. F. Heinz, “Control of valley polarization in monolayer MoS2by optical helicity,” *Nat. Nanotechnol.*, vol. 7, no. 8, pp. 494–498, 2012

[88] W. Yao, D. Xiao, and Q. Niu, “Valley-dependent optoelectronics from inversion symmetry breaking,” *Phys. Rev. B - Condens. Matter Mater. Phys.*, vol. 77, no. 23, p. 235406, Jun. 2008

[89] T. Cao, G. Wang, W. Han, H. Ye, C. Zhu, J. Shi, Q. Niu, P. Tan, E. Wang, B. Liu, and J. Feng, “Valley-selective circular dichroism of monolayer molybdenum disulphide,” *Nat. Commun. 2012 31*, vol. 3, no. 1, pp. 1–5, Jun. 2012

[90] A. J. Goodman, D. H. Lien, G. H. Ahn, L. L. Spiegel, M. Amani, A. P. Willard, A. Javey, and W. A. Tisdale, “Substrate-Dependent Exciton Diffusion and Annihilation in Chemically Treated MoS_2 and WS_2,” *J. Phys. Chem. C*, vol. 124, no. 22, pp. 12175–12184, Jun. 2020

[91] F. Cadiz, C. Robert, E. Courtade, M. Manca, L. Martinelli, T. Taniguchi, K. Watanabe, T. Amand, A. C. H. Rowe, D. Paget, B. Urbaszek, and X. Marie, “Exciton diffusion in WSe_2 monolayers embedded in a van der Waals heterostructure,” *Appl. Phys. Lett.*, vol. 112, no. 15, p. 152106, Apr. 2018

[92] J. W. Kang, J. W. Jung, T. Lee, J. G. Kim, and C. H. Cho, “Enhancing exciton diffusion in monolayer WS_2 with h- BN bottom layer,” *Phys. Rev. B*, vol. 100, no. 20, p. 205304, Nov. 2019

[93] M. Kulig, J. Zipfel, P. Nagler, S. Blanter, C. Schüller, T. Korn, N. Paradiso, M. M. Glazov, and A. Chernikov, “Exciton Diffusion and Halo Effects in Monolayer Semiconductors,” *Phys. Rev. Lett.*, vol. 120, no. 20, p. 207401, May 2018

[94] D. F. Cordovilla Leon, Z. Li, S. W. Jang, C. H. Cheng, and P. B. Deotare, “Exciton transport in strained monolayer WSe_2,” *Appl. Phys. Lett.*, vol. 113, no. 25, p. 252101, 2018

[95] S. V. Morozov, K. S. Novoselov, M. I. Katsnelson, F. Schedin, D. C. Elias, J. A. Jaszczak, and A. K. Geim, “Giant intrinsic carrier mobilities in graphene and its bilayer,” *Phys. Rev. Lett.*, vol. 100, no. 1, p. 016602, Jan. 2008

[96] E. H. Hwang, S. Adam, and S. Das Sarma, “Carrier transport in two-dimensional graphene layers,” *Phys. Rev. Lett.*, vol. 98, no. 18, p. 186806, May 2007

[97] J. Wierzbowski, J. Klein, F. Sigger, C. Straubinger, M. Kremser, T. Taniguchi, K. Watanabe, U. Wurstbauer, A. W. Holleitner, M. Kaniber, K. Müller, and J. J. Finley, “Direct exciton emission from atomically thin transition metal dichalcogenide heterostructures near the lifetime limit,” *Sci. Rep.*, vol. 7, no. 1, pp. 1–6, Dec. 2017

[98] C. R. Dean, A. F. Young, I. Meric, C. Lee, L. Wang, S. Sorgenfrei, K. Watanabe, T. Taniguchi, P. Kim, K. L. Shepard, and J. Hone, “Boron nitride substrates for high-quality graphene electronics,” *Nat. Nanotechnol.*, vol. 5, no. 10, pp. 722–726, 2010

[99] Z. Li, D. F. C. Leon, W. Lee, K. Datta, Z. Lyu, J. Hou, T. Taniguchi, K. Watanabe, E. Kioupakis, and P. B. Deotare, "Dielectric Engineering for Manipulating Exciton Transport in Semiconductor Monolayers," *Nano Lett.*, p. acs.nanolett.1c02990, Sep. 2021

[100] H. G. Drickamer and C. W. Frank, *Electronic Transitions and the High Pressure Chemistry and Physics of Solids*. Springer Netherlands, 1973.

[101] H. G. Drickamer, C. W. Frank, and C. P. Slichter, "Optical Versus Thermal Transitions in Solids at High Pressure," *Proc. Natl. Acad. Sci.*, vol. 69, no. 4, pp. 933–937, Apr. 1972

[102] J. K. Grey and I. S. Butler, "Effects of high external pressures on the electronic spectra of coordination compounds," *Coord. Chem. Rev.*, vol. 219–221, pp. 713–759, Oct. 2001

[103] A. Facchetti, "π-Conjugated polymers for organic electronics and photovoltaic cell applications," *Chem. Mater.*, vol. 23, no. 3, pp. 733–758, Feb. 2011

[104] S. Guha and M. Chandrasekhar, "Photophysics of organic emissive semiconductors under hydrostatic pressure," *Phys. status solidi*, vol. 241, no. 14, pp. 3318–3327, Nov. 2004

[105] S. Guha, M. Chandrasekhar, U. Scherf, and M. Knaapila, "Tuning structural and optical properties of blue-emitting polymeric semiconductors," *Phys. status solidi*, vol. 248, no. 5, pp. 1083–1090, May 2011

[106] P. Puschnig, K. Hummer, C. Ambrosch-Draxl, G. Heimel, M. Oehzelt, and R. Resel, "Electronic, optical, and structural properties of oligophenylene molecular crystals under high pressure: An *ab initio* investigation," *Phys. Rev. B*, vol. 67, no. 23, p. 235321, Jun. 2003

[107] S. Webster and D. N. Batchelder, "Absorption, luminescence and Raman spectroscopy of poly(p-phenylene vinylene) at high pressure," *Polymer (Guildf).*, vol. 37, no. 22, pp. 4961–4968, Oct. 1996

[108] B. C. Hess, G. S. Kanner, and Z. Vardeny, "Photoexcitations in polythiophene at high pressure," *Phys. Rev. B*, vol. 47, no. 3, p. 1407, Jan. 1993

[109] M. Knaapila, Z. Konôpková, M. Torkkeli, D. Haase, H. P. Liermann, S. Guha, and U. Scherf, "Structural study of helical polyfluorene under high quasihydrostatic pressure," *Phys. Rev. E - Stat. Nonlinear, Soft Matter Phys.*, vol. 87, no. 2, p. 022602, Feb. 2013

[110] K. Paudel, H. Knoll, M. Chandrasekhar, and S. Guha, "Tuning intermolecular interactions in dioctyl-substituted polyfluorene via hydrostatic pressure," *J. Phys. Chem. A*, vol. 114, no. 13, pp. 4680–4688, Apr. 2010

[111] S.-C. Yang, W. Graupner, S. Guha, P. Puschnig, C. Martin, H. R. Chandrasekhar, M. Chandrasekhar, G. Leising, C. Ambrosch-Draxl, and U. Scherf, "Geometry-Dependent Electronic Properties of Highly Fluorescent Conjugated Molecules," *Phys. Rev. Lett.*, vol. 85, no. 11, p. 2388, Sep. 2000

[112] J. P. Schmidtke, R. H. Friend, and C. Silva, “Tuning Interfacial Charge-Transfer Excitons at Polymer-Polymer Heterojunctions under Hydrostatic Pressure,” *Phys. Rev. Lett.*, vol. 100, no. 15, p. 157401, Apr. 2008

[113] Y.-S. Huang, J. Gierschner, J. P. Schmidtke, R. H. Friend, and D. Beljonne, “Tuning interchain and intrachain interactions in polyfluorene copolymers,” *Phys. Rev. B*, vol. 84, no. 20, p. 205311, Nov. 2011

[114] A. Köhler and H. Bässler, “Triplet states in organic semiconductors,” *Mater. Sci. Eng. R Reports*, vol. 66, no. 4–6, pp. 71–109, Nov. 2009

[115] C. Botta, S. Luzzati, R. Tubino, D. D. C. Bradley, and R. H. Friend, “Photoinduced absorption of polymer solutions,” *Phys. Rev. B*, vol. 48, no. 20, p. 14809, Nov. 1993

[116] K. Paudel, D. Moghe, M. Chandrasekhar, P. Yu, S. Ramasesha, U. Scherf, and S. Guha, “Pressure dependence of singlet and triplet excitons in amorphous polymer semiconductors,” *Europhys. Lett.*, vol. 104, no. 2, p. 27008, Nov. 2013

[117] K. W. Ang, C. H. Tung, N. Balasubramanian, G. S. Samudra, and Y. C. Yeo, “Strained n-channel transistors with silicon source and drain regions and embedded silicon/germanium as strain-transfer structure,” *IEEE Electron Device Lett.*, vol. 28, no. 7, pp. 609–612, Jul. 2007

[118] J. Welser, J. L. Hoyt, and J. F. Gibbons, “Electron mobility enhancement in strained-Si N-type metal-oxide-semiconductor field-effect transistors,” *IEEE Electron Device Lett.*, vol. 15, no. 3, pp. 100–102, Mar. 1994

[119] H. H. Hall, J. Bardeen, and G. L. Pearson, “The Effects of Pressure and Temperature on the Resistance of p-n Junctions in Germenium,” *Phys. Rev.*, vol. 84, no. 1, p. 129, Oct. 1951

[120] J. A. Del Alamo, “Nanometre-scale electronics with III–V compound semiconductors,” *Nature*, vol. 479, no. 7373, pp. 317–323, Nov. 2011

[121] X. Fu, G. Jacopin, M. Shahmohammadi, R. Liu, M. Benameur, J. D. Ganière, J. Feng, W. Guo, Z. M. Liao, B. Deveaud, and D. Yu, “Exciton drift in semiconductors under uniform strain gradients: Application to bent ZnO microwires,” *ACS Nano*, vol. 8, no. 4, pp. 3412–3420, Apr. 2014

[122] S. Aas and C. Bulutay, “Strain dependence of photoluminescence and circular dichroism in transition metal dichalcogenides: a *k.p* analysis,” *Opt. Express*, vol. 26, no. 22, p. 28672, Oct. 2018

[123] E. Scalise, M. Houssa, G. Pourtois, V. Afanas’ev, and A. Stesmans, “Strain-induced semiconductor to metal transition in the two-dimensional honeycomb structure of MoS_2,” *Nano Res. 2012 51*, vol. 5, no. 1, pp. 43–48, Nov. 2011

[124] H. Lee, Y. Koo, J. Choi, S. Kumar, H. T. Lee, G. Ji, S. H. Choi, M. Kang, K. K. Kim, H.

R. Park, H. Choo, and K. D. Park, “Drift-dominant exciton funneling and trion conversion in 2D semiconductors on the nanogap,” *Sci. Adv.*, vol. 8, no. 5, p. 5236, Feb. 2022

[125] J. Feng, X. Qian, C. W. Huang, and J. Li, “Strain-engineered artificial atom as a broad-spectrum solar energy funnel,” *Nat. Photonics*, vol. 6, no. 12, pp. 866–872, 2012

[126] Le Huang, Zhanghui Chen, and Jingbo Li, “Effects of strain on the band gap and effective mass in two-dimensional monolayer GaX (X = S, Se, Te),” *RSC Adv.*, vol. 5, no. 8, pp. 5788–5794, Dec. 2014

[127] M. Hosseini, M. Elahi, M. Pourfath, and D. Esseni, “Strain-induced modulation of electron mobility in single-layer transition metal dichalcogenides MX_2 (M = Mo, W; X = S, Se),” *IEEE Trans. Electron Devices*, vol. 62, no. 10, pp. 3192–3198, Oct. 2015

[128] S. Yang, Y. Chen, and C. Jiang, “Strain engineering of two-dimensional materials: Methods, properties, and applications,” *InfoMat*, vol. 3, no. 4, pp. 397–420, Apr. 2021

[129] F. Kleinermann, N. J. Avis, S. K. Judah, al -, M. Ozawa, S. Arai, L. Tao, W. Ou, Y. Li, H. Liao, J. Zhang, F. Gan, and X. Ou, “Recent advances in mechanical strain engineering of low-dimensional semiconductors and their applications in high-performance quantum emitters,” *Semicond. Sci. Technol.*, vol. 35, no. 10, p. 103002, Sep. 2020

[130] C. Lee, X. Wei, J. W. Kysar, and J. Hone, “Measurement of the elastic properties and intrinsic strength of monolayer graphene,” *Science (80-.).*, vol. 321, no. 5887, pp. 385–388, Jul. 2008

[131] M. Ghorbani-Asl, S. Borini, A. Kuc, and T. Heine, “Strain-dependent modulation of conductivity in single-layer transition-metal dichalcogenides,” *Phys. Rev. B - Condens. Matter Mater. Phys.*, vol. 87, no. 23, p. 235434, Jun. 2013

[132] Z. Li, Y. Lv, L. Ren, J. Li, L. Kong, Y. Zeng, Q. Tao, R. Wu, H. Ma, B. Zhao, D. Wang, W. Dang, K. Chen, L. Liao, X. Duan, X. Duan, and Y. Liu, “Efficient strain modulation of 2D materials via polymer encapsulation,” *Nat. Commun.*, vol. 11, no. 1, pp. 1–8, Dec. 2020

[133] M. Velický and P. S. Toth, “From two-dimensional materials to their heterostructures: An electrochemist’s perspective,” *Appl. Mater. Today*, vol. 8, pp. 68–103, Sep. 2017

[134] O. B. Aslan, M. Deng, and T. F. Heinz, “Strain tuning of excitons in monolayer WSe_2,” *Phys. Rev. B*, vol. 98, no. 11, p. 115308, Sep. 2018

[135] S. B. Desai, G. Seol, J. S. Kang, H. Fang, C. Battaglia, R. Kapadia, J. W. Ager, J. Guo, and A. Javey, “Strain-induced indirect to direct bandgap transition in multilayer WSe_2,” *Nano Lett.*, vol. 14, no. 8, pp. 4592–4597, 2014

[136] I. Niehues, R. Schmidt, M. Drüppel, P. Marauhn, D. Christiansen, M. Selig, G. Berghäuser, D. Wigger, R. Schneider, L. Braasch, R. Koch, A. Castellanos-Gomez, T. Kuhn, A. Knorr, E. Malic, M. Rohlfing, S. Michaelis De Vasconcellos, and R.

Bratschitsch, “Strain Control of Exciton-Phonon Coupling in Atomically Thin Semiconductors,” *Nano Lett.*, vol. 18, no. 3, pp. 1751–1757, Mar. 2018

[137] O. B. Aslan, M. Deng, M. L. Brongersma, and T. F. Heinz, “Strained bilayer WSe_2 with reduced exciton-phonon coupling,” *Phys. Rev. B*, vol. 101, no. 11, p. 115305, Mar. 2020

[138] K. P. Dhakal, S. Roy, H. Jang, X. Chen, W. S. Yun, H. Kim, J. Lee, J. Kim, and J. H. Ahn, “Local Strain Induced Band Gap Modulation and Photoluminescence Enhancement of Multilayer Transition Metal Dichalcogenides,” *Chem. Mater.*, vol. 29, no. 12, pp. 5124–5133, Jun. 2017

[139] H. J. Conley, B. Wang, J. I. Ziegler, R. F. Haglund, S. T. Pantelides, and K. I. Bolotin, “Bandgap engineering of strained monolayer and bilayer MoS_2,” *Nano Lett.*, vol. 13, no. 8, pp. 3626–3630, 2013

[140] O. B. Aslan, I. M. Datye, M. J. Mleczko, K. Sze Cheung, S. Krylyuk, A. Bruma, I. Kalish, A. V. Davydov, E. Pop, and T. F. Heinz, “Probing the Optical Properties and Strain-Tuning of Ultrathin $Mo_{1-x}W_xTe_2$,” *Nano Lett.*, vol. 18, no. 4, pp. 2485–2491, Apr. 2018

[141] H. H. Pérez Garza, E. W. Kievit, G. F. Schneider, and U. Staufer, “Controlled, reversible, and nondestructive generation of uniaxial extreme strains (>10%) in graphene,” *Nano Lett.*, vol. 14, no. 7, pp. 4107–4113, Jul. 2014

[142] C. Martella, C. Mennucci, E. Cinquanta, A. Lamperti, E. Cappelluti, F. Buatier De Mongeot, and A. Molle, “Anisotropic MoS_2 Nanosheets Grown on Self-Organized Nanopatterned Substrates,” *Adv. Mater.*, vol. 29, no. 19, p. 1605785, May 2017

[143] A. Branny, S. Kumar, R. Proux, and B. D. Gerardot, “Deterministic strain-induced arrays of quantum emitters in a two-dimensional semiconductor,” *Nat. Commun.*, vol. 8, no. 1, pp. 1–7, 2017

[144] C. Palacios-Berraquero, D. M. Kara, A. R. P. Montblanch, M. Barbone, P. Latawiec, D. Yoon, A. K. Ott, M. Loncar, A. C. Ferrari, and M. Atatüre, “Large-scale quantum-emitter arrays in atomically thin semiconductors,” *Nat. Commun.*, vol. 8, no. 1, pp. 1–6, May 2017

[145] M. Kremser, M. Brotons-Gisbert, J. Knörzer, J. Gückelhorn, M. Meyer, M. Barbone, A. V. Stier, B. D. Gerardot, K. Müller, and J. J. Finley, “Discrete interactions between a few interlayer excitons trapped at a $MoSe_2$–WSe_2 heterointerface,” *npj 2D Mater. Appl. 2020 41*, vol. 4, no. 1, pp. 1–6, May 2020

[146] V. S. Mangu, M. Zamiri, S. R. J. Brueck, and F. Cavallo, “Strain engineering, efficient excitonic photoluminescence, and exciton funnelling in unmodified MoS_2 nanosheets,” *Nanoscale*, vol. 9, no. 43, pp. 16602–16606, Nov. 2017

[147] F. Dirnberger, J. D. Ziegler, P. E. F. Junior, R. Bushati, T. Taniguchi, K. Watanabe, J. Fabian, D. Bougeard, A. Chernikov, and V. M. Menon, “Quasi-1D exciton channels in strain-engineered 2D materials,” *Sci. Adv.*, vol. 7, no. 44, pp. 3066–3095, Oct. 2021

[148] S. Yang, C. Wang, H. Sahin, H. Chen, Y. Li, S. S. Li, A. Suslu, F. M. Peeters, Q. Liu, J. Li, and S. Tongay, "Tuning the optical, magnetic, and electrical properties of $ReSe_2$ by nanoscale strain engineering," *Nano Lett.*, vol. 15, no. 3, pp. 1660–1666, Mar. 2015

[149] E. Blundo, M. Felici, T. Yildirim, G. Pettinari, D. Tedeschi, A. Miriametro, B. Liu, W. Ma, Y. Lu, and A. Polimeni, "Evidence of the direct-to-indirect band gap transition in strained two-dimensional WS_2, MoS_2, and WSe_2," *Phys. Rev. Res.*, vol. 2, no. 1, p. 012024, Jan. 2020

[150] Y. M. He, G. Clark, J. R. Schaibley, Y. He, M. C. Chen, Y. J. Wei, X. Ding, Q. Zhang, W. Yao, X. Xu, C. Y. Lu, and J. W. Pan, "Single quantum emitters in monolayer semiconductors," *Nat. Nanotechnol.*, vol. 10, no. 6, pp. 497–502, Jun. 2015

[151] I. Aharonovich, D. Englund, and M. Toth, "Solid-state single-photon emitters," *Nat. Photonics*, vol. 10, no. 10, pp. 631–641, Sep. 2016

[152] C. Chakraborty, N. Vamivakas, and D. Englund, "Advances in quantum light emission from 2D materials," *Nanophotonics*, vol. 8, no. 11, pp. 2017–2032, Nov. 2019

[153] S. Kumar, A. Kaczmarczyk, and B. D. Gerardot, "Strain-Induced Spatial and Spectral Isolation of Quantum Emitters in Mono- and Bilayer WSe_2," *Nano Lett.*, vol. 15, no. 11, pp. 7567–7573, 2015

[154] M. R. Rosenberger, C. K. Dass, H. J. Chuang, S. V. Sivaram, K. M. McCreary, J. R. Hendrickson, and B. T. Jonker, "Quantum Calligraphy: Writing Single-Photon Emitters in a Two-Dimensional Materials Platform," *ACS Nano*, vol. 13, no. 1, pp. 904–912, Jan. 2019

[155] X. X. Song, D. Liu, V. Mosallanejad, J. You, T. Y. Han, D. T. Chen, H. O. Li, G. Cao, M. Xiao, G. C. Guo, and G. P. Guo, "A gate defined quantum dot on the two-dimensional transition metal dichalcogenide semiconductor WSe_2," *Nanoscale*, vol. 7, no. 40, pp. 16867–16873, Oct. 2015

[156] J. P. So, H. R. Kim, H. Baek, K. Y. Jeong, H. C. Lee, W. Huh, Y. S. Kim, K. Watanabe, T. Taniguchi, J. Kim, C. H. Lee, and H. G. Park, "Electrically driven strain-induced deterministic single-photon emitters in a van der Waals heterostructure," *Sci. Adv.*, vol. 7, no. 43, Oct. 2021

[157] M. Cotrufo, L. Sun, J. Choi, A. Alù, and X. Li, "Enhancing functionalities of atomically thin semiconductors with plasmonic nanostructures," *Nanophotonics*, vol. 8, no. 4, pp. 577–598, Apr. 2019

[158] Y. Luo, G. D. Shepard, J. V. Ardelean, D. A. Rhodes, B. Kim, K. Barmak, J. C. Hone, and S. Strauf, "Deterministic coupling of site-controlled quantum emitters in monolayer WSe2 to plasmonic nanocavities," *Nat. Nanotechnol.*, vol. 13, no. 12, pp. 1137–1142, Oct. 2018

[159] K. Parto, S. I. Azzam, K. Banerjee, and G. Moody, "Defect and strain engineering of monolayer WSe_2 enables site-controlled single-photon emission up to 150 K," *Nat.*

Commun. 2021 121, vol. 12, no. 1, pp. 1–8, Jun. 2021

[160] K. Wang, Z. Gao, W. Zhang, Y. Yan, H. Song, X. Lin, Z. Zhou, H. Meng, A. Xia, J. Yao, and Y. S. Zhao, "Exciton funneling in light-harvesting organic semiconductor microcrystals for wavelength-tunable lasers," *Sci. Adv.*, vol. 5, no. 6, pp. 2953–2967, Jun. 2019

[161] P. Qi, Y. Dai, Y. Luo, G. Tao, W. Qian, Z. Zhang, Z. Zhang, T. H. Zhang, L. Lin, W. Liu, and Z. Fang, "Molding 2D Exciton Flux toward Room Temperature Excitonic Devices," *Adv. Mater. Technol.*, p. 2200032, 2022

[162] M. G. Harats and K. I. Bolotin, "Limits of funneling efficiency in non-uniformly strained 2D semiconductors," *2D Mater.*, vol. 8, no. 1, p. 015010, Jan. 2021

[163] Y. Jiang, S. Chen, W. Zheng, B. Zheng, and A. Pan, "Interlayer exciton formation, relaxation, and transport in TMD van der Waals heterostructures," *Light Sci. Appl.*, vol. 10, no. 1, pp. 2047–7538, Dec. 2021

[164] J. Kim, C. Jin, B. Chen, H. Cai, T. Zhao, P. Lee, S. Kahn, K. Watanabe, T. Taniguchi, S. Tongay, M. F. Crommie, and F. Wang, "Observation of ultralong valley lifetime in WSe_2/MoS_2 heterostructures," *Sci. Adv.*, vol. 3, no. 7, Jul. 2017

[165] P. Hess, "Surface acoustic waves in materials science," *Phys. Today*, vol. 55, no. 3, pp. 42–47, 2002

[166] D. Morgan, *Surface Acoustic Wave Filters*. Elsevier Ltd, 2007.

[167] J. Rudolph, R. Hey, and P. V. Santos, "Exciton transport by surface acoustic waves," *Superlattices Microstruct.*, vol. 41, no. 5–6, pp. 293–296, 2007

[168] A. Zrenner, P. Leeb, J. Schäfer, G. Böhm, G. Weimann, J. M. Worlock, L. T. Florez, and J. P. Harbison, "Indirect excitons in coupled quantum well structures," *Surf. Sci.*, vol. 263, no. 1–3, pp. 496–501, Feb. 1992

[169] J. E. Golub, K. Kash, J. P. Harbison, and L. T. Florez, "Long-lived spatially indirect excitons in coupled $GaAs/Al_xGa_{1-x}As$ quantum wells," *Phys. Rev. B*, vol. 41, no. 12, p. 8564, Apr. 1990

[170] A. Gärtner, A. W. Holleitner, J. P. Kotthaus, and D. Schuh, "Drift mobility of long-living excitons in coupled GaAs quantum wells," *Appl. Phys. Lett.*, vol. 89, no. 5, p. 52108, Aug. 2006

[171] K. Datta, Z. Lyu, Z. Li, T. Taniguchi, K. Watanabe, and P. B. Deotare, "Spatiotemporally controlled room-temperature exciton transport under dynamic strain," *Nat. Photonics*, vol. 16, no. 3, pp. 242–247, Feb. 2022

[172] K. Datta and P. B. Deotare, "Optical Determination of Young's Modulus of Nanoscale Organic Semiconductor Thin Films for Flexible Devices," *ACS Appl. Nano Mater.*, vol. 3,

no. 2, pp. 992–1001, 2020

[173] K. Datta and P. B. Deotare, “Strain sensitivity of dielectric polarization to doping in a host: guest medium,” *Opt. Mater. Express, Vol. 10, Issue 12, pp. 3021-3029*, vol. 10, no. 12, pp. 3021–3029, Dec. 2020

[174] M. Fahlman, S. Fabiano, V. Gueskine, D. Simon, M. Berggren, and X. Crispin, “Interfaces in organic electronics,” *Nat. Rev. Mater.*, vol. 4, no. 10, pp. 627–650, Jul. 2019

[175] Y. Kondo, K. Yoshiura, S. Kitera, H. Nishi, S. Oda, H. Gotoh, Y. Sasada, M. Yanai, and T. Hatakeyama, “Narrowband deep-blue organic light-emitting diode featuring an organoboron-based emitter,” *Nat. Photonics*, pp. 1–5, Jul. 2019

[176] T. Dogan, R. Verbeek, A. J. Kronemeijer, P. A. Bobbert, G. H. Gelinck, and W. G. van der Wiel, “Short-Channel Vertical Organic Field-Effect Transistors with High On/Off Ratios,” *Adv. Electron. Mater.*, vol. 5, no. 5, 2019

[177] L. Meng, Y. Zhang, X. Wan, C. Li, X. Zhang, Y. Wang, X. Ke, Z. Xiao, L. Ding, R. Xia, H. L. Yip, Y. Cao, and Y. Chen, “Organic and solution-processed tandem solar cells with 17.3% efficiency,” *Science (80-.).*, vol. 361, no. 6407, pp. 1094–1098, 2018

[178] S.-S. Yoon and D.-Y. Khang, “High Efficiency (>17%) Si-Organic Hybrid Solar Cells by Simultaneous Structural, Electrical, and Interfacial Engineering via Low-Temperature Processes,” *Adv. Energy Mater.*, vol. 8, no. 9, p. 1702655, Mar. 2018

[179] T. Sekitani and T. Someya, “Stretchable, large-area organic electronics,” *Advanced Materials*, vol. 22, no. 20. pp. 2228–2246, 2010.

[180] Y. Qian, X. Zhang, L. Xie, D. Qi, B. K. Chandran, X. Chen, and W. Huang, “Stretchable Organic Semiconductor Devices,” *Adv. Mater.*, vol. 28, no. 42, pp. 9243–9265, 2016

[181] S. E. Root, S. Savagatrup, A. D. Printz, D. Rodriquez, and D. J. Lipomi, “Mechanical Properties of Organic Semiconductors for Stretchable, Highly Flexible, and Mechanically Robust Electronics,” *Chem. Rev.*, vol. 117, no. 9, pp. 6467–6499, 2017

[182] C. M. Stafford, B. D. Vogt, C. Harrison, D. Julthongpiput, and R. Huang, “Elastic moduli of ultrathin amorphous polymer films,” *Macromolecules*, vol. 39, no. 15, pp. 5095–5099, 2006

[183] D. Rodriquez, S. Savagatrup, E. Valle, C. M. Proctor, C. McDowell, G. C. Bazan, T. Q. Nguyen, and D. J. Lipomi, “Mechanical Properties of Solution-Processed Small-Molecule Semiconductor Films,” *ACS Appl. Mater. Interfaces*, vol. 8, no. 18, pp. 11649–11657, 2016

[184] J. Y. Chung, A. J. Nolte, and C. M. Stafford, “Surface wrinkling: A versatile platform for measuring thin-film properties,” *Adv. Mater.*, vol. 23, no. 3, pp. 349–368, 2011

[185] C. M. Stafford, C. Harrison, K. L. Beers, A. Karim, E. J. Amis, M. R. Vanlandingham, H.

C. Kim, W. Volksen, R. D. Miller, and E. E. Simonyi, “A buckling-based metrology for measuring the elastic moduli of polymeric thin films,” *Nat. Mater.*, vol. 3, no. 8, pp. 545–550, 2004

[186] N. Bakken, J. M. Torres, J. Li, and B. D. Vogt, “Thickness dependent modulus of vacuum deposited organic molecular glasses for organic electronics applications,” *Soft Matter*, vol. 7, no. 16, pp. 7269–7273, 2011

[187] J. M. Torres, N. Bakken, C. M. Stafford, J. Li, and B. D. Vogt, “Thickness dependence of the elastic modulus of tris(8-hydroxyquinolinato) aluminium,” *Soft Matter*, vol. 6, no. 22, pp. 5783–5788, Nov. 2010

[188] C. J. Chiang, S. Bull, C. Winscom, and A. Monkman, “A nano-indentation study of the reduced elastic modulus of Alq_3 and NPB thin-film used in OLED devices,” *Org. Electron. physics, Mater. Appl.*, vol. 11, no. 3, pp. 450–455, 2010

[189] M. D. Halls, J. M. Sanders, H. S. Kwak, T. J. Mustard, and A. R. Browning, “Atomistic simulations of mechanical and thermophysical properties of OLED materials,” no. September 2018, p. 87, 2018

[190] D. Schneider, T. Schwarz, and B. Schultrich, “Determination of elastic modulus and thickness of surface layers by ultrasonic surface waves,” *Thin Solid Films*, vol. 219, no. 1–2, pp. 92–102, Oct. 1992

[191] D. C. Hurley, V. K. Tewary, and A. J. Richards, “Surface acoustic wave methods to determine the anisotropic elastic properties of thin films,” *Meas. Sci. Technol.*, vol. 12, no. 9, pp. 1486–1494, 2001

[192] H. Ogi, N. Nakamura, and M. Hirao, “Picosecond ultrasound spectroscopy for studying elastic modulus of thin films: a review,” *Nondestruct. Test. Eval.*, vol. 26, no. 3–4, pp. 267–280, Sep. 2011

[193] B. C. Daly, S. T. Bailey, R. Sooryakumar, and S. W. King, “Noncontact optical metrologies for Young’s modulus measurements of nanoporous low-k dielectric thin films,” *J. Nanophotonics*, vol. 7, no. 1, p. 073094, Apr. 2013

[194] L. L. Chapelon, J. Vitiello, D. Neira, J. Torres, J. C. Royer, D. Barbier, F. Naudin, G. Tas, P. Mukundhan, and J. Clerico, “Measuring the Young’s modulus of ultralow-k materials with the non destructive picosecond ultrasonic method,” *Microelectron. Eng.*, vol. 83, no. 11–12, pp. 2346–2350, Nov. 2006

[195] J. A. Forrest, K. Dalnoki-Veress, and J. R. Dutcher, “Brillouin light scattering studies of the mechanical properties of thin freely standing polystyrene films,” *Phys. Rev. E - Stat. Physics, Plasmas, Fluids, Relat. Interdiscip. Top.*, vol. 58, no. 5, pp. 6109–6114, 1998

[196] S. Bailey, E. Mays, D. J. Michalak, R. Chebiam, S. King, and R. Sooryakumar, “Mechanical properties of high porosity low-k dielectric nano-films determined by Brillouin light scattering,” *J. Phys. D. Appl. Phys.*, vol. 46, no. 4, Jan. 2013

[197] G. Carlotti, N. Chérault, N. Casanova, C. Goldberg, and G. Socino, "Elastic constants of low-k and barrier dielectric films measured by Brillouin light scattering," *Thin Solid Films*, vol. 493, no. 1–2, pp. 175–178, Dec. 2005

[198] K. P. Mogilnikov and M. R. Baklanov, "Determination of Young's modulus of porous low-k films by ellipsometric porosimetry," *Electrochem. Solid-State Lett.*, vol. 5, no. 12, Dec. 2002

[199] C. Boissiere, D. Grosso, S. Lepoutre, L. Nicole, A. B. Bruneau, and C. Sanchez, "Porosity and mechanical properties of mesoporous thin films assessed by environmental ellipsometric porosimetry," *Langmuir*, vol. 21, no. 26, pp. 12362–12371, Dec. 2005

[200] J. Bae, T. Ouchi, and R. C. Hayward, "Measuring the Elastic Modulus of Thin Polymer Sheets by Elastocapillary Bending," *ACS Appl. Mater. Interfaces*, vol. 7, no. 27, pp. 14734–14742, Jul. 2015

[201] C. W. Tang and S. A. Vanslyke, "Organic electroluminescent diodes," *Appl. Phys. Lett.*, vol. 51, no. 12, pp. 913–915, 1987

[202] L. S. Hung and C. H. Chen, "Recent progress of molecular organic electroluminescent materials and devices," *Materials Science and Engineering R: Reports*, vol. 39, no. 5–6. Elsevier Ltd, pp. 143–222, Dec. 01, 2002.

[203] V. G. Kozlov, V. Bulovic, P. E. Burrows, M. Baldo, V. B. Khalfin, G. Parthasarathy, S. R. Forrest, Y. You, and M. E. Thompson, "Study of lasing action based on Förster energy transfer in optically pumped organic semiconductor thin films," *J. Appl. Phys.*, vol. 84, no. 8, pp. 4096–4108, Oct. 1998

[204] T. Mori and T. Mizutani, "Application of energy transfer model to partially DCM-doped Alq_3 light-emitting diode," *Polym. Adv. Technol.*, vol. 8, no. 7, pp. 471–476, Jul. 1997

[205] N. Balar and B. T. O'Connor, "Correlating Crack Onset Strain and Cohesive Fracture Energy in Polymer Semiconductor Films," *Macromolecules*, vol. 50, no. 21, pp. 8611–8618, 2017

[206] D. Tank, H. H. Lee, and D. Y. Khang, "Elastic moduli of organic electronic materials by the buckling method," *Macromolecules*, vol. 42, no. 18, pp. 7079–7083, 2009

[207] H. F. Winters and J. W. Coburn, "The etching of silicon with XeF_2 vapor," *Appl. Phys. Lett.*, vol. 34, no. 1, pp. 70–73, 1979

[208] C. W. Chang, Y. T. Kao, and E. W. G. Diau, "Fluorescence lifetime and nonradiative relaxation dynamics of DCM in nonpolar solvent," *Chem. Phys. Lett.*, vol. 374, no. 1–2, pp. 110–118, 2003

[209] B. Beyer and K. Leo, "Efficiency increase of organic solar cells with emissive light-in-coupling layers," *J. Mater. Chem. C*, vol. 3, no. 41, pp. 10830–10836, Oct. 2015

[210] C. W. Tang, S. A. Vanslyke, and C. H. Chen, “Electroluminescence of doped organic thin films,” *J. Appl. Phys.*, vol. 65, no. 9, p. 3610, Jun. 1998

[211] J. R. Lakowicz, *Principles of fluorescence spectroscopy*. Springer, 2006.

[212] E. Lippert, “Dipolmoment und Elektronenstruktur von angeregten Molekülen,” *Zeitschrift fur Naturforsch. - Sect. A J. Phys. Sci.*, vol. 10, no. 7, pp. 541–545, 1955

[213] N. Mataga, Y. Kaifu, and M. Koizumi, “Solvent Effects upon Fluorescence Spectra and the Dipolemoments of Excited Molecules,” *Bull. Chem. Soc. Jpn.*, vol. 29, no. 4, pp. 465–470, 1956

[214] L. Onsager, “Electric Moments of Molecules in Liquids,” *J. Am. Chem. Soc.*, vol. 58, no. 8, pp. 1486–1493, 1936

[215] A. P. Green, K. T. Butler, and A. R. Buckley, “Tuning of the emission energy of fluorophores using solid state solvation for efficient luminescent solar concentrators,” *Appl. Phys. Lett.*, vol. 102, no. 13, 2013

[216] M. Meyer and J. C. Mialocq, “Ground state and singlet excited state of laser dye DCM: Dipole moments and solvent induced spectral shifts,” *Opt. Commun.*, vol. 64, no. 3, pp. 264–268, 1987

[217] A. Luridiana, G. Pretta, D. Chiriu, C. M. Carbonaro, R. Corpino, F. Secci, A. Frongia, L. Stagi, and P. C. Ricci, “A facile strategy for new organic white LED hybrid devices: Design, features and engineering,” *RSC Adv.*, 2016

[218] P. Van Rysselberghe, “Remarks concerning the clausius-mossotti law,” *J. Phys. Chem.*, vol. 36, no. 4, pp. 1152–1155, 1932

[219] S. D. Senturia, *Microsystem Design*. Springer, 2005.

[220] R. Farchioni and G. Grosso, *Organic Electronic Materials: Conjugted Polymers and Low Molecular Weight Electronic Solids.* Springer, 2001.

[221] “COMSOL Multiphysics® Modeling Software.” https://www.comsol.com/

[222] D.-Y. Khang, J. A. Rogers, and H. H. Lee, “Mechanical Buckling: Mechanics, Metrology, and Stretchable Electronics,” *Adv. Funct. Mater.*, vol. 19, no. 10, pp. 1526–1536, May 2009

[223] K. Datta, Z. Li, Z. Lyu, and P. B. Deotare, “Piezoelectric Modulation of Excitonic Properties in Monolayer WSe_2 under Strong Dielectric Screening,” *ACS Nano*, vol. 15, no. 7, pp. 12334–12341, Jul. 2021

[224] S. Manzeli, D. Ovchinnikov, D. Pasquier, O. V. Yazyev, and A. Kis, “2D transition metal dichalcogenides,” *Nat. Rev. Mater.*, vol. 2, no. 8, pp. 1–15, Jun. 2017

[225] D. Jariwala, V. K. Sangwan, L. J. Lauhon, T. J. Marks, and M. C. Hersam, "Emerging device applications for semiconducting two-dimensional transition metal dichalcogenides," *ACS Nano*, vol. 8, no. 2, pp. 1102–1120, Feb. 2014

[226] C. Schneider, M. M. Glazov, T. Korn, S. Höfling, and B. Urbaszek, "Two-dimensional semiconductors in the regime of strong light-matter coupling," *Nat. Commun.*, vol. 9, no. 1, pp. 1–9, Dec. 2018

[227] A. Chernikov, T. C. Berkelbach, H. M. Hill, A. Rigosi, Y. Li, O. B. Aslan, D. R. Reichman, M. S. Hybertsen, and T. F. Heinz, "Exciton binding energy and nonhydrogenic Rydberg series in monolayer WS_2," *Phys. Rev. Lett.*, vol. 113, no. 7, p. 076802, Aug. 2014

[228] J. S. Ross, P. Klement, A. M. Jones, N. J. Ghimire, J. Yan, D. G. Mandrus, T. Taniguchi, K. Watanabe, K. Kitamura, W. Yao, D. H. Cobden, and X. Xu, "Electrically tunable excitonic light-emitting diodes based on monolayer WSe_2 *p–n* junctions," *Nat. Nanotechnol.*, vol. 9, no. 4, pp. 268–272, 2014

[229] B. W. H. Baugher, H. O. H. Churchill, Y. Yang, and P. Jarillo-Herrero, "Optoelectronic devices based on electrically tunable *p-n* diodes in a monolayer dichalcogenide," *Nat. Nanotechnol.*, vol. 9, no. 4, pp. 262–267, Mar. 2014

[230] T. Sogawa, H. Sanada, H. Gotoh, H. Yamaguchi, and P. V. Santos, "Dynamic control of photoluminescence polarization properties in GaAs/AlAs quantum wells by surface acoustic waves," *Phys. Rev. B - Condens. Matter Mater. Phys.*, vol. 86, no. 3, p. 035311, Jul. 2012

[231] F. Alsina, P. V. Santos, R. Hey, A. García-Cristóbal, and A. Cantarero, "Dynamic carrier distribution in quantum wells modulated by surface acoustic waves," *Phys. Rev. B - Condens. Matter Mater. Phys.*, vol. 64, no. 4, pp. 1–4, 2001

[232] J. B. Kinzel, D. Rudolph, M. Bichler, G. Abstreiter, J. J. Finley, G. Koblmüller, A. Wixforth, and H. J. Krenner, "Directional and dynamic modulation of the optical emission of an individual GaAs nanowire using surface acoustic waves," *Nano Lett.*, vol. 11, no. 4, pp. 1512–1517, Apr. 2011

[233] A. Hernández-Mínguez, M. Möller, S. Breuer, C. Pfüller, C. Somaschini, S. Lazić, O. Brandt, A. García-Cristóbal, M. M. De Lima, A. Cantarero, L. Geelhaar, H. Riechert, and P. V. Santos, "Acoustically driven photon antibunching in nanowires," *Nano Lett.*, vol. 12, no. 1, pp. 252–258, Jan. 2012

[234] S. Lazić, E. Chernysheva, Gačević, H. P. Van Der Meulen, E. Calleja, and J. M. Calleja Pardo, "Dynamic control of the optical emission from GaN/InGaN nanowire quantum dots by surface acoustic waves," *AIP Adv.*, vol. 5, no. 9, p. 97217, Sep. 2015

[235] J. Pustiowski, K. Müller, M. Bichler, G. Koblmüller, J. J. Finley, A. Wixforth, and H. J. Krenner, "Independent dynamic acousto-mechanical and electrostatic control of individual quantum dots in a $LiNbO_3$-GaAs hybrid," *Appl. Phys. Lett.*, vol. 106, no. 1, p. 13107, Jan. 2015

[236] A. R. Rezk, B. Carey, A. F. Chrimes, D. W. M. Lau, B. C. Gibson, C. Zheng, M. S. Fuhrer, L. Y. Yeo, and K. Kalantar-Zadeh, "Acoustically-Driven Trion and Exciton Modulation in Piezoelectric Two-Dimensional MoS_2," *Nano Lett.*, vol. 16, no. 2, pp. 849–855, 2016

[237] A. R. Rezk, S. Walia, R. Ramanathan, H. Nili, J. Z. Ou, V. Bansal, J. R. Friend, M. Bhaskaran, L. Y. Yeo, and S. Sriram, "Acoustic-Excitonic Coupling for Dynamic Photoluminescence Manipulation of Quasi-2D MoS_2 Nanoflakes," *Adv. Opt. Mater.*, vol. 3, no. 7, pp. 888–894, Jul. 2015

[238] S. Lazić, A. Espinha, S. Pinilla Yanguas, C. Gibaja, F. Zamora, P. Ares, M. Chhowalla, W. S. Paz, J. J. P. Burgos, A. Hernández-Mínguez, P. V. Santos, and H. P. van der Meulen, "Dynamically tuned non-classical light emission from atomic defects in hexagonal boron nitride," *Commun. Phys.*, vol. 2, no. 1, pp. 1–8, Dec. 2019

[239] E. Preciado, F. J. R. Schülein, A. E. Nguyen, D. Barroso, M. Isarraraz, G. Von Son, I. H. Lu, W. Michailow, B. Möller, V. Klee, J. Mann, A. Wixforth, L. Bartels, and H. J. Krenner, "Scalable fabrication of a hybrid field-effect and acousto-electric device by direct growth of monolayer MoS_2/$LiNbO_3$," *Nat. Commun.*, vol. 6, no. 1, pp. 1–8, Oct. 2015

[240] S. Zheng, E. Wu, Z. Feng, R. Zhang, Y. Xie, Y. Yu, R. Zhang, Q. Li, J. Liu, W. Pang, H. Zhang, and D. Zhang, "Acoustically enhanced photodetection by a black phosphorus-MoS_2 van der Waals heterojunction *p-n* diode," *Nanoscale*, vol. 10, no. 21, pp. 10148–10153, Jun. 2018

[241] L. Bandhu, L. M. Lawton, and G. R. Nash, "Macroscopic acoustoelectric charge transport in graphene," *Appl. Phys. Lett.*, vol. 103, no. 13, p. 133101, Sep. 2013

[242] V. Miseikis, J. E. Cunningham, K. Saeed, R. O'Rorke, and A. G. Davies, "Acoustically induced current flow in graphene," *Appl. Phys. Lett.*, vol. 100, no. 13, p. 133105, Mar. 2012

[243] S. Zheng, H. Zhang, Z. Feng, Y. Yu, R. Zhang, C. Sun, J. Liu, X. Duan, W. Pang, and D. Zhang, "Acoustic charge transport induced by the surface acoustic wave in chemical doped graphene," *Appl. Phys. Lett.*, vol. 109, no. 18, p. 183110, Oct. 2016

[244] T. Poole and G. R. Nash, "Acoustoelectric Current in Graphene Nanoribbons," *Sci. Rep.*, vol. 7, no. 1, pp. 1–9, Dec. 2017

[245] M. Yokoi, S. Fujiwara, T. Kawamura, T. Arakawa, K. Aoyama, H. Fukuyama, K. Kobayashi, and Y. Niimi, "Negative resistance state in superconducting $NbSe_2$ induced by surface acoustic waves," *Sci. Adv.*, vol. 6, no. 34, p. eaba1377, Aug. 2020

[246] L. S. R. Cavalcante, D. R. Da Costa, G. A. Farias, D. R. Reichman, and A. Chaves, "Stark shift of excitons and trions in two-dimensional materials," *Phys. Rev. B*, vol. 98, no. 24, p. 245309, Dec. 2018

[247] T. G. Pedersen, “Exciton Stark shift and electroabsorption in monolayer transition-metal dichalcogenides,” *Phys. Rev. B*, vol. 94, no. 12, p. 125424, Sep. 2016

[248] M. Massicotte, F. Vialla, P. Schmidt, M. B. Lundeberg, S. Latini, S. Haastrup, M. Danovich, D. Davydovskaya, K. Watanabe, T. Taniguchi, V. I. Fal’ko, K. S. Thygesen, T. G. Pedersen, and F. H. L. Koppens, “Dissociation of two-dimensional excitons in monolayer WSe_2,” *Nat. Commun.*, vol. 9, no. 1, pp. 1–7, Dec. 2018

[249] J. Klein, J. Wierzbowski, A. Regler, J. Becker, F. Heimbach, K. Müller, M. Kaniber, and J. J. Finley, “Stark Effect Spectroscopy of Mono- and Few-Layer MoS_2,” *Nano Lett.*, vol. 16, no. 3, pp. 1554–1559, Mar. 2016

[250] J. G. Roch, N. Leisgang, G. Froehlicher, P. Makk, K. Watanabe, T. Taniguchi, C. Schönenberger, and R. J. Warburton, “Quantum-Confined Stark Effect in a MoS_2 Monolayer van der Waals Heterostructure,” *Nano Lett.*, vol. 18, no. 2, pp. 1070–1074, Feb. 2018

[251] I. Verzhbitskiy, D. Vella, K. Watanabe, T. Taniguchi, and G. Eda, “Suppressed Out-of-Plane Polarizability of Free Excitons in Monolayer WSe_2,” *ACS Nano*, vol. 13, no. 3, pp. 3218–3224, Mar. 2019

[252] C. Rocke, S. Zimmermann, A. Wixforth, J. P. Kotthaus, G. Böhm, and G. Weimann, “Acoustically driven storage of light in a quantum well,” *Phys. Rev. Lett.*, vol. 78, no. 21, pp. 4099–4102, 1997

[253] D. Morgan, *Surface Acoustic Wave Filters*. Cambridge, Massachusetts: Elsevier Ltd, 2007.

[254] T. C. Berkelbach, M. S. Hybertsen, and D. R. Reichman, “Theory of neutral and charged excitons in monolayer transition metal dichalcogenides,” *Phys. Rev. B - Condens. Matter Mater. Phys.*, vol. 88, no. 4, p. 045318, Jul. 2013

[255] Y. Lin, X. Ling, L. Yu, S. Huang, A. L. Hsu, Y. H. Lee, J. Kong, M. S. Dresselhaus, and T. Palacios, “Dielectric screening of excitons and trions in single-layer MoS_2,” *Nano Lett.*, vol. 14, no. 10, pp. 5569–5576, Oct. 2014

[256] A. V. Stier, N. P. Wilson, G. Clark, X. Xu, and S. A. Crooker, “Probing the Influence of Dielectric Environment on Excitons in Monolayer WSe_2: Insight from High Magnetic Fields,” *Nano Lett.*, vol. 16, no. 11, pp. 7054–7060, Nov. 2016

[257] D. Scolfaro, M. Finamor, L. O. Trinchão, B. L. T. Rosa, A. Chaves, P. V. Santos, F. Iikawa, and O. D. D. Couto, “Acoustically Driven Stark Effect in Transition Metal Dichalcogenide Monolayers,” *ACS Nano*, vol. 15, no. 9, pp. 15371–15380, Sep. 2021

[258] G. Aivazian, Z. Gong, A. M. Jones, R. L. Chu, J. Yan, D. G. Mandrus, C. Zhang, D. Cobden, W. Yao, and X. Xu, “Magnetic control of valley pseudospin in monolayer WSe_2,” *Nat. Phys.*, vol. 11, no. 2, pp. 148–152, Jan. 2015

[259] A. Arora, M. Koperski, K. Nogajewski, J. Marcus, C. Faugeras, and M. Potemski, "Excitonic resonances in thin films of WSe_2: From monolayer to bulk material," *Nanoscale*, vol. 7, no. 23, pp. 10421–10429, Jun. 2015

[260] J. Huang, T. B. Hoang, and M. H. Mikkelsen, "Probing the origin of excitonic states in monolayer WSe_2," *Sci. Rep.*, vol. 6, no. 1, pp. 1–7, Mar. 2016

[261] Y. You, X. X. Zhang, T. C. Berkelbach, M. S. Hybertsen, D. R. Reichman, and T. F. Heinz, "Observation of biexcitons in monolayer WSe_2," *Nat. Phys.*, vol. 11, no. 6, pp. 477–481, Jun. 2015

[262] M. He, P. Rivera, D. Van Tuan, N. P. Wilson, M. Yang, T. Taniguchi, K. Watanabe, J. Yan, D. G. Mandrus, H. Yu, H. Dery, W. Yao, and X. Xu, "Valley phonons and exciton complexes in a monolayer semiconductor," *Nat. Commun.*, vol. 11, no. 1, pp. 1–7, Dec. 2020

[263] P. Rivera *et al.*, "Intrinsic donor-bound excitons in ultraclean monolayer semiconductors," *Nat. Commun.*, vol. 12, no. 1, pp. 1–8, Dec. 2021

[264] K. Wei, Y. Liu, H. Yang, X. Cheng, and T. Jiang, "Large range modification of exciton species in monolayer WS_2," *Appl. Opt.*, vol. 55, no. 23, p. 6251, Aug. 2016

[265] S. Mouri, Y. Miyauchi, and K. Matsuda, "Tunable photoluminescence of monolayer MoS_2 via chemical doping," *Nano Lett.*, vol. 13, no. 12, pp. 5944–5948, Dec. 2013

[266] A. Singh, G. Moody, K. Tran, M. E. Scott, V. Overbeck, G. Berghäuser, J. Schaibley, E. J. Seifert, D. Pleskot, N. M. Gabor, J. Yan, D. G. Mandrus, M. Richter, E. Malic, X. Xu, and X. Li, "Trion formation dynamics in monolayer transition metal dichalcogenides," *Phys. Rev. B*, vol. 93, no. 4, p. 041401, Jan. 2016

[267] J. Siviniant, D. Scalbert, A. V. Kavokin, D. Coquillat, and J. P. Lascaray, "Chemical equilibrium between excitons, electrons, and negatively charged excitons in semiconductor quantum wells," *Phys. Rev. B - Condens. Matter Mater. Phys.*, vol. 59, no. 3, pp. 1602–1604, Jan. 1999

[268] K. Kheng, R. T. Cox, M. Y. D'Aubigné, F. Bassani, K. Saminadayar, and S. Tatarenko, "Observation of negatively charged excitons X^- in semiconductor quantum wells," *Phys. Rev. Lett.*, vol. 71, no. 11, pp. 1752–1755, Sep. 1993

[269] P. V. Santos, M. Ramsteiner, and F. Jungnickel, "Spatially resolved photoluminescence in GaAs surface acoustic wave structures," *Appl. Phys. Lett.*, vol. 72, no. 17, pp. 2099–2101, Jun. 1998

[270] D. A. Fuhrmann, A. Wixforth, A. Curran, J. K. Morrod, K. A. Prior, R. J. Warburton, and J. Ebbecke, "Surface acoustic wave mediated exciton dissociation in a ZnCdSe/ $LiNbO_3$ hybrid," *Appl. Phys. Lett.*, vol. 94, no. 19, p. 193505, May 2009

[271] T. Huang, P. Han, X. Wang, J. Ye, W. Sun, S. Feng, and Y. Zhang, "Theoretical study on

dynamic acoustic modulation of free carriers, excitons, and trions in 2D MoS_2 flake," *J. Phys. D. Appl. Phys.*, vol. 50, no. 11, p. 114005, Feb. 2017

[272] P. V. Santos, F. Alsina, J. A. H. Stotz, R. Hey, S. Eshlaghi, and A. D. Wieck, "Band mixing and ambipolar transport by surface acoustic waves in GaAs quantum wells," *Phys. Rev. B - Condens. Matter Mater. Phys.*, vol. 69, no. 15, p. 155318, Apr. 2004

[273] A. L. Ivanov and P. B. Littlewood, "Acoustically induced stark effect for excitons in intrinsic semiconductors," *Phys. Rev. Lett.*, vol. 87, no. 13, p. 136403, Sep. 2001

[274] W. C. H. Choy, E. H. Li, and B. L. Weiss, "Electro-optic and electro-absorptive modulations of AlGaAs/GaAs quantum well using surface acoustic wave," *J. Appl. Phys.*, vol. 83, no. 2, pp. 858–866, Jan. 1998

[275] Z. Sun, J. Beaumariage, K. Xu, J. Liang, S. Hou, S. R. Forrest, S. K. Fullerton-Shirey, and D. W. Snoke, "Electric-field-induced optical hysteresis in single-layer WSe_2," *Appl. Phys. Lett.*, vol. 115, no. 16, p. 161103, Oct. 2019

[276] A. Chernikov, A. M. Van Der Zande, H. M. Hill, A. F. Rigosi, A. Velauthapillai, J. Hone, and T. F. Heinz, "Electrical Tuning of Exciton Binding Energies in Monolayer WS_2," *Phys. Rev. Lett.*, vol. 115, no. 12, p. 126802, Sep. 2015

[277] R. Schmidt, I. Niehues, R. Schneider, M. Drüppel, T. Deilmann, M. Rohlfing, S. M. De Vasconcellos, A. Castellanos-Gomez, and R. Bratschitsch, "Reversible uniaxial strain tuning in atomically thin WSe_2," *2D Mater.*, vol. 3, no. 2, p. 021011, Jun. 2016

[278] D. A. B. Miller, D. S. Chemla, T. C. Damen, A. C. Gossard, W. Wiegmann, T. H. Wood, and C. A. Burrus, "Electric field dependence of optical absorption near the band gap of quantum-well structures," *Phys. Rev. B*, vol. 32, no. 2, pp. 1043–1060, Jul. 1985

[279] T. Yan, X. Qiao, X. Liu, P. Tan, and X. Zhang, "Photoluminescence properties and exciton dynamics in monolayer WSe_2," *Appl. Phys. Lett.*, vol. 105, no. 10, p. 101901, Sep. 2014

[280] S. Mouri, Y. Miyauchi, M. Toh, W. Zhao, G. Eda, and K. Matsuda, "Nonlinear photoluminescence in atomically thin layered WSe_2 arising from diffusion-assisted exciton-exciton annihilation," *Phys. Rev. B - Condens. Matter Mater. Phys.*, vol. 90, no. 15, pp. 1–5, 2014

[281] S. Sim, J. Park, J. G. Song, C. In, Y. S. Lee, H. Kim, and H. Choi, "Exciton dynamics in atomically thin MoS_2: Interexcitonic interaction and broadening kinetics," *Phys. Rev. B - Condens. Matter Mater. Phys.*, vol. 88, no. 7, p. 075434, Aug. 2013

[282] H. Liu, C. Wang, D. Liu, and J. Luo, "Neutral and defect-induced exciton annihilation in defective monolayer WS_2," *Nanoscale*, vol. 11, no. 16, pp. 7913–7920, Apr. 2019

[283] A. García-Cristóbal, A. Cantarero, F. Alsina, and P. V. Santos, "Spatiotemporal carrier dynamics in quantum wells under surface acoustic waves," *Phys. Rev. B - Condens.*

Matter Mater. Phys., vol. 69, no. 20, pp. 1–13, 2004

[284] T. Tan, X. Jiang, C. Wang, B. Yao, H. Zhang, T. Tan, B. C. Yao, X. T. Jiang, C. Wang, and H. Zhang, "2D Material Optoelectronics for Information Functional Device Applications: Status and Challenges," *Adv. Sci.*, vol. 7, no. 11, p. 2000058, Jun. 2020

[285] A. Rose, Z. Zhu, C. F. Madigan, T. M. Swager, and V. Bulović, "Sensitivity gains in chemosensing by lasing action in organic polymers," *Nat. 2005 4347035*, vol. 434, no. 7035, pp. 876–879, Apr. 2005

[286] L. V. Butov, "Excitonic devices," *Superlattices Microstruct.*, vol. 108, pp. 2–26, 2017

[287] G. Grosso, J. Graves, A. T. Hammack, A. A. High, L. V. Butov, M. Hanson, and A. C. Gossard, "Excitonic switches operating at around 100K," *Nat. Photonics*, vol. 3, no. 10, pp. 577–580, 2009

[288] L. H. Fowler-Gerace, D. J. Choksy, and L. V. Butov, "Voltage-controlled long-range propagation of indirect excitons in a van der Waals heterostructure," *Phys. Rev. B*, vol. 104, no. 16, p. 165302, Oct. 2021

[289] A. A. High, E. E. Novitskaya, L. V. Butov, M. Hanson, and A. C. Gossard, "Control of exciton fluxes in an excitonic integrated circuit," *Science (80-.).*, vol. 321, no. 5886, pp. 229–231, 2008

[290] A. Chaves *et al.*, "Bandgap engineering of two-dimensional semiconductor materials," *npj 2D Mater. Appl. 2020 41*, vol. 4, no. 1, pp. 1–21, Aug. 2020

[291] D. Unuchek, A. Ciarrocchi, A. Avsar, K. Watanabe, T. Taniguchi, and A. Kis, "Room-temperature electrical control of exciton flux in a van der Waals heterostructure," *Nature*, vol. 560, no. 7718, pp. 340–344, Aug. 2018

[292] D. Unuchek, A. Ciarrocchi, A. Avsar, Z. Sun, K. Watanabe, T. Taniguchi, and A. Kis, "Valley-polarized exciton currents in a van der Waals heterostructure," *Nat. Nanotechnol.*, vol. 14, no. 12, pp. 1104–1109, Dec. 2019

[293] P. Zhou, C. Chen, X. Wang, B. Hu, and H. San, "2-Dimentional photoconductive MoS_2 nanosheets using in surface acoustic wave resonators for ultraviolet light sensing," *Sensors Actuators A Phys.*, vol. 271, pp. 389–397, Mar. 2018

[294] R. Fandan, J. Pedrós, A. Hernández-Mínguez, F. Iikawa, P. V. Santos, A. Boscá, and F. Calle, "Dynamic Local Strain in Graphene Generated by Surface Acoustic Waves," *Nano Lett.*, vol. 20, no. 1, pp. 402–409, Jan. 2019

[295] Y. Hoshi, T. Kuroda, M. Okada, R. Moriya, S. Masubuchi, K. Watanabe, T. Taniguchi, R. Kitaura, and T. Machida, "Suppression of exciton-exciton annihilation in tungsten disulfide monolayers encapsulated by hexagonal boron nitrides," *Phys. Rev. B*, vol. 95, no. 24, p. 241403, Jun. 2017

[296] T. Hotta, S. Higuchi, A. Ueda, K. Shinokita, Y. Miyauchi, K. Matsuda, K. Ueno, T. Taniguchi, K. Watanabe, and R. Kitaura, "Exciton diffusion in a h BN-encapsulated monolayer $MoSe_2$," *Phys. Rev. B*, vol. 102, no. 11, p. 115424, Apr. 2020

[297] V. Y. Shur, "Lithium niobate and lithium tantalate-based piezoelectric materials," in *Advanced Piezoelectric Materials: Science and Technology*, Elsevier Inc., 2010, pp. 204–238.

[298] C. J. Dorow, M. W. Hasling, D. J. Choksy, J. R. Leonard, L. V. Butov, K. W. West, and L. N. Pfeiffer, "High-mobility indirect excitons in wide single quantum well," *Appl. Phys. Lett.*, vol. 113, no. 21, p. 212102, Nov. 2018

[299] A. Falin, Q. Cai, E. J. G. Santos, D. Scullion, D. Qian, R. Zhang, Z. Yang, S. Huang, K. Watanabe, T. Taniguchi, M. R. Barnett, Y. Chen, R. S. Ruoff, and L. H. Li, "Mechanical properties of atomically thin boron nitride and the role of interlayer interactions," *Nat. Commun.*, vol. 8, no. 1, pp. 1–9, Jun. 2017

[300] M. Feierabend, A. Morlet, G. Berghäuser, and E. Malic, "Impact of strain on the optical fingerprint of monolayer transition-metal dichalcogenides," *Phys. Rev. B*, vol. 96, no. 4, p. 045425, Jul. 2017

[301] S. Kovalchuk, M. G. Harats, G. López-Polín, J. N. Kirchhof, K. Höflich, and K. I. Bolotin, "Neutral and charged excitons interplay in non-uniformly strain-engineered WS_2," *2D Mater.*, vol. 7, no. 3, p. 035024, Jun. 2020

[302] R. Perea-Causín, S. Brem, R. Rosati, R. Jago, M. Kulig, J. D. Ziegler, J. Zipfel, A. Chernikov, and E. Malic, "Exciton Propagation and Halo Formation in Two-Dimensional Materials," *Nano Lett.*, vol. 19, no. 10, pp. 7317–7323, Oct. 2019

[303] Y. Li, A. Chernikov, X. Zhang, A. Rigosi, H. M. Hill, A. M. Van Der Zande, D. A. Chenet, E. M. Shih, J. Hone, and T. F. Heinz, "Measurement of the optical dielectric function of monolayer transition-metal dichalcogenides: MoS_2, $MoSe_2$, WS_2, and WSe_2," *Phys. Rev. B - Condens. Matter Mater. Phys.*, vol. 90, no. 20, p. 205422, Nov. 2014

[304] L. Yuan, T. Wang, T. Zhu, M. Zhou, and L. Huang, "Exciton Dynamics, Transport, and Annihilation in Atomically Thin Two-Dimensional Semiconductors," *Journal of Physical Chemistry Letters*, vol. 8, no. 14. American Chemical Society, pp. 3371–3379, Jul. 20, 2017.

[305] D. F. Cordovilla Leon, Z. Li, S. W. Jang, and P. B. Deotare, "Hot exciton transport in WSe_2 monolayers," *Phys. Rev. B*, vol. 100, no. 24, p. 241401, Dec. 2019

[306] Y. Song and H. Dery, "Transport theory of monolayer transition-metal dichalcogenides through symmetry," *Phys. Rev. Lett.*, vol. 111, no. 2, p. 026601, Jul. 2013

[307] M. M. Glazov, "Phonon wind and drag of excitons in monolayer semiconductors," *Phys. Rev. B*, vol. 100, no. 4, p. 045426, Jul. 2019

[308] Y. Yu, Y. Yu, G. Li, A. A. Puretzky, D. B. Geohegan, and L. Cao, "Giant enhancement of exciton diffusivity in two-dimensional semiconductors," *Sci. Adv.*, vol. 6, no. 51, pp. 4823–4841, Dec. 2020

[309] L. Yuan and L. Huang, "Exciton dynamics and annihilation in WS_2 2D semiconductors," *Nanoscale*, vol. 7, no. 16, pp. 7402–7408, Apr. 2015

[310] Y. Yu, A. W. Bataller, R. Younts, Y. Yu, G. Li, A. A. Puretzky, D. B. Geohegan, K. Gundogdu, and L. Cao, "Room-Temerature Electron-Hole Liquid in Monolayer MoS_2," *ACS Nano*, vol. 13, no. 9, pp. 10351–10358, May 2019

[311] J. Wang, J. Ardelean, Y. Bai, A. Steinhoff, M. Florian, F. Jahnke, X. Xu, M. Kira, J. Hone, and X. Y. Zhu, "Optical generation of high carrier densities in 2D semiconductor heterobilayers," *Sci. Adv.*, vol. 5, no. 9, Sep. 2019

[312] S. F. Chen and Y. R. Wu, "Electronic properties of MoS_2 nanoribbon with strain using tight-binding method," *Phys. status solidi*, vol. 254, no. 2, p. 1600565, Feb. 2017

[313] S. Yu, H. D. Xiong, K. Eshun, H. Yuan, and Q. Li, "Phase transition, effective mass and carrier mobility of MoS_2 monolayer under tensile strain," *Appl. Surf. Sci.*, vol. 325, no. C, pp. 27–32, Jan. 2015

[314] J. T. Dull, Y. Wang, H. Johnson, K. Shayegan, E. Shapiro, R. D. Priestley, Y. H. Geerts, and B. P. Rand, "Thermal Properties, Molecular Structure, and Thin-Film Organic Semiconductor Crystallization," *J. Phys. Chem. C*, vol. 124, no. 49, pp. 27213–27221, Dec. 2020

[315] M. A. Fusella, F. Schreiber, K. Abbasi, J. J. Kim, A. L. Briseno, and B. P. Rand, "Homoepitaxy of Crystalline Rubrene Thin Films," *Nano Lett.*, vol. 17, no. 5, pp. 3040–3046, May 2017

[316] A. Alkauskas, C. A. Meriles, C. Cohen, H. Jayakumar, M. Doherty, M. Dollar, N. V. Proscia, P. Reddy, V. M. Menon, and Z. Shotan, "Near-deterministic activation of room-temperature quantum emitters in hexagonal boron nitride," *Opt. Vol. 5, Issue 9, pp. 1128-1134*, vol. 5, no. 9, pp. 1128–1134, Sep. 2018

[317] J. Chaste, A. Missaoui, S. Huang, H. Henck, Z. Ben Aziza, L. Ferlazzo, C. Naylor, A. Balan, A. T. C. Johnson, R. Braive, and A. Ouerghi, "Intrinsic Properties of Suspended MoS_2 on SiO_2/Si Pillar Arrays for Nanomechanics and Optics," *ACS Nano*, vol. 12, no. 4, pp. 3235–3242, Apr. 2018

[318] C. Errando-Herranz, E. Schöll, R. Picard, M. Laini, S. Gyger, A. W. Elshaari, A. Branny, U. Wennberg, S. Barbat, T. Renaud, M. Sartison, M. Brotons-Gisbert, C. Bonato, B. D. Gerardot, V. Zwiller, and K. D. Jöns, "Resonance Fluorescence from Waveguide-Coupled, Strain-Localized, Two-Dimensional Quantum Emitters," *ACS Photonics*, vol. 8, no. 4, pp. 1069–1076, Apr. 2021

[319] F. Peyskens, C. Chakraborty, M. Muneeb, D. Van Thourhout, and D. Englund,

"Integration of single photon emitters in 2D layered materials with a silicon nitride photonic chip," *Nat. Commun. 2019 101*, vol. 10, no. 1, pp. 1–7, Sep. 2019

[320] K. R. Williams and R. S. Muller, "Etch rates for micromachining processing," *J. Microelectromechanical Syst.*, vol. 5, no. 4, pp. 256–269, Dec. 1996

[321] K. R. Williams, K. Gupta, and M. Wasilik, "Etch rates for micromachining processing - Part II," *J. Microelectromechanical Syst.*, vol. 12, no. 6, pp. 761–778, Dec. 2003

[322] Y. Y. Kuznetsova, M. Remeika, a a High, a T. Hammack, L. V Butov, M. Hanson, and a C. Gossard, "All-optical excitonic transistor.," *Opt. Lett.*, vol. 35, no. 10, pp. 1587–9, 2010

[323] L. A. Jauregui, A. Y. Joe, K. Pistunova, D. S. Wild, A. A. High, Y. Zhou, G. Scuri, K. de Greve, A. Sushko, C. H. Yu, T. Taniguchi, K. Watanabe, D. J. Needleman, M. D. Lukin, H. Park, and P. Kim, "Electrical control of interlayer exciton dynamics in atomically thin heterostructures," *Science (80-.).*, vol. 366, no. 6467, pp. 870–875, Nov. 2019

[324] Y. Liu, K. Dini, Q. Tan, T. Liew, K. S. Novoselov, and W. Gao, "Electrically controllable router of interlayer excitons," *Sci. Adv.*, vol. 6, no. 41, p. eaba1830, Oct. 2020

[325] D. N. Shanks, F. Mahdikhanysarvejahany, T. G. Stanfill, M. R. Koehler, D. G. Mandrus, T. Taniguchi, K. Watanabe, B. J. Leroy, J. R. Schaibley, and J. Schaibley, "Interlayer Exciton Diode and Transistor," Mar. 2022

[326] C. Cho, J. Wong, A. Taqieddin, S. Biswas, N. R. Aluru, S. Nam, and H. A. Atwater, "Highly Strain-Tunable Interlayer Excitons in MoS_2 /WSe_2 Heterobilayers," *Nano Lett.*, vol. 21, no. 9, pp. 3956–3964, May 2021

[327] J. M. Kim, F. Haque, E. Y. Hsieh, S. M. Nahid, I. Zarin, K.-Y. Jeong, J.-P. So, H.-G. Park, S. Nam, J. M. Kim, S. Nam, M. F. Haque, E. Y. Hsieh, S. M. Nahid, I. Zarin, K.-Y. Jeong, J.-P. So, and H.-G. Park, "Strain Engineering of Low-Dimensional Materials for Emerging Quantum Phenomena and Functionalities," *Adv. Mater.*, p. 2107362, 2022

[328] W. van Gelder and V. E. Hauser, "The Etching of Silicon Nitride in Phosphoric Acid with Silicon Dioxide as a Mask," *J. Electrochem. Soc.*, vol. 114, no. 8, p. 869, Aug. 1967

[329] J.-E. Jung, Y. Barsukov, V. Volynets, G. Kim, S. K. Nam, K. Han, S. Huang, and M. J. Kushner, "Highly selective Si_3N_4/SiO_2 etching using an NF_3/N_2/O_2/H_2 remote plasma. II. Surface reaction mechanism," *J. Vac. Sci. Technol. A Vacuum, Surfaces, Film.*, vol. 38, no. 2, p. 023008, Jan. 2020